
Photoinduced N₂O dissociation and CO oxidation on thin MgO films

*Im Fachbereich Physik
der Freien Universität Berlin
eingereichte Dissertation*



Philipp Giese

March 2012

This work was done between April 2008 and March 2012 in the group of Professor Martin Wolf at the Physics Department of the Freie Universität Berlin and the Department of Physical Chemistry at the Fritz Haber Institut der Max Planck Gesellschaft.

Berlin, March 2012

Erstgutachter: Prof. Dr. Martin Wolf
Zweitgutachter: Prof. Dr. José Ignacio Pascual

Datum der Disputation: 9. Mai 2012

Abstract

As a model system for photochemistry on oxide surfaces, the generation of atomic oxygen by photodissociation of N_2O adsorbed on thin MgO films which are grown on Ag(001) has been studied under UHV conditions. The reactivity of the generated atomic oxygen was examined by studying the oxidation of CO. If MgO with adsorbed N_2O is irradiated with photons ($h\nu = 5.0\text{ eV}$), TPD spectra show a N_2O depletion and generation of N_2 (desorbing $\approx 55\text{ K}$) and atomic oxygen (desorbing recombinatively at $\approx 550\text{ K}$). An analysis of the photon dose dependence suggests two N_2O dissociation pathways on the surface with reaction cross sections of about 10^{-19} cm^2 : The irradiation with $h\nu = 5.0\text{ eV}$ leads to an electron-hole-pair excitation at the edges of the MgO film. Excited electrons are trapped at certain defect sites which lead to localized electrons and localized holes at low coordinated sites. These localized charges can cause a dissociation of nearby adsorbed N_2O . The presence of the electron and the hole lead to singly charged atomic oxygen. EPR spectroscopy done in cooperation with the department of Hajo Freund confirmed that the generated atomic oxygen is correlated with a free spin. A site-selective chemistry can be applied with different photon energies. If a photon energy of 6.4 eV is used, the reaction cross sections increase to 10^{-17} cm^2 which is explained by the increased probability to create a trapped electron: The photoexcitation of MgO films at terrace sites leads to a higher amount of generated electron-hole pairs compared to the photoexcitation at lower coordinated sites. The reaction yield could also be controlled by varying the MgO film preparation: Due to a larger surface roughness for thicker MgO films (which led to more electron traps), UV-induced atomic oxygen generation scales with the MgO film thickness. Irradiation ($h\nu = 5.0\text{ eV}$) of the coadsorbate consisting of CO and atomic oxygen leads to a formation of CO_2 .

Zusammenfassung

Als Modellsystem für Photochemie auf Oxiden wurde in dieser Arbeit die Bildung von atomarem Sauerstoff durch Photodissoziation von N_2O -Adsorbaten auf dünnen MgO-Filmen, präpariert auf Ag(001), unter UHV-Bedingungen untersucht. Die Reaktivität des atomaren Sauerstoffs wurde anhand von CO Oxidation überprüft. Nach UV-Bestrahlung zeigen thermische Desorptionsspektren eine Abnahme der ursprünglichen N_2O Bedeckung und eine Bildung von N_2 (Desorption bei ≈ 55 K) und atomarem Sauerstoff (rekombinative Desorption bei ≈ 550 K). Die Photonenabhängigkeit der N_2O -Dissoziation läßt sich mit einem Mechanismus bestehend aus zwei Reaktionspfaden beschreiben, deren Querschnitte jeweils $\approx 10^{-19}$ cm^2 sind: UV-Bestrahlung ($h\nu = 5.0$ eV) führt zu einer Elektronen-Loch-Paar-Anregung an Kanten des MgO-Films. Angeregte Elektronen werden an bestimmten Defekten eingefangen und führen zu lokalisierten Elektronen und Löchern, wodurch in der Nähe adsorbiertes N_2O dissoziiert. Durch diese Ladungen entsteht einfach geladener atomarer Sauerstoff, dessen freier Spin durch eine EPR-Studie in Kooperation mit der Abteilung von Hajo Freund nachgewiesen wurde. Oberflächen-selektive Chemie kann durch unterschiedliche Photonenenergien realisiert werden. N_2O -Dissoziation mit einer Photonenenergie von $h\nu = 6.4$ eV erhöht die Reaktionsquerschnitte auf 10^{-17} cm^2 . Die erhöhte Wahrscheinlichkeit, lokalisierte Ladungen zu generieren ist eine Erklärung hierfür: Die Photonenanregung an Terrassen von MgO-Filmen führt zu einer größeren Anzahl an generierten Elektron-Loch-Paaren als die an geringer koordinierten Oberflächenstellen. Auch durch Variation der MgO-Präparation kann die Reaktionsausbeute kontrolliert werden: Da dickere Filme eine rauhere Oberfläche haben und damit mehr Elektronenfallen aufweisen, wächst die UV-induzierte Generation von atomarem Sauerstoff mit der MgO-Filmstärke. Bestrahlung eines Koadsorbats bestehend aus vorher generiertem atomarem Sauerstoff und CO führt zur Bildung von CO_2 und bestätigt die Reaktivität des atomaren Sauerstoffs.

Contents

Abstract	i
Zusammenfassung	iii
List of Figures	ix
Introduction	xiii
1 Concepts and models	1
1.1 MgO - general aspects	1
1.1.1 Electronic structure and optical properties of oxides	2
1.1.2 Chemical properties of oxide surfaces	3
1.1.3 Thin oxide films	6
1.2 Photochemistry on oxide surfaces	8
1.3 Adsorption and desorption of molecules	10
1.3.1 Physisorption and Chemisorption	10
1.3.2 Thermodynamics of desorption processes	14
1.3.3 Theory behind Temperature programmed desorption	19
2 Experimental system and used methods	23
2.1 UHV setup for photochemistry	23
2.1.1 Sample holder and manipulation	26
2.2 Excimer Lasers	28
2.3 Temperature programmed desorption (TPD)	29
2.3.1 Signal amplification by Feulner Cup shielding of the mass spectrometer	29
2.3.2 Analysis of TPD spectra	32
2.4 Electron energy loss spectroscopy (EELS)	35
2.5 Electron paramagnetic resonance (EPR)	38

3	MgO films grown on Ag(001)	41
3.1	Preparation and characterization of MgO films	41
3.1.1	Chemical characterization of the Sample	43
3.1.2	Study of the LEED-pattern for Ag(001) and MgO	43
3.1.3	Surface phonons of MgO	45
3.2	Experimental procedures	49
4	Adsorption of N₂O on thin MgO films	53
4.1	Vibration species of N ₂ O	55
4.2	TPD spectra of N ₂ O/MgO	57
4.3	Conclusion	60
5	Photoinduced N₂O dissociation on MgO films	63
5.1	Photon dose dependence	67
5.2	Photon energy dependence	71
5.2.1	photon doses	75
5.2.2	N ₂ O coverage dependence	77
5.3	MgO preparation dependence	79
5.3.1	Influence of film thickness	80
5.3.2	Additional Mg deposition on MgO films	85
5.3.3	Post-oxidation of magnesium	88
5.4	Observation of free spin by EPR	93
5.5	Conclusion	97
6	Oxidation by pregenerated atomic oxygen	101
6.1	CO and CO/O coadsorbates adsorbed on MgO	101
6.2	UV-irradiation of CO/N ₂ O and CO/O coadsorbates	104
6.3	Conclusion	111
7	Summary and Outlook	115
A	Influence of atomic oxygen on CH₄	119
	Bibliography	125
	Abbreviations	135
	Publications	137

<i>CONTENTS</i>	vii
Curriculum vitae	139
Danksagung	141
Erklärung gemäß §7, Abs. 4 der Promotionsordnung	145

List of Figures

1	SEM images of MgO powder	xiv
1.1	Structure of MgO surface	2
1.2	Calculated band structure of MgO	3
1.3	Defects on a MgO surface	4
1.4	Formation of mosaic structures in MgO films	7
1.5	Photoprocesses on MgO powders	9
1.6	Potential energy curves for physisorbed and chemisorbed molecules	11
1.7	Energy diagram for CO adsorption	12
1.8	Water adsorption on flat and defective MgO surfaces	13
1.9	Schematic representation of TST	17
1.10	Thermal desorption spectroscopy scheme	19
1.11	Desorption orders	22
2.1	UHV Setup for photochemical measurements	24
2.2	Scheme of a quadrupole mass spectrometer	25
2.3	Sample holder	26
2.4	Temperature calibration	27
2.5	Feulner-Cup Scheme	30
2.6	Feulner-Cup Influence	31
2.7	Inverted Polanyi-Wigner plot	34
2.8	EELS spectrum of CO/Cu(001)	36
2.9	Scheme of EELS spectrometer	36
2.10	Electron scattering at surfaces	38
3.1	Thickness-dependence of Auger spectra from MgO films	42
3.2	Low energy electron diffraction of Ag(001) and thin MgO films	43
3.3	Spot intensity oscillations of NiO and MgO	44

3.4	Contribution of surface phonons on HrEELS spectra	46
3.5	Fourier deconvolution of MgO spectrum	49
3.6	TPD spectrum of N ₂ O	50
3.7	Photodissociation of N ₂ O on MgO	51
4.1	IR-Spectrum of N ₂ O	54
4.2	Raw HrEELS spectrum of N ₂ O on MgO	56
4.3	Deconvoluted HrEELS spectrum of N ₂ O on MgO	57
4.4	TPD spectrum of N ₂ O	58
4.5	Inverted Polanyi Wigner plot of N ₂ O	59
4.6	Coverage dependence of pre-exponential factor	59
5.1	Photodissociation of N ₂ O	64
5.2	Blocking of reaction	65
5.3	Thermally induced partial recovery	66
5.4	Photoinduced nitrogen in comparison to adsorbed one	67
5.5	Photon dependence of TPD spectra	68
5.6	Reaction model for N ₂ O photodissociation	70
5.7	Site dependence of MgO band gap	72
5.8	TD reaction spectra for different wavelengths	74
5.9	Photon energy dependence of N ₂ O dissociation	76
5.10	N ₂ O coverage dependence for 5.0 eV excitation	78
5.11	N ₂ O coverage dependence in general	79
5.12	Preparation dependence of N ₂ yield	81
5.13	Preparation dependence of O ₂ yield	81
5.14	Thin film oxygen desorption	83
5.15	Possible scenarios for reaction at thin films	84
5.16	N ₂ O desorption from Ag(001)	84
5.17	Additional coloring by Mg deposition	86
5.18	N ₂ generation on colored MgO	87
5.19	Scheme for post oxidized MgO film on Ag(001)	88
5.20	Auger electron spectra of postoxidized and simultaneously oxidized magnesium	90
5.21	N ₂ O desorption from regular and postoxidized MgO films	91
5.22	Photochemistry on post oxidized Mg	92
5.23	Photochemistry on MgO in N ₂ O gas phase	94
5.24	EPR-Signatures prior and after irradiation	95

5.25	Temperature dependence of EPR-signatures	96
5.26	Excitation scheme	97
6.1	Scheme of CO adsorption on MgO surfaces	102
6.2	TPD spectra of CO	103
6.3	CO + O ⁻ coadsorbate	103
6.4	Photoinduced CO ₂ generation by irradiation of a CO / N ₂ O coadsorbate	105
6.5	Comparison between coadsorption and sequential adsorption of N ₂ O and CO	106
6.6	Photon dependence of CO oxidation	107
6.7	Reaction mechanism of CO oxidation	108
6.8	Hyperthermal recovery of previously blocked reaction sites	110
6.9	Catalytic cycle for CO oxidation	112
A.1	Influence of atomic oxygen on CH ₄ coadsorbate	121
A.2	Dosage dependence of CH ₄ coverage	121
A.3	Adsorption of CH ₄ on MgO surfaces	123

Introduction

The understanding of surface processes is of critical importance in industrial chemistry and the control of elementary processes at interfaces. Various chemical reactions in nature happen at the surface of either liquids or solids. Corrosion, i.e. the oxidation of metal is a textbook example of surface chemistry. In heterogenous catalysis, the selectivity and rate of chemical transformations is enhanced and controlled by a sequence of elementary steps at specific so called active sites at the catalyst surface. In the Haber-Bosch-Process, for example, the conversion of nitrogen and hydrogen to ammonia is dramatically enhanced in the vicinity of iron particles.

Light is also able to induce chemical processes at surfaces or interfaces by electronic excitations. A field of current interest is photovoltaics where the photoexcitation of electron hole pairs induces a current. A second well-known and investigated example is the photon-induced degradation of organic molecules adsorbed on TiO_2 surfaces. In a semiconductor like TiO_2 a photon with enough energy can excite an electron-hole pair whose charge carriers can generate radical species on the surface. These lead ultimately to decomposition of organic molecules to CO_2 and H_2O [1, 2].

Industrial catalysts are often quite complicated systems. Fig.1 shows SEM images of MgO material used for catalytic purposes. As shown, the structure is very complex and thus a chemistry related to distinct defects is hard to quantify. A frequently used approach in surface science is the study of model systems to draw conclusions from these to the "real world applications". As these model systems themselves might be completely different from the actual system - depending on the assumptions stated before and the possibilities in generating a model system, the bridge over this pressure and material *gap* might lead into wrong directions if the model system is chosen based on wrong assumptions [4].

One important class of (photo)catalytic active materials are oxides. MgO in particular is a typical support material in many catalytic processes. Moreover,

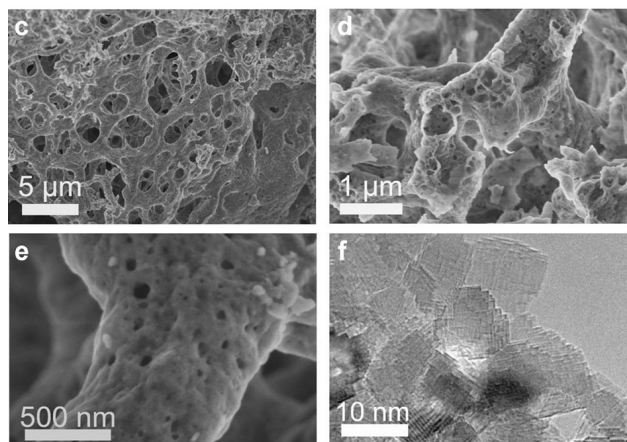


Figure 1: SEM images of MgO powder used in catalytic reactors. The surface is porous and difficult to describe thus an unambiguous correlation between reactivity and specific active site is impossible. Picture taken from Ref. [3].

MgO has shown also direct catalytic properties as in the oxidative coupling of methane [5] or the water gas shift reaction [6]. The simple geometric and electronic structure has yielded to a lot of oxide studies with MgO serving as a model system.

The investigation of these photochemical reactions on oxide surfaces in general [7–11] and MgO surfaces in particular [12–14] is a field of constant interest. Especially the group of Knözinger has investigated the photochemistry on MgO powders in great detail [15–25]. However, the powder-material and the elevated pressures which were used makes it complicated to discuss the adsorbate binding to the substrate, quantify the reaction yield to evaluate different reaction mechanisms or modify the substrate to generate reactive defects.

In this thesis the photoinduced dissociation of N_2O on epitaxially grown MgO films was studied to discuss these points. As the growth of oxide films can be controlled, it is possible to manipulate the defect density by different preparation routines. The possibility to quantify the concentration of educts and products on the surface makes it possible deduce a reaction mechanism which takes place. Moreover, the cross sections for these reactions are able to be quantified. The dependence of photon dose and photon energy studied at an N_2O adsorbate under UHV conditions leads to a confirmation of site dependent chemistry and extends this knowledge to the chemistry after electron hole pair excitation at terraces. N_2O coverage dependent measurements gain insight into the adsorption and reaction properties of N_2O on MgO. To confirm the influence of defects, the prepa-

ration conditions of the MgO films were varied by different degrees. Furthermore an electron spin resonance (EPR) experiment has been performed in collaboration with the department of Hajo Freund in order to elucidate the nature of photochemically formed atomic oxygen species. To confirm and study the reactivity of the atomic oxygen generated by photoinduced N_2O dissociation on MgO, the oxidation of carbon monoxide was investigated.

This thesis is organized as follows:

- In the first chapter, the background knowledge will be presented. In the first part, oxide surfaces, their (photo)chemical properties and the properties of thin oxide films are discussed. The second part of the first chapter is more general and deals with adsorption processes on surfaces.
- The second chapter deals with the experimental setup used in this experiment. The setup and the techniques which were used to acquire the data will be presented.
- The presentation of the measurements recorded and analyzed in this thesis begins with the third chapter: The properties of prepared MgO films grown on Ag(001) will be discussed here.
- In the following chapter the adsorption properties of N_2O on MgO are discussed on the basis TPD spectra and HREELS measurements. The monolayer properties of the N_2O adsorbate are discussed and a conclusion is drawn.
- In the fifth chapter, the photoinduced N_2O adsorbed on MgO is discussed. From the photon dependence, a reaction mechanism is proposed. The photon energy dependence reveals the possibilities to induce a site-selective chemistry. Different MgO preparation routines were examined to maximize the reaction yield. This chapter concludes with an EPR investigation where the generated atomic oxygen is looked upon.
- This atomic oxygen is finally put in use to investigate oxidating properties at one model system in the last chapter: The pregenerated atomic oxygen is used to study the CO oxidation as a well-known model system.

Chapter 1

Concepts and models

In this chapter, the conceptual and theoretical background to the presented thesis is discussed. First, the general properties of MgO are presented. As the chosen model system MgO is, like other binary oxides, an insulator, its physical and chemical properties differ significantly from the respective properties of metals. While the latter is oftentimes the textbook example when discussing surface chemical processes, insulator surfaces are not treated in great depth (see e.g. [26–29]). As photochemistry on oxide surfaces is closely related to the optical and chemical properties of the specific compound, the next section discusses the non-thermal possibilities of inducing a chemistry with photons on insulator materials.

The second part deals with adsorption characteristics on surfaces. The different mechanisms leading to adsorption are discussed. This part concludes with a general discussion about the thermodynamics occurring during desorption. This discussion is closely related to the presentation of the detection method (Thermal desorption spectroscopy, see chapter 2.3).

1.1 MgO - general aspects

As MgO is the model system dealt with in this thesis, the aim of this chapter is mainly to discuss the properties of this oxide. With its simple structure, MgO serves oftentimes as a model system for more complex materials so the general conclusions about electronical, optical and chemical properties are also valid for other oxides.

Fig. 1.1 shows a sketch of the surface structure of MgO. It is a rocksalt structure, a fcc lattice with a basis consisting of two ions, the Mg^{2+} and the O^{2-} ion, respectively. The lattice constant is 4.2 Å. MgO is thermally inert: its melting point

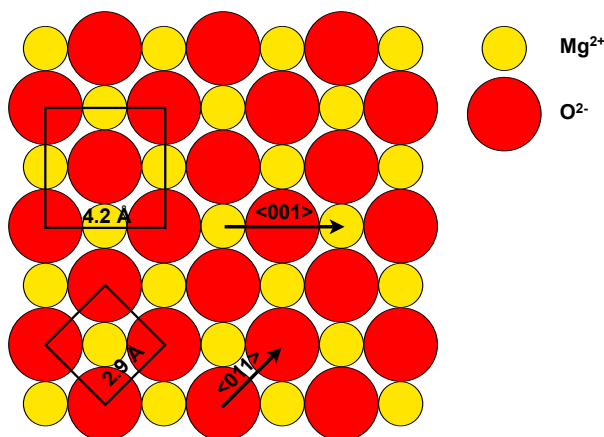


Figure 1.1: Structure of the MgO surface. The structure is a rocksalt structure, a fcc structure with a basis of two atoms. In this sketch the lattice constants in 001- and 011-direction, i.e. the lattice constant and the distance to the next neighbor are depicted. They are 4.2 Å and 2.9 Å, respectively. Taken in modified form from Ref. [30]

is at 3073 K and its boiling point at ≈ 4070 K. Without impurities it is transparent for wavelengths higher than 165 nm [30], dependent on preparation technique there might be small impurities which lead to a yellow-colored MgO crystal.

1.1.1 Electronic structure and optical properties of oxides

The basis to understand the particular chemical and (photo)catalytical properties of MgO lies within its band structure. For MgO, the band gap is 7.8 eV [32–34], see Fig. 1.2¹, thus electrons cannot be excited simply by thermal means from the valence bond to the conduction bond. Since the band gap is that large, visible light transmits through intact, clean MgO.

This band gap is significantly reduced for lower coordinated sites see table 1.1 [33, 37]. Additionally, defect sites, which will be discussed in the next section, reduce the band gap and may even lead to light absorption in the visible range. This light absorption is due to an electron excitation from the valence to the conduction band and thus the generation of an exciton, an electron-hole pair. This process is of crucial importance for photochemistry on oxide surfaces which will be dealt with

¹Some discrepancy in the literature is here as a few sources claim the band gap to be 8.7 eV [35,36]. The reason for this discrepancy is that the latter make a distinction between the bulk exciton and the band gap.

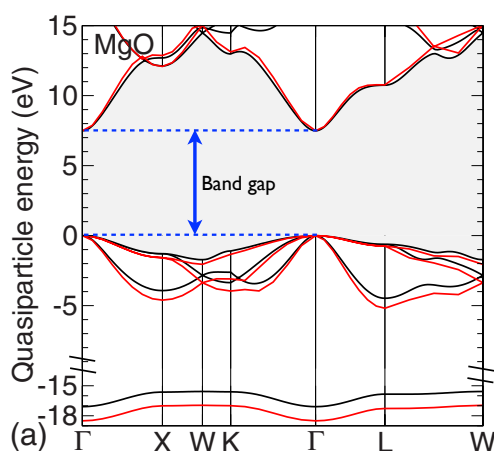


Figure 1.2: Band structure of MgO as calculated by DFT within two different approximations shown in black and red. The band gap has its minimum at the Γ point and is 7.8 eV. This picture is taken from Ref. [31].

Table 1.1: Band gap of MgO for different types of sites. The energies are taken from Refs. [33,37]

Surface site	coordination number	Energy gap /eV
bulk	8	7.8
terraces	6	6.2
edges	4	5.4
corners, kinks	3	4.6

in chapter 1.2.

1.1.2 Chemical properties of oxide surfaces

The chemical properties and thus their capabilities as catalytic material are closely related to the electronic structure of the respective oxide. The high band gap, varying with the type of the respective surface site, makes it possible to localize charges on the surface. The electronic structure and electron affinity varies for every different type of site, thus a site-selective chemistry can be expected.

Beside lower coordinated sites as edges, kinks and corners, more localized defects occur on MgO surfaces which possess distinct chemical properties (see Fig. 1.3):

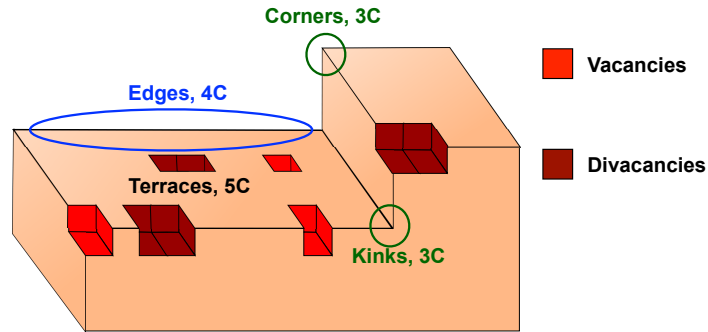


Figure 1.3: Schematic representation of various defects on a MgO surface. The coordination number for terraces, edges, corners and kinks is denoted as $x\text{C}$.

- The most prominent type of defect on oxide surfaces is the oxygen (or anion) vacancy or F-center [38]. These vacancies absorb light in the visible range, which is the reason for the name F-center: F is an abbreviation of the german word Farbe - color. These point defects are sites where an oxygen ion in the lattice is missing. Three kinds of F-centers exist on MgO differing in their charge: diamagnetic oxygen vacancies are neutrally or doubly charged and known as F^0 and F^{2+} centers, respectively. It has to be pointed out that this charge is *with respect to the regular oxide*. That said, the F^0 center is an oxygen vacancy with two electrons still present while the F^{2+} center is an oxygen vacancy with no localized electron. Paramagnetic F^+ centers are consequently oxygen vacancies with one electron captured. These paramagnetic F-centers are supposed to be highly reactive as the associated free electron suggests.

The doubly charged F-centers are capable of capturing electrons as they possess a high electron affinity. As discussed later in chapter 1.2, a suitable way of transforming doubly F^{2+} to F^+ centers is by electron-hole pair excitation.

Though these sites will be of significant importance on highly defective powder materials, on single crystalline surfaces or MgO films their natural abundance is very limited: The number of free spins (i.e. F^+ centers) on MgO surfaces is lower than $1 \cdot 10^{12}$ spins [39]. As the singly charged oxygen vacancy is expected to be more stable than the doubly charged one [40], almost no F^{2+} centers are to be expected.

- Magnesium (or cation) vacancies are vacancies with one Mg ion missing, analogous to anion vacancies with one missing oxygen ion. These centers are known as V^0 , V^- and V^{2-} and result from the formal removal of Mg^0 , Mg^+ and Mg^{2+} , respectively. The electrons associated with these sites are localized on neighboring oxygen atoms [41]
- The removal of a neutral MgO unit from the lattice results in a divacancy. Electronically neutral they can act as electron traps, though not as efficient as F^{2+} sites [42]. However, as their abundance is significantly larger on MgO surfaces these sites are an important candidate for chemically relevant sites.
- Similar as the divacancy other more extended defects as reverse corners [43] or misfit dislocations [44] may act as electron traps and thus play a significant role in defect chemistry.

This list focuses on electron trapping sites on single crystalline MgO and assumes no impurities or hydration effects which may also induce reactive defect sites (grain boundaries, charged sites due to doping, protonated sites...). Two types of chemistry were studied in great detail at the defects presented in the list above.

On the one hand, metal particles adsorbed on certain kinds of defects exhibit chemical properties which differ from regular metal: Upon oxygen vacancies, metal clusters are bound stronger when compared to regular adsorption sites [45–48]. Moreover, the charge of the adsorbed metal clusters is negative suggesting an influence of the defect and its trapped electron. As MgO serves as support for catalytically relevant metal particles in reactors these results are interesting as they suggest an *active role* of the support material.

But not only as an active supporter material but as a catalyst itself magnesium oxide is used. A basic reaction step investigated was the hydrogen dissociation at F^{2+} -centers [49], where the hydrogen ions form with the anion vacancies hydrogenated, singly charged anion vacancies which are known as $F^+(H)$ centers. These hydrogenated sites possess the same chemical properties as singly charged anion vacancies and serve oftentimes as model system for the dissociative adsorption of oxygen [50] or N_2O [51].

One example for chemistry at more extended defects is the water dissociation at divacancies [52,53]. DFT calculations suggest that a water molecule dissociates instantaneously at a divacancy by forming a $[V_{Mg},2H]$ complex, a magnesium vacancy with two hydrated oxygen atoms as neighbors. One of these oxygen atoms is a fragment of the previously adsorbed water molecule.

Another more complicated example for defect related chemistry on pretreated MgO is the oxidative coupling of methane. Ito et al introduced CH₄ and O₂ into a flow reactor with differently prepared MgO as catalyst. When using lithium-promoted MgO, the methane dissociation rate of CH₄ and the selectivity towards C₂ compounds was dramatically enhanced [54]. By evaluating EPR spectra of the catalyst they deduced that Lithium atoms serve as dopant by taking the lattice places of magnesium atoms. As Lithium can only donate one electron, a singly charged oxygen ion is formed. The supposedly formed active site is known as Li⁺O⁻ - site and it is thought that the associated oxygen ion lowers the methane dissociation barrier significantly [55]. As this process was the initial motivation for this study, a more profound introduction and discussion is found in the appendix A.

1.1.3 Thin oxide films

For surface science purposes, a pure oxide crystal is a difficult system to deal with. The bad electrical conductivity is oftentimes accompanied by a bad thermal conductivity. As these insulating oxides can charge up, they prohibit the use of techniques which use electrons and ions as information carriers. Both of these problems are circumvented by depositing oxide films on a metal substrate.

Not every metal crystal serves as a good substrate for an oxide film; the lattice parameters should be similar. For MgO, usually used metallic substrates are Mo(001) and Ag(001), sometimes also Fe(001) [56]. The lattice mismatch between metal and MgO is +3 % for silver and -5 % for molybdenum. Thus, the MgO film grown on Ag(001) is expected to be flatter than the MgO film on Mo(001). As shown in Fig. 1.4 even the small lattice mismatch ultimately leads to an interface dislocation with the (011) glide plane of the MgO film [57–59]. These dislocations are called "mosaic structures". Beside the formation of these dislocations, the thermal instability of silver compared to MgO has to be taken into account thus it is questionable whether the flatness of MgO films on Ag(001) will be held valid for thick films. This question will be investigated in chapter 3.1.2.

A second question when dealing with oxide films on metal surfaces is whether the chemical and electronic structures of the film differ from a regular oxide. Very thin oxide films show different properties than bulk oxides which are also researched extensively [60–63] and help to deduce when the surface chemistry possesses no contributions from the underlying silver anymore. This issue will also be touched briefly when investigating the photochemistry on very thin MgO films, see chapter 5.3.1.

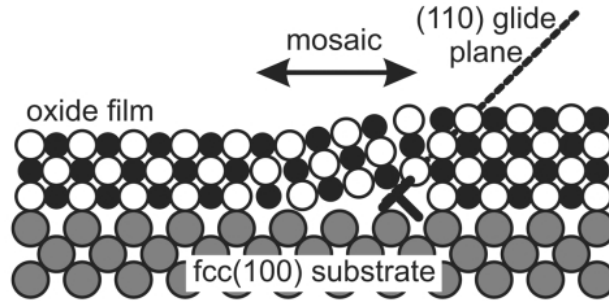


Figure 1.4: The small lattice mismatch between Ag(001) and MgO(001) leads to an interface dislocation of MgO which results in the generation of large-scale domains. The picture is taken from Ref. [57]

Different processes might alter the properties of the oxide for the thin film limit:

- The first aspect is whether the film is completely closed. MgO films on silver are known to cover the silver substrate completely at thicknesses above 2 ML, however, higher deposition temperatures would lead to silver diffusion into the MgO film and alter this picture [64].
- Moreover, the electronic structure might be different. Schintke et al have applied scanning tunneling spectroscopy measurements for thin (1-3 ML) MgO films grown on Ag(001) and could show that for films lower than 3 ML the electronic structure differs [37,65]: Due to the presence of interface states the surface band gap is reduced to about 5 eV.
- For thin films, charge transfers from the silver bulk might happen. Metal atoms deposited on thin MgO films (1-4 ML) were negatively charged in contrast to metal atoms deposited on bulk MgO where they were neutral. Moreover, the nucleation site differs: On bulk MgO, Gold atoms adsorb on O sites, while on thin MgO films, a considerable amount of gold atoms adsorb on Mg sites. This is accompanied by a stabilization of two dimensional cluster geometries in contrast to gold deposition on bulk MgO. The underlying mechanism for this charge state is a charge transfer from the metal substrate, similar to the behavior of metal clusters deposited on anion vacancies [66,67].

- Finally, the possibility of a polaronic distortion has to be taken into account. The lattice flexibility is increased for thin oxide films (up to 3 ML) which makes it possible to accommodate an electron transfer induced charge accumulation [68–70]. These may alter the chemistry on oxide surfaces, leading to chemical properties not known to bulk MgO [71, 72].

To conclude, regardless of the different properties which may differ for thin films from the regular oxide, preparation of MgO films with thicknesses significantly larger than 5 ML should lead to films with properties comparable to MgO bulk material.

1.2 Photochemistry on oxide surfaces

The possible underlying principles for photochemical processes are manifold:

- Photons may be absorbed by the adsorbate, initiating an electronic excitation in the molecules itself.
- In general photons may induce a local heating process which suffices so that the system can pass the energy barrier separating educt and product.
- In metals, hot electrons might excite the phonon-bath and the adsorbate leading to a reaction [73].
- Analogous to electronic excitations leading to hot electrons, on materials with a band gap photons can induce an electron-hole-pair excitation which may trigger a reaction on the surface. As the photochemistry on MgO, a high band gap insulator, is focus of this thesis, this latter mechanism will be discussed now.

This electron-hole pair excitation is also the underlying physical mechanism for self-cleaning chemical reactions of TiO₂: In the semiconductor, the generated exciton may separate and the resulting charge carriers might react with adsorbed water and oxygen on the surface and form radicals. These radicals then decompose organic molecules on the surface. The reaction mechanisms appearing on UV-irradiated oxide surfaces in general and MgO surfaces in particular are depicted in Fig. 1.5.

The first two steps which are not shown in the scheme are the initial photoexcitation and the trapping of an electron:



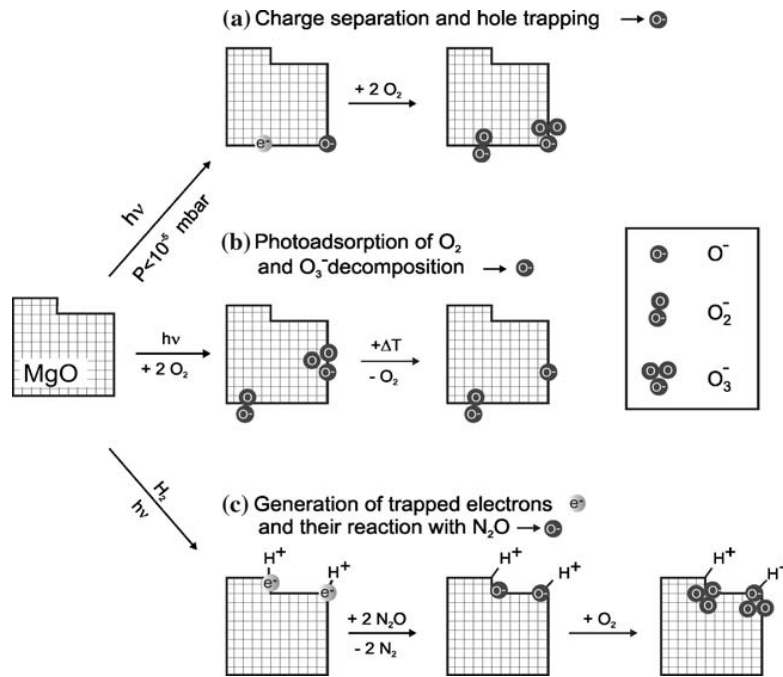


Figure 1.5: Photoprocesses on MgO powder material leading to different types of O_x^- sites. The picture is taken from Ref. [15].



The electron transfer leads to a trapping process at defect sites (eq. 1.2) and is accompanied by a transfer of the localized hole: EPR measurements have proven that the live time of both localized charges is identical suggesting that no long-distance charge separation occurs [74].

Possible electron trapping sites are the already discussed defects, see chapter 1.1.2. The localized charge is highly reactive, thus reactions as the ones shown in Fig. 1.5 can happen. Oxygen, for example, would form O_n^- ($n=1-3$) radicals on the surface, and the already mentioned $F^+(H)$ sites could be generated by photoinduced UV hydration of the surface.

All of the presented mechanisms depicted in Fig.1.5 are able to generate oxygen ions, however, their EPR-signatures show that these species are different with respect to each other: The exact nature of all involved electron traps is not known due to the complexity of the system. However, some of the EPR signals could be correlated to point defects at step edges or corners.

As indicated in the introduction, the investigation of photochemistry on thin oxide films would lead to a simpler system with less defects. The possibility to

study and modify the surface quality would make it possible to correlate the reaction products to specific defects. As pointed out before, the MgO film thickness should exceed 5 ML to guarantee an electronic structure of the MgO film which is identical to the regular electronic structure.

1.3 Adsorption and desorption of molecules

In this chapter, adsorption processes on surfaces are briefly discussed. First, the physical reasons behind adsorption and then the thermodynamics of desorption processes are examined.

A substrate has only a limited number of adsorption sites. If these are occupied by adsorbate particles, this complete adsorbate coverage is called a *monolayer*. If more than one monolayer are adsorbed onto the surface, the resulting additional coverage, only bound by adsorbate-adsorbate interactions is called *multilayer*.

1.3.1 Physisorption and Chemisorption

A broad distinction is made between two types of adsorption depending on the binding mechanism: A molecule can either *physisorb* on the surface or bind via *chemisorption*. Though it has to be noted that a continuous spectrum of interaction strengths exists and thus no sharp distinction can be done, a broad classification into either one of these two mechanisms serves in most cases well.

One oftentimes used way to describe adsorption phenomena is to sketch the binding energy in dependence of the particle distance from the surface. Fig. 1.6 sketches the potential energy curves for the "physisorption well" and for two cases of a "chemisorption well". The respective potentials between a molecule and a metal surface are expressed as a combination of a short-ranged repulsive interactions and contributions for the respective binding mechanism. The repulsive term itself has its reason in the Pauli repulsion; as the distance between the molecule and the surface becomes smaller, the filled atomic orbitals of the metal repel the orbitals of the molecule. This scheme also illustrates that the intact molecule from the gas phase, as the Pauli repulsion is too strong, cannot approach the surface more closely without entering a chemical bond i.e. changing its electronic structure in a significant way.

Physical interactions like polarization-induced Van der Waals attractions lead to physisorption. The surface bonding is weak (≤ 50 kJ/mol) and the potential energy surface is flatter leading to a higher diffusion on the surface. Physisorbed

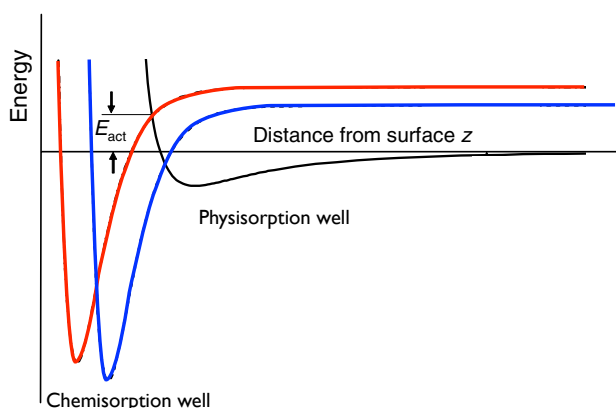


Figure 1.6: Potential energy curves in the cases of physisorption (black) and chemisorption are shown. The potential energy of the molecules to the surface are plotted against the surface distance z . Energy values above the x -axis indicate desorbed molecules. The blue curve shows a chemisorption potential for non activated adsorption while red curve one for activated chemisorption. As shown, in the case of activated adsorption a physisorbed molecule has to overcome an energy barrier E_{act} in a non-thermal way. The picture is taken from Ref. [29] in modified form.

species oftentimes experience larger adsorbate-adsorbate than adsorbate-substrate interactions, thus coadsorption phenomena are more abundant here. A textbook example for this behavior is multilayer adsorption.

A *chemical* interaction such as an electron exchange between the molecule and the surface leads to chemisorption. The binding energy of the adsorbed molecules is high (≥ 50 kJ/mol [26]) and the potential energy surface is highly corrugated which means that a bound molecule does not diffuse over the surface without investing high amounts of energy. Thus, chemisorbates stick to specific sites and their binding energy is strongly dependent on their exact position and orientation with respect to the surface.

Two types of chemisorption may occur: Non-activated and activated adsorption (see Fig. 1.6). In the case of non-activated adsorption, a molecule bound by physisorption may be chemisorbed by thermal activation, as long as the introduced energy does not suffice to induce desorption. For activated adsorption, however, the energy barrier separating the chemisorption well from the physisorption well is too large to be overcome by simple thermal means: the molecule then simply desorbs.

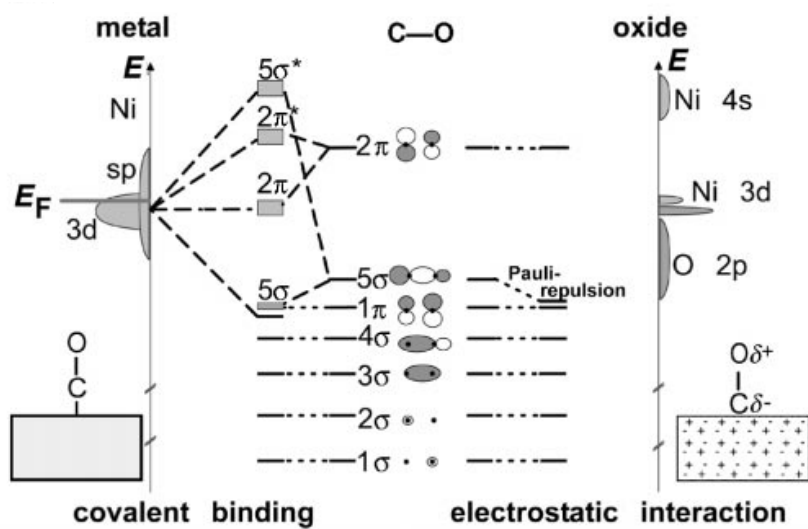


Figure 1.7: Energy diagram for CO adsorption on Nickel (left) and Nickel-oxide (right). As shown, the binding mechanism differs dramatically; while the 5σ -orbital of CO gets repelled by the oxide, no π -backdonation occurs which leads the 2π orbital unmodified in CO adsorption on oxides. The picture is taken from Ref. [75].

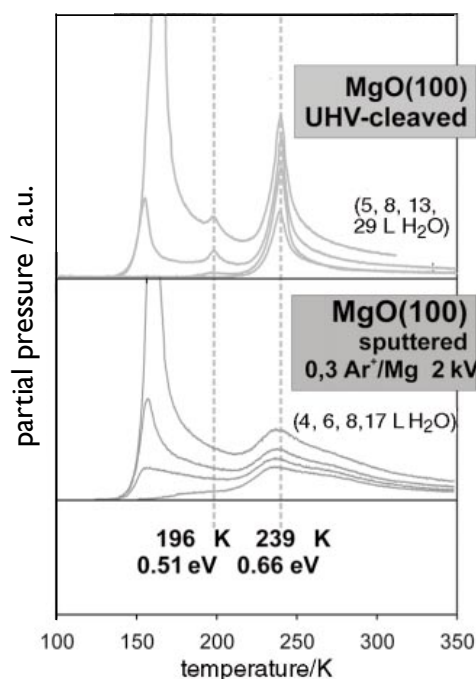


Figure 1.8: TPD spectra of water desorbing from flat (upper panel) and defective (lower panel) MgO surfaces. The broad distribution of the desorption features indicate different adsorption sites. The picture is taken from Ref. [75]

The most extreme case of chemisorption is a bond formation so strong that the substrate forms a new compound. Metals such as iron forms strong bonds with oxygen thus oxygen chemisorption easily leads to oxidation not only of surface, but also of *subsurface* sites. In the course of the experiments presented in this thesis Mg films were oxidized by interaction with oxygen (see chapter 5.3.3).

The large differences between adsorption on metals and adsorption on oxides are best described with one classical example of surface chemistry: Adsorption of carbon monoxide. On metals, CO forms a covalent bond with the surface, thus the binding energy is large. As an example, CO binds to Nickel via the σ -donation/ π -backdonation mechanism. On NiO, however, CO binds primarily in an electrostatic fashion, see Fig. 1.7 and comparatively weak to the substrate. This example shows that different adsorption mechanisms occur on an oxide surface compared to a metal surface: While chemisorbed particles tend to favor high-coordinated sites on metals, on semiconductors and insulators they prefer highly localized sites as the charge density at these sites may be different (see chapter 1.1). Sputtered MgO films exhibit broader desorption spectra as the TPD spectra of H₂O adsorbed on

MgO(001) (Fig. 1.8) suggest. This is correlated to the higher defect density of the respective surfaces. As the local topology of the respective surface site has a significant impact on its electronic structure, other adsorption mechanisms take place at defects leading to particles bound with a higher energy.

1.3.2 Thermodynamics of desorption processes

The aim of this section is to discuss what microscopic properties can be revealed by investigating desorption processes. If not stated otherwise, the literature sources mainly used were [26–28].

The experimental method used to record desorption processes is known as temperature programmed desorption (TPD) or thermal desorption spectroscopy (TDS). This method will be described later (see chapter 2.3). It has to be pointed out that the information derived from TPD spectra reveal only a mean value, thus the transition to particular particles is difficult, if even possible. However, a derived desorption energy E_{des} can be compared with values obtained with other experimental or theoretical methods to narrow down the number of possible interpretations. Moreover, the frequency factor ν might also reveal various properties of the adsorbate. Thirdly, the desorption order n can provide information about the desorption mechanism, i.e. if nonassociative or associative (recombinative) desorption occurs or evaluate whether a mixed phase is present at the surface.

The rate of desorption processes is described by the Polanyi-Wigner equation:

$$r_{des}(t) = \theta^n k_{des} = \nu \theta^n e^{-E_{des}/RT} \quad (1.3)$$

The n denotes in the desorption order, θ the absolute coverage at temperature T , E_{des} the desorption energy, and ν is known as the frequency factor. R is the molar gas constant. The desorption rate itself is the coverage change with increasing temperature. Eq. 1.3 is also the inner core of the interpretation of TPD spectra which will be described in chapters. 1.3.3 and 2.3. At this point, the different influences on the desorption rate will be discussed.

E_{des} is the desorption energy, the binding energy between the adsorbate particle and the surface. This binding energy of an adsorbate molecule to a surface might, as pointed out in chapter 1.3.1 serve to estimate whether a molecule is physisorbed or chemisorbed. The binding energy may be coverage dependent due to two reasons: First, lateral interactions between adsorbate particles might alter the desorption energy. Second, E_{des} can differ for different sites if the surfaces' electronic structure varies with the adsorption site.

Desorption processes can be distinguished in orders of desorption ranging from zero to two with desorption order $n = 1$ as the most frequently observed, nonassociative type of desorption:



That means that a limited number of molecules bound at specific adsorption sites (denoted as a) transforms in a limited number of gas particles (denoted as g) i.e. one *specific* adsorbed particle desorbs with a probability specified by the desorption constant k_{des} : Thus the rate $r_{des}(t)$ is also, as written in eq. 1.3, the product of the actual coverage θ and the desorption constant k_{des} .

It is the most often observed one for desorption from saturated surfaces. If all adsorption sites are occupied by adsorbed particles (i.e. a monolayer is formed), no more particles can be bound directly to the surface. If more particles are adsorbed, they are bound by adsorbate-adsorbate interactions and belong to the multilayer. Since the multilayer particles are more mobile and every desorbing particle can be replenished by other particles in this multilayer, zeroth order desorption occurs:



Zeroth order desorption can thus be understood as the desorption process of several *indistinguishable* adsorbed particles into the gas phase.

A third type of desorption is a associative desorption. This is described as a second order desorption process:



In the case of associative desorption, two adsorbed particles combine during the desorption process.

Zeroth order of desorption does not depend on the coverage, while the desorption rate for 1st and 2nd order desorption depend linearly or quadratically on it respectively.

The last not yet explained component in eq. 1.3 is ν . ν is known as the frequency factor (or pre-exponential factor) and is via the Frenkel Equation correlated to the lifetime of an adsorbate on the surface:

$$\tau_{des} = \nu^{-1} e^{E_{des}/RT_s} \quad (1.7)$$

Thus, a molecule stays for a finite time on the surface, depending on the surface temperature and the desorption energy.

There are two ways to get an understanding of this frequency factor: One by means of transition state theory (TST), the other one by thermodynamic considerations. Both approaches are described here to obtain an optimal understanding of this factor. As first-order desorption is the most regular type of desorption and the ideas developed here are easily expandable to the other cases, the focus will be on first order desorption.

Pre-exponential factor and transition state theory

The transition state theory is based on the idea of a potential energy surface where the product and educt states are separated by energy barriers (see Fig. 1.9). The state of the system on this barrier is known as *activated complex* or *transition state*. In this section a special case of a one step, elementary reaction, the desorption, is discussed:



Thus, a nonassociative, regular desorption process is described by transition from an adsorbed molecule A^* to a desorbed one (A) leaving one spare adsorption site ($*$). To describe a desorption process in transition state theory (TST), the following assumption have to be made:

- The energy distributions are describable by the Maxwell - Boltzmann - distributions.
- The motion along the reaction coordinate can be treated classically and is separable from other motions of the transition state.

The equilibrium constant K , i.e. the constant describing an equilibrium between adsorption and desorption, can be written in three ways:

$$K = \frac{[A][*]}{[A^*]} = \frac{k_{des}}{k_{ads}} = \frac{q_A q_*}{q_{A^*}} \exp\left(\frac{-E_{des}}{RT}\right) \quad (1.9)$$

Here, the terms in squared brackets denote the concentrations of the respective compounds, e.g. $[A^*]$ is the number of adsorbed molecules. k_{des} is the desorption rate constant, k_{ads} the adsorption rate constant and the different q_i - terms stand for the respective partition functions. So, an equilibrium constant is either the quotient of the products and educts or of the rates for a forward and a reverse reaction, i.e. de- and adsorption, or the quotient of the molecular partition functions per unit volume times the Maxwell - Boltzmann distribution. The energy E_{des} is the

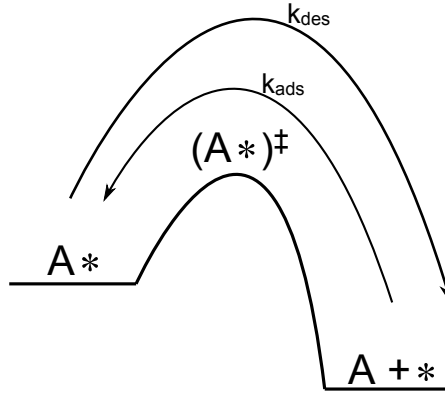


Figure 1.9: Schematic representation of transition state theory. Consider a molecule A adsorbed on adsorption site *. With a rate k_{des} molecules desorb and with a rate k_{ads} they adsorb. To achieve desorption an energy barrier represented by the transition state $(A^*)^\ddagger$ has to be overcome.

desorption energy at $T = 0$ K. This expression can be expressed as the rate constant with q^\ddagger as the partition function of the transition state:

$$K_{des} = K^\ddagger = \frac{q^\ddagger}{q_{A^*}} \exp\left(\frac{-E_{des}}{RT}\right) \quad (1.10)$$

These partition functions are separable into their translational, vibrational, rotational and electronic parts which allows to express the equilibrium constant for desorption in terms of the respective coverages:

$$K_{des} = \frac{\sigma_\ddagger}{\sigma_{A^*}} \quad (1.11)$$

σ_\ddagger is the coverage with molecules in the transition state and σ_{A^*} the one with adsorbed molecules. With this formula and eq. 1.10 the concentration of the transition state is calculated. Oftentimes, this transition state can be thought of as having one vibrational mode that leads to desorption. This is expressed as $k_B T/h\nu$. If this vibrational mode is factorized out of q^\ddagger , the remaining contributions to the partition function are labeled as q_\ddagger and eq. 1.11 can thus be rearranged to:

$$\nu\sigma_\ddagger = \sigma_{A^*} \frac{k_B T}{h} \frac{q_\ddagger}{q_{A^*}} \exp\left(\frac{-E_{des}}{RT}\right) \quad (1.12)$$

The left side is the concentration of the activated complex multiplied with desorption frequency, i.e. r_{des} by comparison with eq. 1.3. This now leads finally to an

expression for the pre-exponential factor (in combination with eq. 1.3):

$$\nu = \frac{k_B T}{h} \frac{q_{\ddagger}}{q_{A^*}} \quad (1.13)$$

If now no change in the partition function between the adsorbed phase and the transition state is assumed, a calculation reveals that $\nu \approx 10^{13} \text{ s}^{-1}$ for room temperature. This value is oftentimes guessed for desorption processes (as discussed in the section about Redhead analysis, see chapter 2.3.2). If ν is larger, that means that $q_{\ddagger} > q_{A^*}$. The transition state is then looser than the adsorbed state, which means that it is more easily excited by thermal energy. If ν is smaller than this 10^{13} s^{-1} a constrained transition state seems a valid interpretation. One example for such a thing is activated adsorption.

Thermodynamics to specify the pre-exponential factor

Extending the results derived by means of transition state theory, a second point of view is to look on the thermodynamics of the system. Thus the equilibrium constant eq. 1.9 and the desorption rate constant eq. 1.10 can be reformulated so that the desorption rate constant is expressed by the equilibrium constant:

$$k_{des} = \frac{k_B T}{h} K^{\ddagger} \quad (1.14)$$

From a thermodynamic point of view, this equilibrium constant is correlated to the Gibbs energy of activation:

$$\Delta G^{\circ} = -RT \ln(K^{\ddagger}) \quad (1.15)$$

This Gibbs energy is separable into the enthalpy and the entropy ($\Delta G^{\circ} = \Delta^{\ddagger}H^{\circ} - T\Delta^{\ddagger}S^{\circ}$). Thus, the desorption rate constant can be expressed in terms of enthalpy $\Delta^{\ddagger}H^{\circ}$ and entropy $\Delta^{\ddagger}S^{\circ}$:

$$k_{des} = \frac{k_B T}{h} \exp\left(\frac{\Delta^{\ddagger}S^{\circ}}{R}\right) \exp\left(-\frac{\Delta^{\ddagger}H^{\circ}}{RT}\right) \quad (1.16)$$

Since the enthalpy of activation is related to the activation energy ($E_a = \Delta^{\ddagger}H^{\circ} + RT$), the second exponential term of eq. 1.16 is correlated to the desorption energy while the rest can be expressed as the pre-exponential factor:

$$\nu = \frac{k_B T}{h} \exp\left(\frac{\Delta^{\ddagger}S^{\circ}}{R}\right) \quad (1.17)$$

The conclusions derived in transition state theory can now be converted into the language of thermodynamics: A pre exponential factor of $\nu \approx 10^{13} \text{ s}^{-1}$ means that

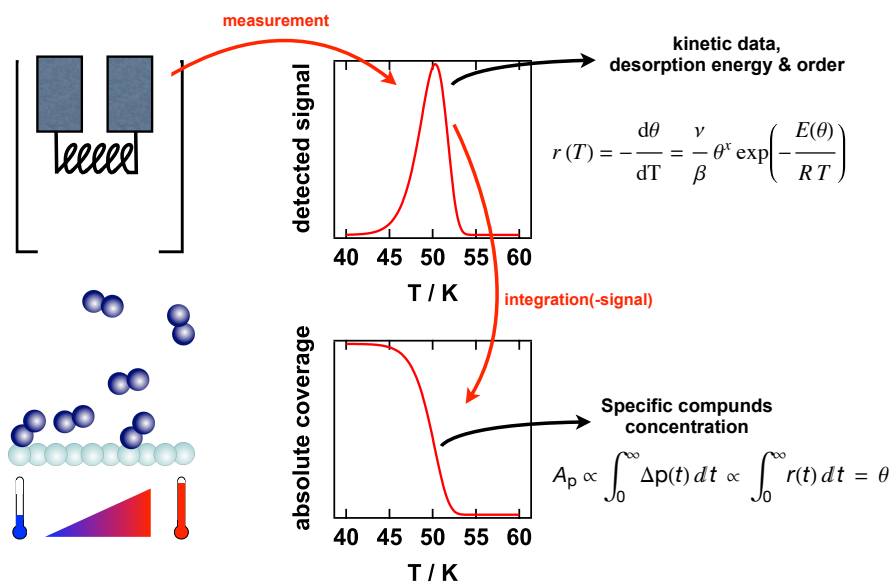


Figure 1.10: Scheme of Temperature programmed desorption (TPD) and its possibilities.

A crystal is heated with a constant heating rate. The desorbing molecules in this process are detected by a quadrupole mass spectrometer. The obtained raw data can then be analyzed in two ways: The integral of the signal is proportional to the surface coverage prior to desorption which makes it possible to quantify specific compounds on the surface. Moreover, since the signal is proportional to the desorption rate from the surface, the desorption energy, the desorption order and the pre-exponential factor can be extracted from this signal revealing kinematic information of the compounds.

the entropy is zero. A larger pre exponential factor thus means a higher entropy which is e.g. correlated to a higher number of accessible configurations and might be the result of a large variety of defects with similar adsorption energies.

1.3.3 Theory behind Temperature programmed desorption

Temperature programmed desorption spectroscopy (TPD) is one of the most widely used technique to study adsorbates in general and its thermodynamics in particular. There is numerous literature about this technique and the interpretation of the data [76–78], however, since this method is the cornerstone of the presented study the main aspects of this theory will be discussed.

The main principle of TPD is shown in Fig. 1.10: Desorbing particles from the sample particles are monitored in dependence of a linear temperature ramp. The resulting signal is correlated to the absolute coverage on the surface.

The main disadvantage is that *desorbing particles* are detected and not processes at the surface. TPD is a post-mortem method where information about what happens on the surface prior to desorption can only be gained indirectly. Even the information about the desorption process might be distorted by processes after desorption as the pumping speed of the system has its influence on the spectra.

However, provided that the compounds stay intact during desorption, TPD is a simple tool to provide information about the quantity of specific compounds on the sample - an information crucial to study the yields and cross sections of reactions on surfaces. Moreover, as the desorption temperature depends on the desorption energy, kinetic parameters can be derived from the data, see chapter 1.3.2.

Correlation between gas pressure and surface desorption

Consider a closed chamber with volume V where the molecules on the walls desorb with a desorption rate L . The chamber is pumped with a pumping rate S and has a gas density c_g . A steady state solution between the desorption of molecules from the chamber walls and the pumping speed would be achieved at

$$V \frac{dc_g}{dt} = L - c_g S = 0 \quad (1.18)$$

which implies that $c_g = L/S$. The steady state pressure at a temperature T_g is then

$$p_s = k_B T_g c_g = \frac{k_B T_g L}{S} \quad (1.19)$$

Consider furthermore a surface (surface area A_s) where molecules desorb with a desorption rate $r_{des}(t)$. Then the steady state solution in eq. 1.18 is distorted and the desorbing particles have to be taken into account:

$$V \frac{dc_g}{dt} = L - c_g S + A_s r_{des}(t) \quad (1.20)$$

Eq. 1.20 can be rewritten in terms of $\Delta p = p - p_s$:

$$V \frac{d\Delta p}{dt} + S \Delta p = k_B T_g A_s r_{des}(t) \quad (1.21)$$

$$\Rightarrow \Delta p = \frac{k_B T_g A_s}{S} r_{des}(t) \quad (1.22)$$

Thus the detected pressure change is proportional to the desorption rate of the molecules. The rate $r_{des}(t)$ follows the Polanyi-Wigner equation described earlier (eq. 1.3). It can be concluded that the *integral* of the pressure changes over time (or, over temperature if a temperature ramp is applied) is proportional to the number of desorbing particles, i.e. to the *coverage* θ .

Investigation of the Polanyi-Wigner equation

In this part, the influence of the different factors in the Polanyi-Wigner equation eq. 1.3 are discussed. To enhance the comparability with real experimental data, the desorption rate is not plotted against time but against temperature. The temperature will be increased by a linear temperature ramp with a heating rate β , i.e. $T(t) = T(0) + \beta t$. The desorption rate in dependence of the temperature is then expressed as:

$$r_{des}(T_s) = \frac{\nu}{\beta} \theta^n e^{-E_{des}/RT_s} \quad (1.23)$$

A higher desorption energy leads to a higher desorption Temperature indicated by a shift of the peak energy to higher temperatures. A quite naïve way to analyze the TPD spectra is thus to simply look at the peak temperature. The Redhead-Analysis described in the chapter 2.3.2 works this way. However, the ν dependence of the desorption characteristics might counterbalance this linear increasing trend: The peak maximum shifts to lower temperatures with increasing pre-exponential factor ν . This is understood by remembering that the frequency factor is proportional to the inverse of the adsorbates' mean lifetime (eq. 1.7). In chapter 2.3.2, a way to extract both types of information from one source is described.

An estimation of the desorption order by looking upon the raw TPD spectra for different coverages is more straightforward: For the regular first order desorption, the peak maximum does not change with coverage, while for second order, it decreases with increasing coverage. That is understandable if a recombinative desorption is assumed for these processes: For high coverages, the probability that two particles recombine (and thus desorb) is higher than for low coverages, thus the desorption rate maximum will shift to higher temperatures when the recombination probability decreases.

Zeroth desorption order is simply the Arrhenius-behavior, thus the leading edges for all coverages overlap each other and the desorption ends abruptly - a behavior expected for eq. 1.5. Sometimes, mixed states might appear in coadsorbates which can be described as desorption processes with a desorption order of 0.5. In these cases, the leading edges also overlap to some degree, however, the desorption traces are not ending abruptly. A simulation for the several desorption orders is illustrated in Fig. 1.11.

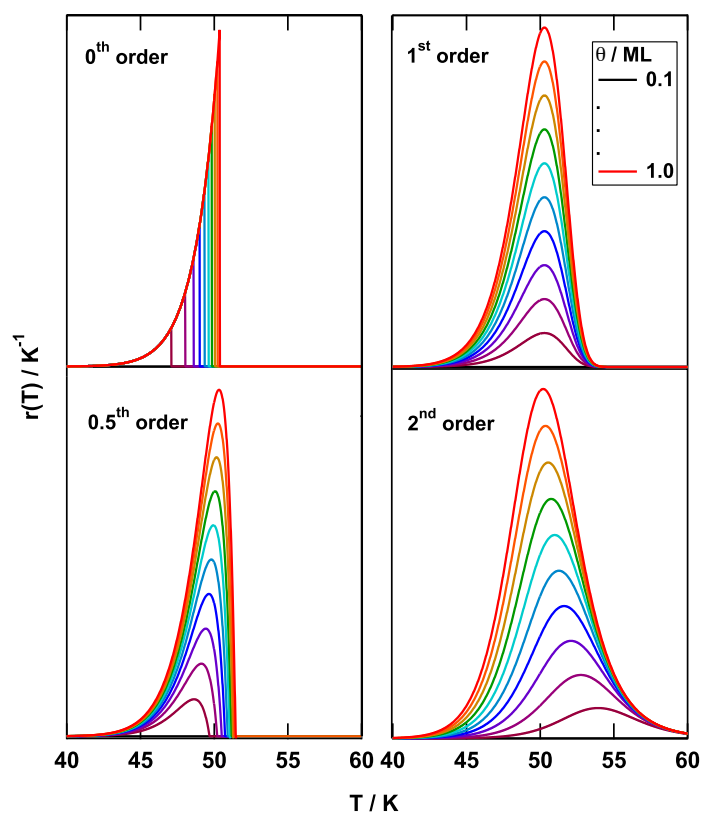


Figure 1.11: Coverage dependences of TPD spectra for desorption orders zero (multilayer desorption), 0.5 (mixed phases), one (regular, nonassociative desorption) and two (associative desorption).

Chapter 2

Experimental system and used methods

To study photochemical processes of molecules adsorbed on MgO surfaces, a UHV setup with a possibility to grow and investigate oxide films and a monochromatic light source is essential. Thus the first part of this thesis was to revive, modify and optimize an old setup for the respective needs. This UHV setup makes it possible to study adsorbates on surfaces without the influence of a gaseous environment. The light sources, excimer lasers and the fourth harmonic of a Nd:YAG laser in our case, is essential to induce the reaction as already emphasized in chapter 1.2.

This chapter will also introduce the techniques used in this experiment. The focus will be on the quadrupole mass spectrometer and especially the Feulner-Cup used to record TPD spectra.

2.1 UHV setup for photochemistry

A sketch of the experimental setup is shown in Fig. 2.1. The ultra high vacuum (UHV) chamber is connected to a pumping stand from Pfeiffer Vacuum (Type: TSU 071), one turbomolecular pump (also from Pfeiffer, type TCP 121), an ion getter pump from Varian (Model No. 929-0066) and a titan sublimation pump, also from Varian (Model No. 929-0034). This pumping system is necessary to pump the chamber down to 10^{-11} mbar and thus minimize uncontrolled surface gas interactions. The number of gas molecules interacting with the surface per second can be estimated with the Hertz-Knudsen Equation:

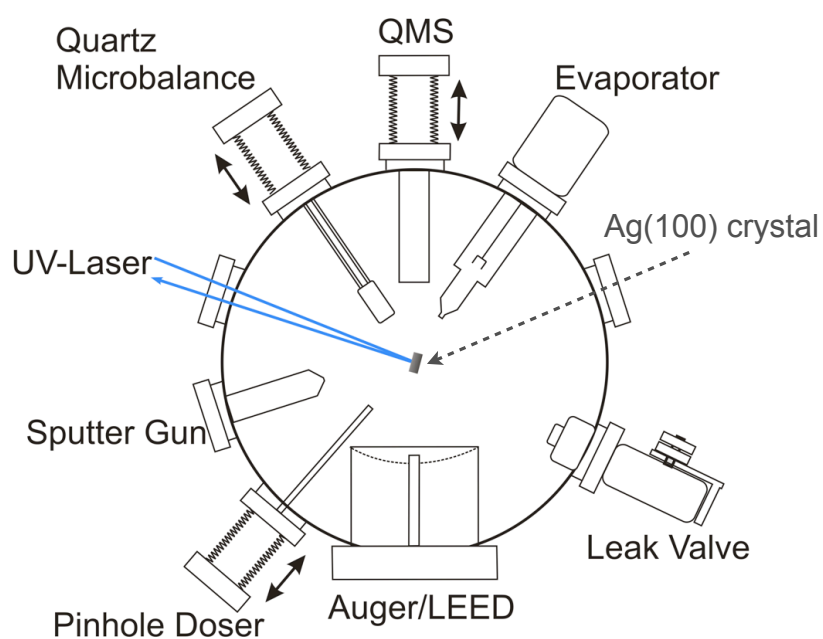


Figure 2.1: UHV setup for the photochemical measurements. This setup has a base pressure below 10^{-10} mbar. The sample can be cooled down to 20 K. MgO films are prepared in situ and are characterized by LEED and Auger electron spectroscopy, while adsorbates are examined by TPD.

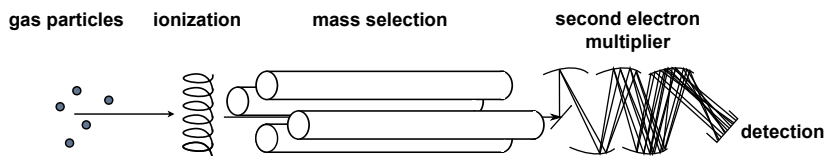


Figure 2.2: Scheme of a quadrupole mass spectrometer. The gas particles get ionized, pass a quadrupole where the desired molecules are filtered. The signal of these molecules is amplified with an electron multiplier to enhance the signal to noise ratio.

$$Z_w = \frac{p}{(2\pi mk_B T)^{1/2}} \quad (2.1)$$

Thus, at a pressure of 10^{-6} mbar every second all surface sites would have interacted with molecules from the gas phase (considering a temperature of 300 K). If a molecule would possess a sticking coefficient of 1 that would mean that every second the sample would be completely contaminated. Therefore, at a pressure of 10^{-11} mbar the time to contaminate the surface completely is extended to 24 hours. To pump down to the desired pressures not only a good pumping system is mandatory. If an opening of the chamber was necessary, the chamber is heated up to 100°C to 130°C for 24-48 h while being pumped. This promotes the desorption of contaminants (especially water) from the inner chamber walls which will always be present after chamber venting. The pressure is measured with a Bayard-Alpert ionization pressure gauge. Standard surface science tools are equipped within the chamber: A commercial leak valve, two pinhole dosers to dose different gases on the one and water on the other hand onto the surface. An electron beam evaporator (EFM 3 from FOKUS gmbH) with a graphite crucible filled with Mg rods allows to evaporate magnesium. To quantify the amount of evaporated metal a quartz microbalance (XTM/2 from Inficon) on the one and an ion flux monitor inside the evaporator was used. The chemical and structural quality of the sample was evaluated by studying the LEED-patterns and Auger spectra from the sample with a LEED-optic from Vacuum Science Instruments GmbH.

To examine photochemical processes similar to the ones described in chap-

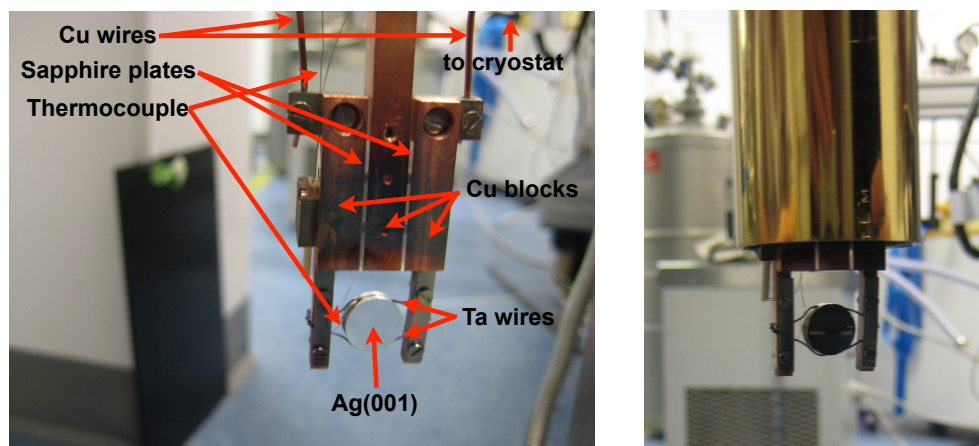


Figure 2.3: The sample holder without (left) and with the radiation shield (right).

ter 1.2 it is mandatory to quantify the absolute amounts of the product and the educt. To gain this information a Feulner-Cup shielded Quadrupole mass spectrometer (QMS) was used. A schematic view of a QMS is shown in Fig. 2.2.

The HrEELS spectra of MgO and N₂O on MgO were recorded in the UHV chamber described in the diploma thesis of Matthias Koch (see Ref. [79]) was used and modified. The surface analysis and manipulation tools shown in Fig. 2.1 were mounted on the preparation chamber. Moreover, the sample holder which will be described in the next section was attached to a HVK-STM Helium cryostat from Vab Vakuum-Anlagenbau GmbH.

2.1.1 Sample holder and manipulation

The most important part of a UHV chamber is the sample itself: Almost every manipulation and detection tool is centered around it. This makes the design of the sample holder a crucial topic. It is designed in a way that not only translation in all axes and rotation of the sample around the z-axis as defined by the cryostat is possible but also to manipulate the sample temperature between 20 K and 700 K; cooling down is achieved with a Janis Supertran LHe cryostat ST 400 and heating the sample up with a resistance heater. The temperature is controlled by a Lakeshore temperature controller which makes it possible to control the samples' temperature and heating rate. The samples' translation is realized by using a XYZ manipulator with computer-controlled OMNIAX stepper motors while the sample rotation is realized by a differentially pumped rotation stage. It is thus possible to move the sample over a range of 25 mm in the x and y directions, over 200 mm in

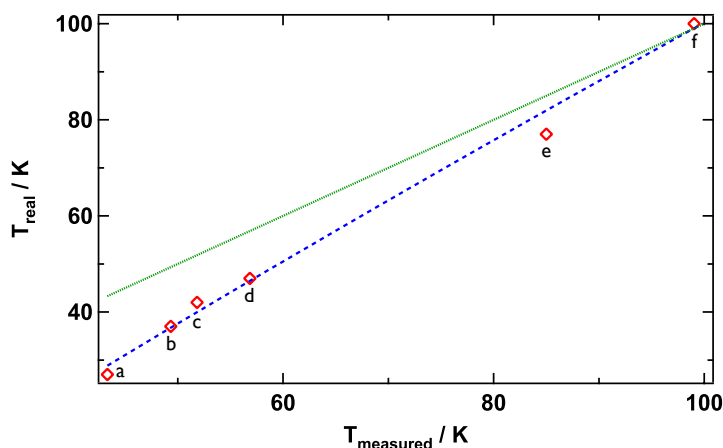


Figure 2.4: Low temperature correction of the measured temperature. The known desorption temperatures of different compounds are used as a tool for a polynomial fit (blue, dashed) to convert the measured temperature into an actual one. The green line serves as a guide to the eye to show how the measured temperatures deviate from the real ones. The peaks are denoted as follows: a.) N_2 multilayer, b.) CH_4 multilayer, c.) N_2 monolayer, d.) CH_4 monolayer, e.) N_2O multilayer, f.) N_2O monolayer.

the z direction and to rotate it around 360 degrees.

The sample holder was designed based on [80, 81] and is shown in Fig. 2.3. The cryostat is terminated by a gold sputtered copper head. A highly polished Cu block, forming the basis of the sample holder is attached to the cryostat. The cryostat is always connected to the ground thus the sample had to be *electrically* isolated from but *thermally* connected to the cryostat; a resistance heater must not be connected to ground while the cooling properties of the cryostat were desired to be used in an optimal fashion. This was realized by attaching two symmetrical copper blocks to this middle part, electrically isolated by sapphire plates. With a volume resistance of $\approx 10^{14} \Omega \text{ cm}$, sapphire is a good electrical isolator. However, its thermal conductivity is about $42 \text{ W m}^{-1} \text{ K}^{-1}$ at 300 K and increases for lower temperatures, thus Sapphire has a thermal conductivity comparable to metal but an electrical resistivity of glass. Current between these copper blocks flows only over the sample which is fixed by two tantalum wires. With two Kapton-insulated copper wires the sample can be heated by resistive heating.

The sample temperature was measured with a pair of type K thermocouples. For low temperatures the linear correlation between U and T_2 is no longer valid. To solve this problem, the TPD spectra from well-known gases adsorbed on MgO

were recorded and its desorption peaks were calibrated with values known from literature [82–85]. The expected temperatures of the mono- and multilayerpeaks are plotted over the real one and fitted with a polynomial, as shown in Fig. 2.4.

The sample holder was modified in several ways: Between the cryostat and the sample holder gold foil was inserted to optimize the thermal conductivity. Not only the tantalum wires but also the copper wires of the resistance heater were chosen as thin as possible. That reduced the interaction with the regular room temperature without reducing the heating power significantly. Finally, a gold-sputtered radiation shield made of copper was installed to reflect radiation which would heat up the sample. Without these optimizations, only temperatures of about 45 K were possible. By applying these modifications, however, temperatures as low as 20 K were obtained- a prerequisite to adsorb very loosely physisorbed molecules such as nitrogen, methane or carbon monoxide.

2.2 Excimer Lasers

To excite electron hole pairs, as explained in chapter 1.2, photons with energies significantly larger than 4.0 eV are needed to excite different surfaces sites of a MgO substrate. Table 2.1 depicts the used light sources and their respective photon energies and wavelengths. To guarantee a monochromatic light source with a high photon density lasers instead of a Hg-Lamp were chosen. The used excimer lasers from Neweks are small, easy to use and very stable. These properties make them shareable between several laboratories. The most regular maintenance procedure (about every two weeks depending on usage) is refilling the gas vessel with excimer gas. With a constant photon density per pulse (depicted by the measured pulse Energy E_{pulse}), a pulse frequency ν , the photon energy E_{photon} and a varied irradiation time t , the number of incident photons $n_{photons}(t)$ was calculated:

$$n_{photons}(t) = t\nu \frac{E_{pulse}}{E_{photon}} \quad (2.2)$$

where E_{pulse} is the Energy per pulse which is measured by a pyroelectric detector and ν is the pulse frequency. As most of the used lasers were Excimer lasers, a short introduction into the principle behind excimer lasers is given here. Excimer molecules exists only in an excited state ¹. This characteristic is used in excimer

¹Technically an Excimer is a homonuclear metastable molecule - an excited dimer -, whereas a heteronuclear metastable molecule is called an Exciplex but this differentiation is barely used.

Table 2.1: Used light sources

Used light source	wavelength / nm	Energy / eV
ArF	193	6.4
KrF	248	5.0
4ω Nd:YAG	266	4.6
XeCl	308	4.0

lasers: as the molecule is metastable, its ground state population will always be empty.

2.3 Temperature programmed desorption (TPD)

In chapter 1.3.3 the main principles of temperature programmed desorption spectroscopy were discussed in the context of surface thermodynamics. The discussion will be extended here. The first section is a discussion of a so-called Feulner cup which was built and used in this thesis to enhance the signal to noise ratio of TPD spectra. In the second section, the thermodynamical analysis of TPD spectra is discussed.

2.3.1 Signal amplification by Feulner Cup shielding of the mass spectrometer

Since no high reaction yields are expected it was mandatory to obtain a signal to noise - ratio as good as possible. A common strategy is to install a so-called Feulner-cup [86, 87].

Fig. 2.5 a.) illustrates the different influences on the quality of the recorded spectrum. At a specific temperature T molecules desorb from the surface with a desorption rate described by the Polanyi-Wigner equation eq. 1.23. The angular distribution of the desorbing particles is proportional to $\cos(\theta)$, thus dependent on the distance between the QMS and the sample, a part of the desorbing particles is not detected. The gas at the ionizer has a finite ionization probability and even if ionized, the gas might not be detected. Moreover, other desorption processes from e.g. chamber walls or from the cryostat might add noise. To conclude, there are a lot of possibilities which reduce the quality of the recorded spectra.

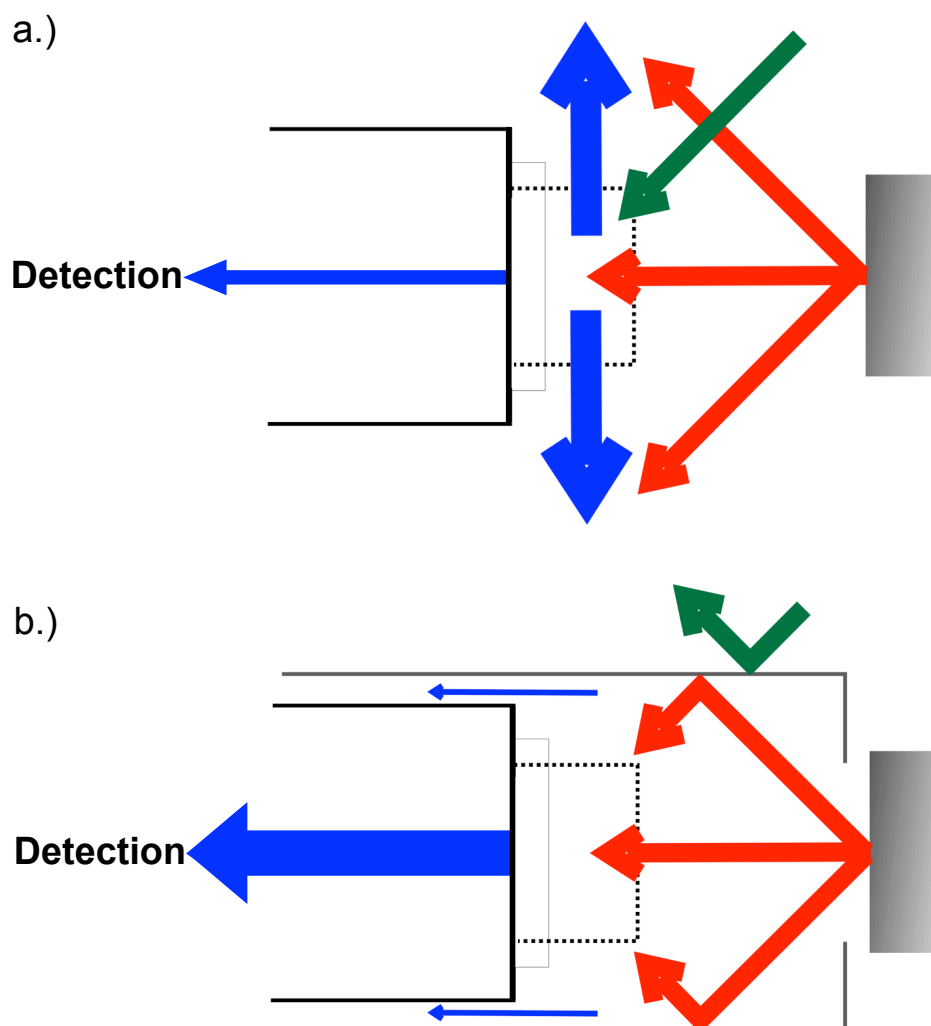


Figure 2.5: Scheme of molecule detection a.) without and b.) with a Feulner cup. The red arrows denote molecules desorbing from a surface, the blue ones ionized molecules and the green one molecules desorbing from other parts inside the UHV chamber e.g. the cryostat. As illustrated, the implementation of a Feulner cup minimizes the influence of desorption processes from other places than the sample and maximizes the signal; on the one hand by reducing the propagation probability away from the detection, on the other hand by increasing the residing time of the molecules at the ionizer.

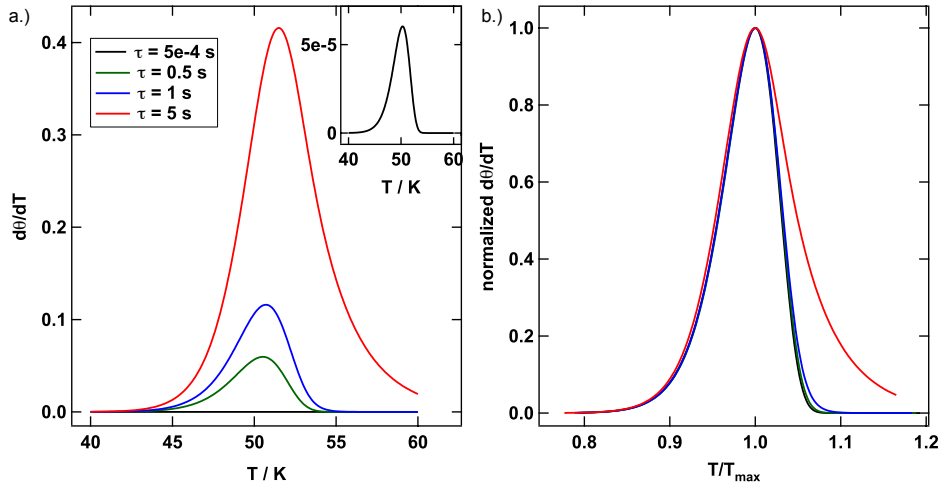


Figure 2.6: Simulated TPD spectra (obtained by solving eq. 2.3 illustrate the signal amplification with a Feulner cup. a.) shows absolute values, b.) a normalized picture. As illustrated, a higher τ leads to a higher signal (see a.), but, however, at the cost of the desorption trace itself (See b.).

However, positioning the sample close to the ionizer and shielding the QMS (which is then called Feulner cup) (see Fig 2.5 b.)), all of the mentioned influences can be minimized.

This signal amplification and its limits can be illustrated by extending eq. 1.23 by a contribution of the slowed down pumping speed [88] which distorts the pressure increase:

$$p(T) = \tau\beta\left(\frac{r_{des}(T)}{\theta_0} - \frac{dp}{dT}\right) \quad (2.3)$$

Here, $\tau = S/V$ is the characteristic pumping time, $r_{des}(T)$ the desorption rate in dependence of T , θ_0 the initial coverage and dp/dT the pressure change in dependence of temperature. In this model, the influence of a reduced pumping time is characterized by $\tau = S/V$, the quotient of the pumping speed and the volume. Solutions for different τ values are depicted in Fig. 2.6. As illustrated there a higher τ results in a better signal and leads to a significant amplification. However, the normalized versions of these plots show that too large τ values result in a distorted desorption behavior. Thus the aim is to construct a Feulner cup which amplifies the signal as much as possible without distorting the desorption behavior.

For the design of the Feulner cup the evacuation time τ was estimated (by referring to standard literature [89–91]) and compared it to the one constructed by Den-

zler et al. whose amplification properties were known [92]. To do so, the pumping time for the volume of a (hypothetical) Shield around the quadrupole mass spectrometer is calculated which is without a Feulner cup $\tau_{chamber} = 1 \cdot 10^{-4}$ s. With a Feulner-Cup, however, this pumping time was increased to $\tau_{Feulner} = 7 \cdot 10^{-3}$ s. Thus, the pumping time is seventy times as long with a Feulner-Cup than without one which means that the measured signal is about as magnified as well. That is about the same magnification that Denzler et al had achieved and does not distort the signal yet.

2.3.2 Analysis of TPD spectra

There are numerous ways to analyze TPD spectra and oftentimes, new ones are presented. A good overview over well known analyzing methods is written by A. de Jong and J. Niemantsverdriet [77, 93], but other ones are also emerge up to this day [88, 94–98]. Another, much more involved method is to simulate the diffusion and desorption kinetics on a surface with a Monte-Carlo approximation [99–102]. The advantage is a (simulated) direct transition from microscopic processes to kinetic parameters of a thermodynamic ensemble (which might make it possible to quantify desorption processes of coadsorbates). However, Monte-Carlo methods are very demanding concerning computer power. Moreover, the surface-adsorbate and intra-adsorbate interactions for each molecule have to be assumed. That is the reason why the focus is here on more simple analysis techniques. Both presented techniques - The Redhead Equation and the inverted Polanyi-Wigner plot - are based on the supposition that the thermal desorption can be described by the aforementioned Polanyi-Wigner equation. Especially for coadsorbates this rule is more a broad approximation. However, since the general trends of a coadsorbate (e.g. lateral interactions for a coverage-dependent desorption energy) can be illustrated in a straightforward manner and since the methods show good results for pure adsorbates, the advantages outweigh this aforementioned disadvantage.

Redhead Analysis

A very simple method to analyze TPD spectra is the Redhead Equation [76]. With a guessed desorption order and pre-exponential factor the desorption temperature is converted into a desorption energy. The Redhead equation itself is

$$E_{des} = RT_m(\ln(\nu T_m/\beta) - 3.64) \quad (2.4)$$

The Redhead equation describes the desorption energy E_{des} in terms of the molar gas constant R , the temperature of the peak maximum in the TPD spectra T_m , the frequency factor ν and the heating ramp β . The factor 3.64 is approximately $\ln(E_{des}/RT_m)$. This conversion might be a good starting point for the analysis of TPD spectra, however, it provides only a rough estimate for the desorption energy.

Inverted Polanyi-Wigner plot

This analysis method is based on the method frequently used by Dohnalek et al. [85, 103]. In analyzing the raw TPD spectra, the Polanyi-Wigner equation 1.23 is applied directly. However, instead of plotting the desorption rate $r_{des}(T)$ the desorption energy in dependence of the coverage is plotted i.e. $E_{des}(\theta)$:

$$E_{des}(\theta) = -RT \left(\ln \left(\frac{r_{des}(T)\beta}{\nu\theta^n(T)} \right) \right) \quad (2.5)$$

The application of this formula to the raw data is straightforward since $r_{des}(T)$ is known and $\theta(T)$ is quickly derivable by integrating the TPD spectra. A typical inverted Polanyi-Wigner plot looks as depicted in Fig. 2.7.

A problem arises when estimating of the frequency factor ν . The absolute value is not directly visible in the raw data (such as the desorption order n). Dohnalek et al solve this problem by choosing a frequency factor in such a manner that the desorption traces for different coverages perfectly fit together. The problem here is that they assume this factor to be constant - an assumption which is, especially on surfaces with different binding sites as an oxide, not at all expected to be true.

However, a good estimation can be extracted by comparing different inverted Polanyi-Wigner plots for different guessed frequency factors. If the coverage dependence of the energy in eq 2.5 is slightly modified, the influence of an error on the spectra can be modeled. Since the frequency factor is usually very high, only a modification of the exponent is applied with $\nu = 10^{x+x_{err}}$:

$$E_{des}(\theta) = -RT \left(\ln \left(\frac{r_{des}(T)\beta}{10^{x+x_{err}}\theta^n(T)} \right) \right) \quad (2.6)$$

With this extension, the influence of a incorrectly guessed frequency factor can be estimated. In Fig. 2.7 a simulated TPD spectrum ($E_{des} = 15$ kJ/mol, $\nu = 10^{13}$ s⁻¹ and $n = 1$) was converted into several inverted Polanyi-Wigner plots with different assumed frequency factors. As Fig. 2.7 shows, a correctly guessed frequency factor ν leads after conversion to the expected constant desorption energy while deviating

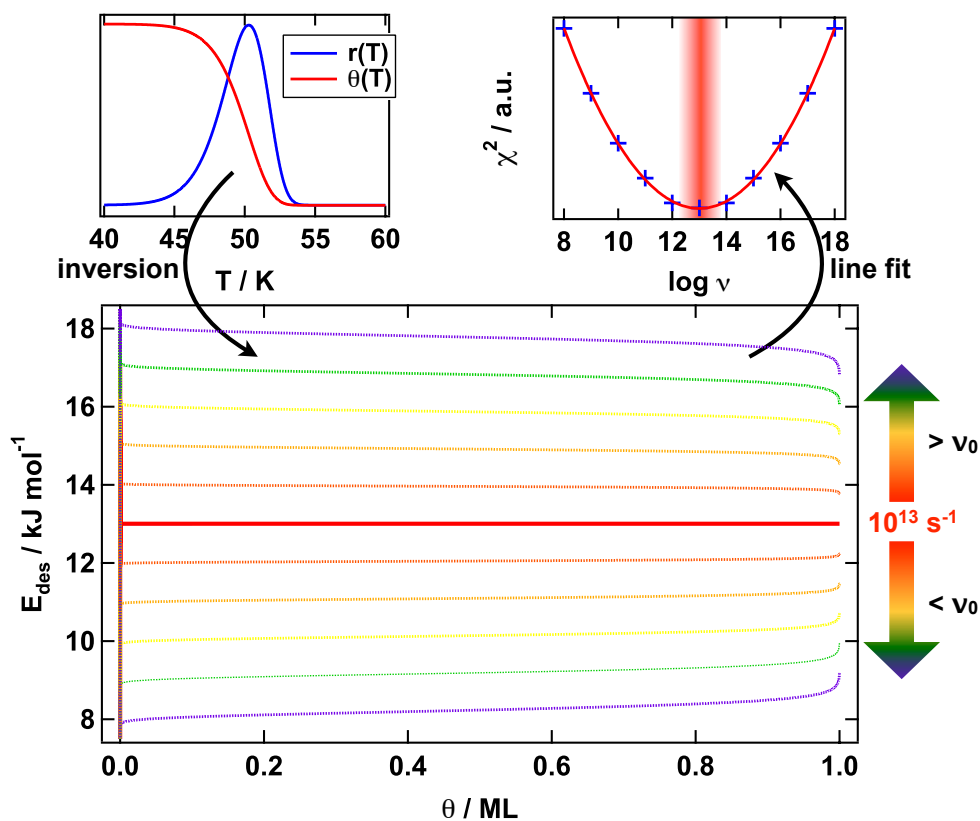


Figure 2.7: Scheme of thermodynamic analysis of TPD spectra: the desorption rate $r_{des}(T)$ and the coverage $\theta(T)$ of a simulated TPD spectrum are transformed to $E_{des}(\theta)$ via eq. 2.5. Different assumptions of ν lead to different traces, however, the correct assumption concerning ν lead to the best agreement with a line fit for $E(\theta)$ ($\theta = 0.2 \text{ ML} - 1.0 \text{ ML}$), indicated as a χ^2 value in the upper right panel.

initial ν values lead to an incorrect coverage dependence of the desorption energy².

As shown, it is possible to obtain reasonable frequency factors for *single* desorption traces by comparing different ν assumptions and see which agrees best with a linear fit (and thus extending the inverted Polanyi-Wigner analysis presented by Dohnalek et al). In that way, it is possible not only to estimate the desorption energy, but also the frequency factor as a function of coverage.

2.4 Electron energy loss spectroscopy (EELS)

The study of photochemical reactions on a surface with TPD is an acceptable method to deduce the quantities prior to and after irradiation, however, as already pointed out, this spectroscopy method lacks the possibility to gain insight into processes prior to desorption. Different methods of electronical and optical spectroscopy (or magnetical, as presented in chapters 2.5 and 5.4) serve this purpose. In the presented study high-resolution electron energy loss spectroscopy (HrEELS) was chosen; the excitation with electrons is not limited by selection rules as IR- or Raman-spectroscopy thus more vibrations are detectable. Moreover, in contrast to Electron Paramagnetic Resonance spectroscopy, the signal is not dependent on the presence of a free spin and would in that way extend the view onto processes of diamagnetic species on the surface. Finally, a large range of excitations (15-1000 meV) is accessible. Within that range, surface phonon modes and adsorbate vibrations can be studied.

The general approach in electron energy loss spectroscopy is straight forward to describe: Electrons with a small energy distribution are focussed at a sample of interest and the reflection of these electrons is detected. Beside the expected reflection of this electron distribution - which is referred to as *elastic peak* - electron losses caused by interactions with adsorbate molecules and surface phonons lead to distinct signals. Fig. 2.8 shows the HrEELS-spectrum of CO on Cu(001). The signal of interest is very small compared to the elastic peak. As shown later, this problem is even more strongly enhanced if the substrate is not a metal but an oxide, whose surface phonons distort the complete energy loss spectrum.

Fig. 2.9 shows how the used HrEELS-spectrometer is build up. An electron beam is generated by use of a cathode. Three electronical lenses after the cathode,

²It has to be pointed out that strong lateral interactions or sites with different adsorption energies lead to a coverage dependence of the desorption energy. However, a distinction has to be made between the artificial coverage dependence of E_{des} due to a wrong frequency factor and the influence of different adsorption sites or a coadsorbate.

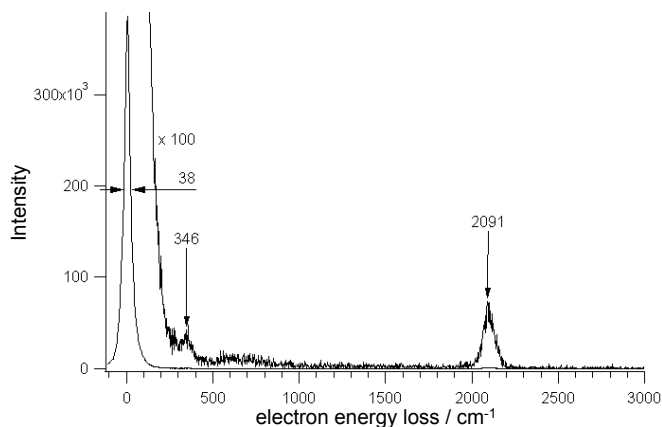


Figure 2.8: HREELS spectrum of CO/Cu(001) to illustrate how an EELS spectrum looks like. The spectrum is dominated by the elastic peak while small side peaks appear at distinct positions. These positions are correlated to adsorbate vibrations, in the present case at 348 cm^{-1} (symmetric stretch vibration of molecule to surface) and 2091 cm^{-1} (symmetric intramolecular stretch vibration of CO). This picture is taken from Ref. [79].

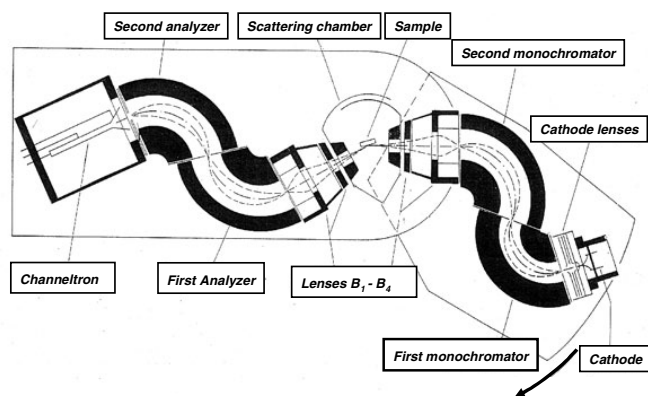


Figure 2.9: Schematic representation of the used EELS spectrometer. An electron beam is generated by a cathode and filtered by two monochromators, two analyzers and lens systems after the cathode and around the sample. Detection of the filtered electron beam is achieved by a channeltron. This picture is taken from [29].

two monochromator optics and two lenses afterwards focus the electron beam further before the electron beam is reflected by the sample. The sample itself is set on a potential chosen so that the difference between the work functions of the sample and the scattering chamber walls are minimized. In that case a homogenous potential interacts with the electron beam and the signal becomes less distorted. After being reflected at the surface, the electron beam passes again two lenses and two monochromators (in the picture called analyzers) before the electron beam is finally detected by a channeltron. The analyzer part behind the sample may be rotated. By tilting the angle between monochromator and analyzer parts, specular and off-specular electron scattering can be distinguished. *Specular* orientation detects the directly reflected electrons, thus this orientation is the perfect orientation between monochromator, sample and analyzer. *Off-specular* orientation, where the analyzer part is rotated slightly out of the specular orientation detects only scattered electrons.

The four monochromator-units are 127° deflectors. Its purpose is the generation of a monochromatic electron beam. A voltage between their inner and outer walls induces radial electric fields in such a way that only electrons with a distinct energy may pass the monochromator unit.

With the used setup, a resolution better than 33 cm^{-1} would be achievable, as defined by the half-width of the elastic scattering of electrons. As pointed out later, however, MgO films grown on Ag(001) are very rough for thicknesses larger than 4 ML which is the reason why in the presented experiment only a resolution of 80 cm^{-1} was achievable; surface roughness has a large influence on the detected electron distribution. It has to be pointed out, though, that this dramatic decrease of resolution is not uncommon on MgO surfaces [104].

When being reflected at the surface, three types of interactions modify the monochromatic electron beam (see Fig. 2.10):

- long-range ($\approx 100 \text{ \AA}$) electric fields induce *dipole scattering*
- short range *impact scattering* ($\approx 1 \text{ \AA}$) due to the presence of atomic potentials
- resonances with molecular orbitals might induce *resonance scattering*

The latter one is of particular interest for interactions with molecules in the gas phase and thus is not expected as a dominant influence here.

Dipole scattering can be described by dielectric theory as inelastic electron scattering. The underlying reason for this mechanism are surface excitations by

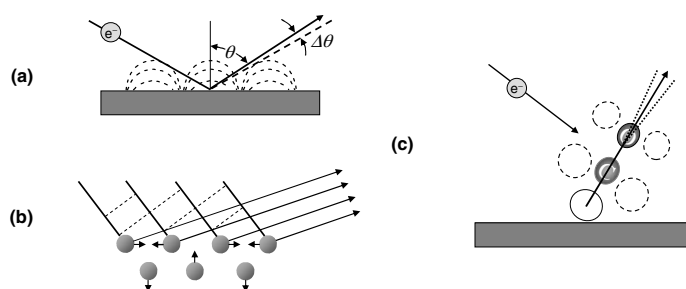


Figure 2.10: The three scattering mechanisms of electrons on the surface are shown. The picture is taken from [29]. a.) dipole scattering b.) impact scattering c.) resonance scattering.

absorption of energy from the incident electrons' electric field: Electrons interact with dipole moments and excite vibrations in this process. Phonons, plasmons and adsorbate vibrations are excited in that manner. A small momentum transfer leads to a small angular distribution between inelastically scattered electrons and the specular direction. It is stressed again though that the preparation conditions like a defective surface broaden this distribution artificially.

Impact scattering is the scattering of electrons by the atomic potential of the substrate and adsorbate atoms. The mechanism is described by a short range coulomb interaction. In contrast to dipole interaction, a large momentum transfer leads to a large angular distribution which makes it possible to discriminate between both excitation mechanisms; an off-specular measurement would only show distributions from angular scattering. The cross section is 2-3 orders of magnitude smaller than the cross section for dipole scattering so much smaller signals are to be expected.

2.5 Electron paramagnetic resonance (EPR)

As chapter 5.4 deals with the the examination of the free spin evolving in the course of photochemistry, the principle of Electron paramagnetic resonance spectroscopy is described here. For a more in-depth description not only of the theory behind EPR but also of the used experimental setup, the reader may refer to the thesis of

Anastasia Gonchar [105].

EPR spectroscopy makes it possible to detect and study the local topology of chemical species with one or more unpaired electrons. Thus EPR is the method of choice for studying radical species, as in the presented case on oxide surfaces. The method is widely applied and its use dates back to the first measurements in oxide chemistry (for a good overview see the Proceedings of a symposium in memory of Dr. A. J. Tench [106]).

Consider an electron with a spin $s = 1/2$. This spin is accompanied by a magnetic component $m_s = \pm 1/2$. The Zeeman effect results in an antiparallel or parallel orientation of this magnetic component to an external field and thus a splitting of the corresponding energy levels:

$$\Delta E = E_{1/2} - E_{-1/2} = g_e \mu_B B_0 \quad (2.7)$$

Here, μ_B is the Bohr magneton, B_0 the strength of the used magnetic field and g_e denotes the g-factor. This g-factor is for a free electron ≈ 2.002 but is significantly influenced by the surrounding environment: The angular momentum of an electron can change due to the presence of a local magnetic field causing a change in the g-factor.

In a strict sense, the g-factor is not a scalar, but a tensor which corresponds to the topological influences on a free spin. A suitable representation of this is in form of a three-dimensional matrix with principal axes determined by a local field. A diagonalization makes it then possible to represent the g-value in three components g_{xxx} , g_{yyy} and g_{zzz} . In the case of axial symmetry, the tensor is even further reduced to a parallel and a perpendicular component of g, named g_{\parallel} and g_{\perp} , respectively, with respect to the magnetic field.

EPR spectroscopy thus works as follows: Either a tunable microwave field is applied perpendicular to a fixed magnetic field or vice versa. The probe is located in the center of both fields. At distinct frequencies the condition of eq.2.7 is fulfilled which leads to the absorption or emittance of a microwave photon.

Chapter 3

MgO films grown on Ag(001)

3.1 Preparation and characterization of MgO films

The Ag(001) single crystal was purchased from Surface Preparation Laboratories. It is aligned to 0.1° and polished so that the roughness of the crystal is 300 \AA or better. Contaminations of this polishing procedure were initially still present on the crystal, so an extensive cleaning procedure consisting of ten or more sputtering (i.e. bombarding with Argon ions) and tempering (annealing up to 650 K for 30 minutes) cycles was mandatory. After this initial cleaning procedure the regular sample preparation consisted only of one of these cycles. The quality of the crystal was verified by LEED and Auger electron spectroscopy.

As discussed in chapter 1.1.3, MgO films thinner than 4 ML are expected to possess surface properties different from bulk MgO. After the surface is cleaned, MgO films with different thicknesses ranging from 4 ML to 30 ML were prepared onto the Ag(001) crystal by reactive deposition of magnesium in an oxygen atmosphere with a partial oxygen pressure of $2 \cdot 10^{-6} \text{ mbar}$. The sample was held at a temperature of 600 K so that the MgO-films can relax and grow as flat and defect free as possible. The nominal thicknesses were calibrated with a quartz microbalance by measuring before and after evaporation onto the crystal the deposition rate. This preparation method is widely used in literature [83, 107]. Again, these thin films were again controlled concerning their geometrical and chemical quality by means of LEED and AES.

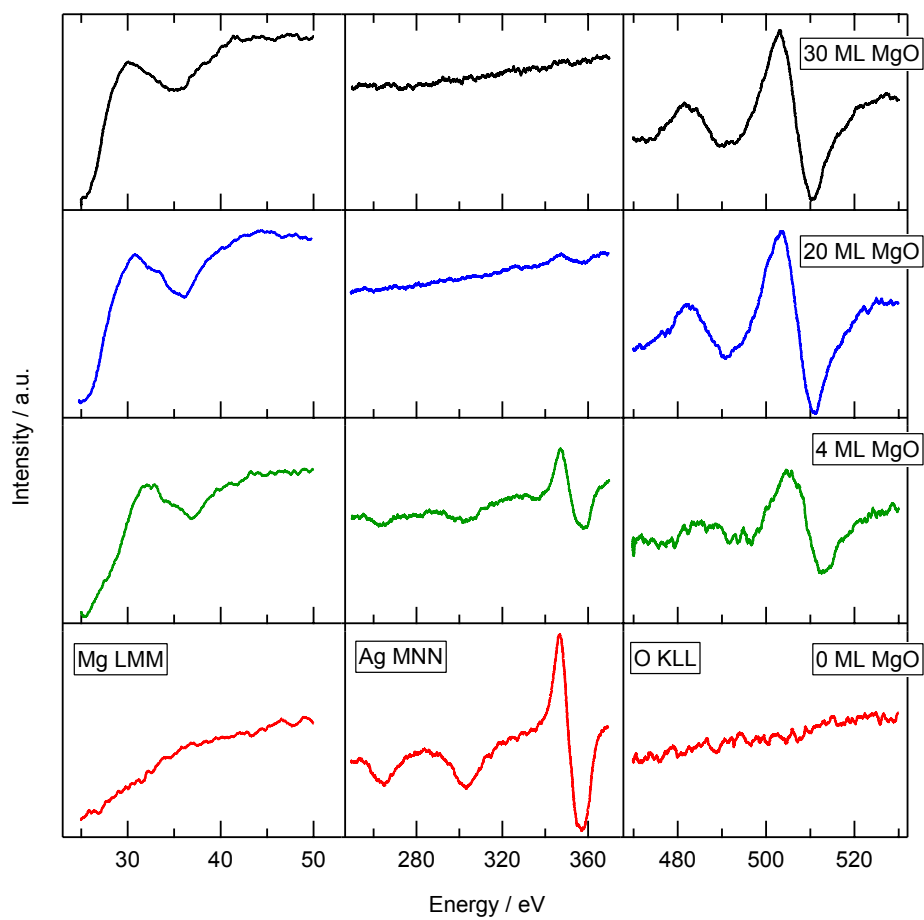


Figure 3.1: Signal dependence of the Mg LMM, Ag MNN and O KLL lines in the Auger electron spectra of MgO films grown on Ag(001). The MgO thickness was between zero and thirty monolayer. Neither the crystal nor the films grown on top of this crystal were contaminated.

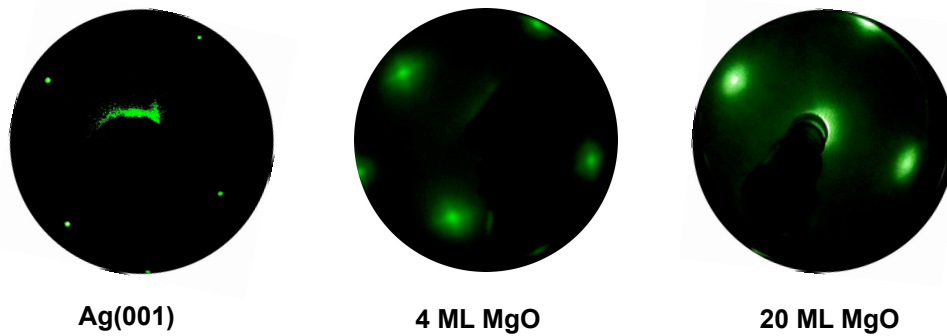


Figure 3.2: LEED pictures taken at a primary electron energy of 50 eV from sputtered and annealed Ag(001), 4 ML and 20 ML MgO films grown on the silver crystal. A four-fold symmetry appears for thin films but vanishes for thicker ones.

3.1.1 Chemical characterization of the Sample

The main purpose of the chemical characterization of the sample which was done by applying Auger Electron spectroscopy is to verify its purity. Auger electron spectroscopy is a standard procedure to do that. With a primary beam energy of 1000 eV the mean free path of the electrons is about 20 Å, so that the topmost layers of the crystal are investigated. For thin films more things might be concluded from the Auger spectra in referring to the limited penetration depth: As Fig. 3.1 shows, a small remnant of the silver signal is still visible at 20 ML (or about 40 Å). As the thickness of the grown MgO film exceeds the penetration depth of the Auger electrons significantly, it is surprising to see a silver signal at these thicknesses. This phenomenon can be explained by referring to the deposition temperature: At this temperature, the underlying silver is already hot so that small silver clusters are able to diffuse in the MgO film see [64]. This influence decreases with film thickness which is one of the reasons why most presented measurements were done with rather thick (20-30 ML) films where no more silver contaminations are to be expected at the surface.

3.1.2 Study of the LEED-pattern for Ag(001) and MgO

The small lattice mismatch between Ag(001) and MgO(001) leads to a similar spatial distribution of the diffraction peaks (see Fig. 3.2). For thin MgO-films, a square-like shape of the LEED-peaks is visible. This is known as a fingerprint for the thin film growth mode of MgO [57, 108], see also chapter 1.1.3: As the

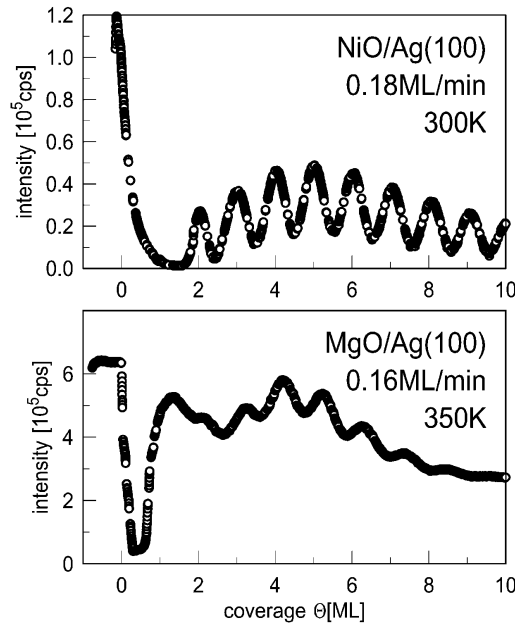


Figure 3.3: Spot intensity oscillations (SPA-LEED) for specular beam detection during film growth for NiO/Ag(001) and MgO/Ag(001). Even though an oscillatory pattern is visible for MgO, it is much more distorted than for NiO. This picture is taken from Ref. [57].

thin films relax by forming an interface dislocation oriented with respect to the Ag(001) structure (Wollschläger et al refer to them as "mosaic structure"). Thicker films, however, lose this four-fold symmetry and form broad peaks with no inner structure. The conclusion is that the surface roughens with increasing thickness and leading to smaller terraces (and in reciprocal space to larger spots).

As already presented in chapter 1.1.3, according to studies done before this thesis [57–59] the small lattice mismatch between MgO and silver should result in a flat film with a relaxing mosaic structure for thicker films. However, the complete opposite is detected: The MgO films become more defective with film thickness. This discrepancy to literature is explained by the low deposition temperature (600 K) which is, compared to the melting point of MgO (about 3000 K) very low. The relaxing influence of the small lattice mismatch, which plays a role for thin films, becomes less significant the thicker the film becomes. MgO films grown on Mo are known to be stable for up to 1300 K [109], while, as mentioned earlier, Ag already begins to diffuse into the MgO bulk at comparatively low temperatures. This leads to a non layer by layer growth for thick films. It should be pointed

out that SPA-LEED (Spot profile analysis LEED) measurements of MgO suggest a similar picture [57]: Albeit the specular beam intensity oscillates during MgO film deposition (the intensity maxima are correlated to a completely closed monolayer), this oscillation is, in contrast to the oscillation during NiO film deposition, significantly distorted, see Fig. 3.3. In fact, the oscillation amplitude becomes smaller than the noise at about nine monolayers revealing that no pure layer by layer growth is established and becomes worse for higher coverages.

3.1.3 Surface phonons of MgO

A characteristic feature in HrEELS-spectra taken from oxide surfaces are large contributions of optical surface phonons. The most well-known oxide surface phonons are known as Fuchs-Kliwer modes [110]. This mode represents a macroscopic surface phonon and corresponds to the vibration of the Mg and O sublattices against one another (in the case of MgO). Dielectric continuum theory predicts the presence of two dipolar modes known as FK^+ and FK^- . These two modes correspond to Fuchs-Kliwer modes at the surface and at the interface, respectively. As a metallic substrate was chosen to prepare MgO films, the latter mode is completely screened and supposed not to be observed. A second, microscopic surface phonon mode is the so-called Wallis mode [111] which corresponds to the microscopic perpendicular motion of oxygen atoms to the topmost layer. In table 3.1 the phonon modes with expected energy losses are listed.

The height and peakshapes of these losses contain structural information of the oxide surface: Wu et al had used HrEELS spectra to determine the stoichiometric quality of Al_2O_3 films grown on Re(0001) surfaces [112]: One certain phonon mode is in that sense expected to appear if the film is not completely oxidized. Moreover, a shift of the peaks with film thickness is visible. Thus, the examination of surface phonon modes was used to determine the quality of the investigated surface. Savio et al had investigated the generation of surface phonons of MgO grown on Ag(001) and the hydroxylation of MgO films at different film thicknesses [113, 114]. While the latter one mainly shows that no significant amount of OH-groups occurs at films thicker than 3 ML, the first one clearly confirms different phonon modes at different film thicknesses.

In the left subpanel of Fig. 3.4 a HrEELS spectrum of a 20 ML MgO on Ag(001) is presented. This spectrum was recorded during this thesis. The spectrum is dominated by large peaks at 670 cm^{-1} and 1340 cm^{-1} which both possess a shoulder at the left side. This peak can be interpreted as the fundamental and the first over-

Table 3.1: List of MgO surface phonons. The values are taken from Ref. [113]

name	energy loss / cm^{-1}
FK⁺	650
FK⁻	393
Wallis	524

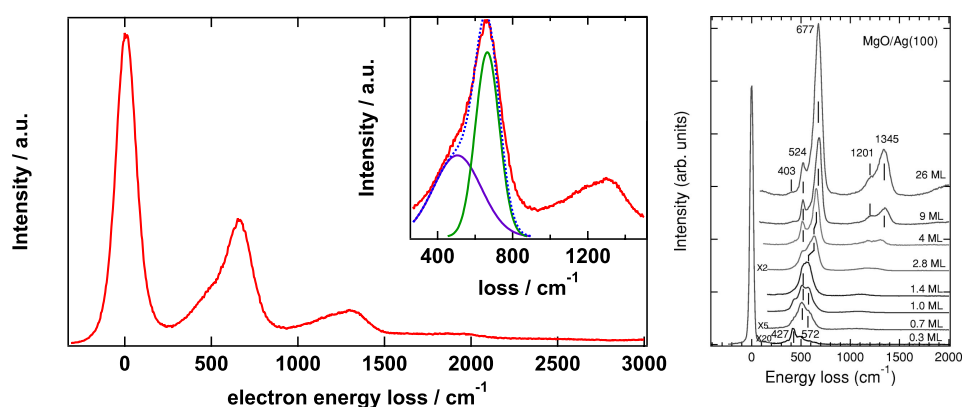


Figure 3.4: HREELS spectrum of pure MgO. As shown, large peaks at $n \cdot 670 \text{ cm}^{-1}$ ($n=1,2,3,\dots$) dominate the energy loss spectrum. These signals are huge in comparison to adsorbate-related losses and thus an impediment in the analysis of surface vibrations. Inset: the phonon signals consist of two peaks closely related to each other. The green one at 670 cm^{-1} is the signal of the FK^+ phonon mode while the shoulder at about 500 cm^{-1} is correlated to the Wallis-mode which appears at films thicker than 3 ML. The broader shape of this peak might be a fingerprint for a fourth, very weak loss at 400 cm^{-1} which is only present at thicker films (10 ML and more), see right picture (taken from Ref. [113]).

tone of a peak occurring periodically at $n \cdot 670 \text{ cm}^{-1}$ ($n=1,2,3\dots$) due to overtone excitations.

The large resolution Savio et al could obtain made it possible to resolve the substructure of the recurring peaks. With this knowledge, the nature of the peaks' shoulder in the left subpanel of Fig. 3.4 could be referred to the microscopic Wallis mode and possibly a third peak at 400 cm^{-1} . However, the nature of this third peak is not yet known. It might be a small remnant of the FK^- mode or due to the presence of lower coordinated oxygen sites of the MgO film.

When compared to theory, the FK^+ mode is significantly higher than expected suggesting a presence of compressive stress which might be referred to the growth mode of MgO on Ag(001).

Thus, an interpretation of the recorded HrEELS-Spectrum would be as follows:

- The absolute height of the recurring signals confirm a thickness of about 20 ML. For thinner films, smaller peaks would be expected.
- Moreover, the absolute peak height, when compared to theoretical calculations, serve as a fingerprint of the compressive stress the MgO film is exposed to due to the lattice mismatch with the Ag(001) substrate.
- The peak shape itself is a signal of both the FK^+ -mode and the Wallis mode. A third peak might also be at 400 cm^{-1} which possibly would serve as a fingerprint for lower coordinated oxygen sites on the MgO surface.

Summarizing, the surface phonon modes of MgO contain much information about the film thickness and the quality of the film. However, as these peaks are huge distortions of the EELS-spectrum, the adsorbate contributions are not detectable anymore: Fig. 2.8 shows that the signal of CO compared to the elastic peak is a small fraction of half a percent. A signal of CO on MgO would be completely lost in presence of surface phonons.

Minimization of phonon-induced distortion of HrEELS-spectra

To minimize or separate the multiple contributions of surface phonon losses, two well-known techniques exist¹: On the one hand, the measurement technique is altered by applying high energy electron beams and detect the losses in off-specular geometry. On the other hand, the spectra are recorded in specular geometry with

¹There are more recent approaches by applying maximum entropy [115, 116] or wavelet [117] methods which are not dealt with in this thesis.

regular electron beam energies, but during analysis the recorded data is modified. Both methods mainly suppress the *multiple* phonon contributions, i.e. the overtone excitations while leaving the fundamental surface phonon mode still significantly high. Thus, the strength of both methods lies within making adsorbate losses larger than 1000 cm^{-1} visible. Lower losses are in a region still dominated by the huge surface phonon fundamental.

The latter approach, the modification after obtaining the HREELS spectra, was chosen for two reasons: First, the impingement with high-energy electrons on an adsorbate might induce chemical reactions and thus distort the results dramatically. Second, the surface roughness results in a broad electron scattering which reduces the specularly-dependence of the elastic peak and the phonon contributions.

Thus, the recorded HREELS spectra are smoothed in form of a Fourier deconvolution [118–121]. This method was applied with success for various systems [122–124]. The mechanism was proposed by Cox et al in 1985 [118] and is based on the idea that the distortion of a signal is not simply added or multiplied to but *convoluted* with the unperturbed signal. This approach is well-known in signal processing: Pictures with a low signal to noise-ratio are deconvoluted to separate the pure signal. As a convolution is a multiplication in Fourier-space, it is reasonable to work with the Fourier-transform of the signal.

Consider a signal $s(\omega)$. This signal is the detected HREEL spectrum and in that sense the convolution of the "perfect" signal without any distortions $p(\omega)$ and the instrumental broadening function $i(\omega)$ i.e. the instrumentally induced distribution of the electrons:

$$s(\omega) = i(\omega) * p(\omega) \quad (3.1)$$

The instrumental broadening function $i(\omega)$ is typically approximated as the elastic peak. As the experimental HREEL spectrum does not only contain contributions from the single loss features but also from multiple losses resulting from overtone excitations, eq. 3.1 has to be specified as a series of self convolutions:

$$s(\omega) = i(\omega) * [\sigma(0) + p(\omega) + \frac{1}{2!}p(\omega) * p(\omega) + \frac{1}{3!}p(\omega) * p(\omega) * p(\omega) + \dots] \quad (3.2)$$

The Fourier transforms of $s(\omega)$, $i(\omega)$ and $p(\omega)$ are denoted as $S(\tau)$, $I(\tau)$ and $P(\tau)$, respectively. Since a convolution in real space is a multiplication in Fourier space, the Fourier transform of eq. 3.2 can be expressed as a power series of $P(\tau)$ times the instrumental broadening function $I(\tau)$. As the respective power series is the exponential function, the Fourier representation of eq. 3.2 is:

$$S(\tau) = I(\tau) \cdot e^{P(\tau)} \quad (3.3)$$

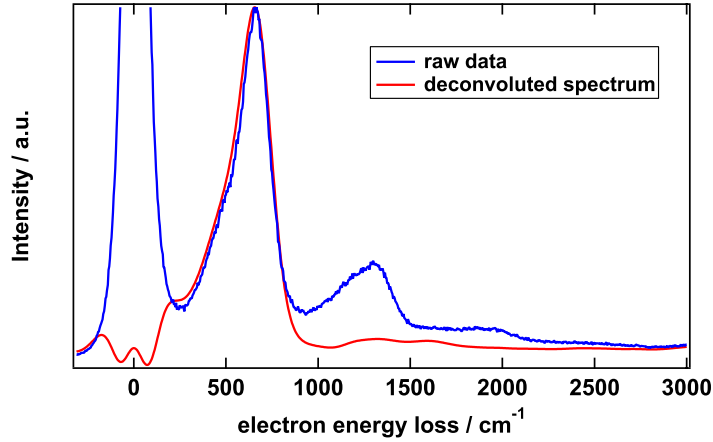


Figure 3.5: Fourier deconvoluted HrEELS spectrum of pure MgO is shown in red while the raw data is plotted in blue. As shown, the phonon modes with exception of the fundamental mode are almost completely suppressed. Moreover, the whole spectrum has a much better signal to noise ratio.

The isolation of the pure, realistic loss function $P(\tau)$ is now established. However, a simple back-transformation is not possible: If the instrumental broadening function is removed, high frequency Fourier ripples with a finite signal to noise ratio are introduced into the data. To solve this problem a smoothing function $I'(\tau)$ is multiplied with $P(\tau)$, a distribution similar to the instrument function whose real space representation $i'(\omega)$ has a slightly larger FWHM (typically 10 cm^{-1}) than $i(\omega)$. That results in a smoothed loss function free of multiple losses:

$$P(\tau) = I'(\tau) \ln(S(\tau)/I(\tau)) \leftrightarrow p(\omega) * i'(\omega) \quad (3.4)$$

Fig. 3.5 shows the real HrEELS spectrum of MgO and its Fourier deconvoluted form. For better comparison both spectra were normalized with respect to the fundamental mode of the surface phonons. The Figure shows that the contributions of the phonon modes - except the fundamental mode - are dramatically reduced. Moreover, the signal to noise-ratio is dramatically enhanced.

3.2 Experimental procedures

In most measurements of this study, N_2O was dosed onto the sample (MgO/Ag(001)) at $T = 20 \text{ K}$, however, no differences in the adsorption characteristics of N_2O were detected if the adsorption temperature was below 70 K i.e. below the temperature

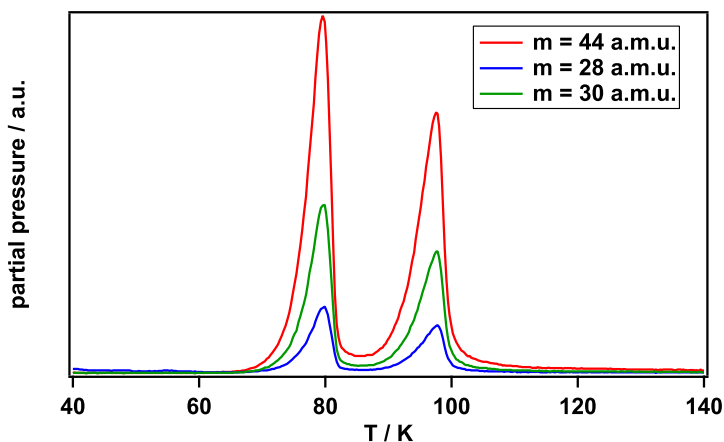


Figure 3.6: TPD spectrum of 2-3 ML N₂O on MgO. The TDS signal for 44,28 and 30 a.m.u. is shown as the these signals refer to the parent mass (N₂O) and its cracking patterns (N₂ and NO, respectively). The almost identical behaviour which differs only in a scaling factor shows that N₂O adsorbs intact on MgO.

for N₂O multilayer desorption. The TPD spectrum of 2-3 ML of N₂O dosed on MgO is shown in Fig. 3.6. The parent mass N₂O ($m = 44$ a.m.u.) and its main cracking patterns NO ($m = 30$ a.m.u.) and N₂ ($m = 28$ a.m.u.) differ only in a scaling factor which suggests intact adsorption of N₂O on MgO surfaces. The properties of N₂O adsorbate and the nature of the monolayer will be discussed in chapter 4.

For the photochemical studies, this experimental system was irradiated homogeneously with one of the aforementioned light sources. Most of the discussed experiments were done with a KrF laser thus the photochemistry at 5.0 eV is investigated more thoroughly than the other wavelengths. We note, however, that the general findings are, if not reported otherwise, identical for all used light sources. After irradiation, low temperature TPD spectra ($T = 20$ -160 K) were recorded with focus on the characteristic mass signals for N₂O (28,30 and 44 a.m.u.). The used temperature ramp was 0.5 K/s. Moreover, high temperature TPD spectra up to 650 K were recorded with focus on $m = 32$ a.m.u. to detect molecular oxygen resulting from recombinative desorption of pregenerated atomic oxygen. For a better signal to noise ratio, the used heating ramp was 1.5 K/s. Fig. 3.7 shows the low- and high-temperature TPD spectra with the same scale to illustrate how large the reaction yield is compared to the signal of the unirradiated N₂O monolayer.

Beside analysis and discussion of TPD spectra, two approaches to study the

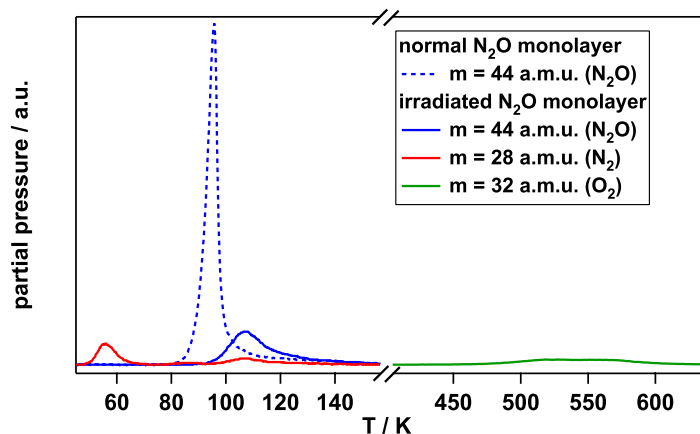


Figure 3.7: TPD spectra of N_2O ($m = 44$ a.m.u., red), N_2 ($m = 28$ a.m.u., blue) and O_2 ($m = 32$ a.m.u., dark green) after irradiation with $2 \cdot 10^{18}$ photons/cm². The dotted red line shows, for comparison, the TPD spectrum of one monolayer N_2O without irradiation.

generated oxygen prior to desorption were done: On the one hand the goal was to study N_2O vibrations on MgO on the one hand and atomic oxygen on the other by HREELS spectroscopy. The corresponding measurements were done in the working group of Prof. Teger, FU Berlin. In a second approach, EPR spectroscopy (in the former working group of Prof. Risse at the Department of Hajo Freund) was applied to study the generation and thermal stability of generated free radicals.

This general procedure was then extended by coadsorbing CO with pre-generated atomic oxygen and irradiate this new experimental system a second time (see chapter 6). After irradiation, CO_2 generation was recorded accompanied by a depletion of pregenerated atomic oxygen. This generated carbon dioxide was also recorded with a temperature ramp of 1.5 K/s.

Chapter 4

Adsorption of N₂O on thin MgO films

The main topic of this thesis is to investigate the photoinduced generation of atomic oxygen by dissociation of N₂O on thin MgO films. Before the photochemistry can be examined in detail, the adsorbate system itself has to be understood. At first, the related studies done before this thesis are presented, followed by a short discussion of HREELS measurements and TPD spectra acquired in this thesis. The final section will discuss the measurements with respect to the literature to draw a conclusion.

Britta Redlich studied the adsorption characteristics of N₂O on flat MgO surfaces by means of LEED and FTIR spectroscopy [30, 125]. The main conclusion from her data is that N₂O adsorbs flat on the MgO terraces with each end adsorbed on a Mg-ion. More important for this study is, however, that two adsorbate phases are expected to be present at the surface: One densely packed phase possesses a $(2\sqrt{2} \times \sqrt{2})R45^\circ$ structure. After annealing to over 88 K the adsorbate has re-ordered to a loosely packed 1×1 structure. Monte-Carlo calculations by Daub et al of a similar system, CO₂ adsorbed on MgO, suggest the same behavior [126].

In contrast, other studies conclude that N₂O adsorbs only in one monolayer phase: Lian et al studied IRAS - and TPD spectra of N₂O adsorbed on MgO [83]. The IRAS spectra show a single absorption at 1275 cm^{-1} which corresponds to the symmetric stretch vibration (ν_1) of N₂O and three absorption peaks at about 2250 cm^{-1} which are correlated to the asymmetric stretch vibrations (ν_3) of N₂O adsorbed at different surface sites of MgO. One vibration at $\nu_{3,a} = 2236 \text{ cm}^{-1}$ was more abundant on annealed MgO films than on films prepared at room temperature

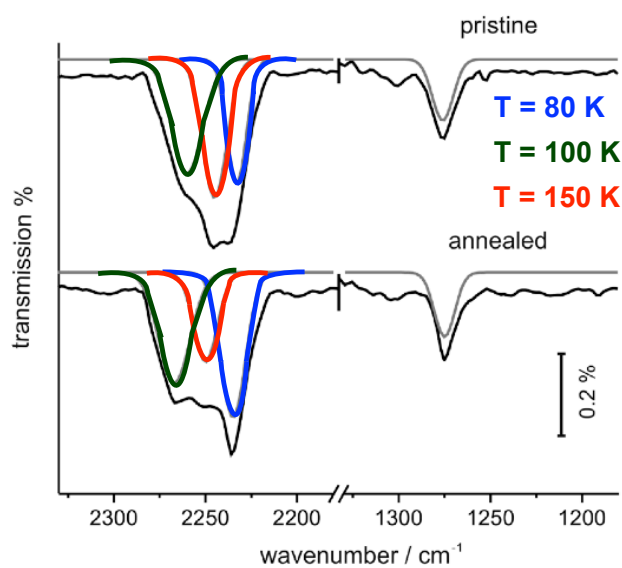


Figure 4.1: IRAS-spectra of N_2O on pristine and annealed MgO films. The spectra were recorded at a surface temperature of 60 K. The peak structure at 2200 cm^{-1} - 2300 cm^{-1} is referred to the ν_3 modes and the peak at 1275 cm^{-1} to the ν_1 mode of N_2O on MgO. The complex peak structure is fitted by gaussians. The signal at $\nu_{3,a} = 2236\text{ cm}^{-1}$ is significantly increased on annealed films thus it can be correlated to N_2O vibrations adsorbed on terraces while the vibrations at $\nu_{3,b} = 2249\text{ cm}^{-1}$ and $\nu_{3,c} = 2270\text{ cm}^{-1}$ are respectively correlated to N_2O adsorbed at defect sites. $\nu_{3,a}$ vanishes at $T = 80\text{ K}$, while $\nu_{3,b}$ and $\nu_{3,c}$ vanish at 100 K and 150 K , respectively. Picture taken from Ref. [83].

(see Fig. 4.1). Thus, the signal at $\nu_{3,a} = 2236 \text{ cm}^{-1}$ could be correlated to terraces, while signals at $\nu_{3,b} = 2249 \text{ cm}^{-1}$ and $\nu_{3,c} = 2270 \text{ cm}^{-1}$ were correlated to N₂O adsorbed on defects. The vibrations correlated to N₂O adsorbed on terraces, however, began to decrease after annealing to 80 K and vanished completely after annealing to 90 K while the other vibrations were more stable.

A theoretical study by Xu et al which supports this interpretation has calculated the N₂O desorption energies for N₂O on terraces as 21 kJ/mol and on edges as 24 kJ/mol [127]. Thus no additional adsorbate phase is expected in this study. The flat adsorption of N₂O on regular terrace- and edge sites, however, suggested in the study of Britta Redlich is confirmed theoretically as the adsorption energies for N₂O adsorbing with each end differ only slightly. Moreover, the calculations suggest that N₂O is adsorbed primarily with the oxygen end at oxygen vacancies. While no further calculations about N₂O adsorbed at divacancies are present, the similar electronic structure when compared to oxygen vacancies suggest that N₂O adsorbs similar in this case.

4.1 Vibration species of N₂O

HrEELS spectra of N₂O adsorbed on MgO were recorded. The raw data is shown in Fig. 4.2. While the adsorption of N₂O leads to a suppression of the primary electron beam and the overall spectrum, no further spectral features of N₂O were visible.

As discussed in chapter 3.1.3, the raw HrEELS data is dominated by multiple contributions of the surface phonon modes: No adsorbate contribution, except the reduced intensity of the elastic peak (and thus the overall spectrum) was visible in the raw data. Because of this reduced intensity the data was normalized with respect to the elastic peak before further analysis steps were taken.

To minimize the surface phonon contributions, the data is smoothed by a Fourier deconvolution (see chapter 3.1.3). After that step, the HrEELS spectrum reveals after N₂O adsorption different peaks (see Fig. 4.3). The peaks at 1280 cm^{-1} and 2250 cm^{-1} correlate with the IRAS-spectra discussed before (see Fig. 4.1). Additional peaks at 1900 cm^{-1} and 2510 cm^{-1} are not yet understood but might be remnant signals from the third and fourth overtone of the surface phonon modes. As the bending mode of N₂O ($\nu_2 = 588 \text{ cm}^{-1}$ [128]) is due to the presence of a huge surface phonon fundamental not visible, the peak at 220 cm^{-1} might be a small remnant of this bending mode.

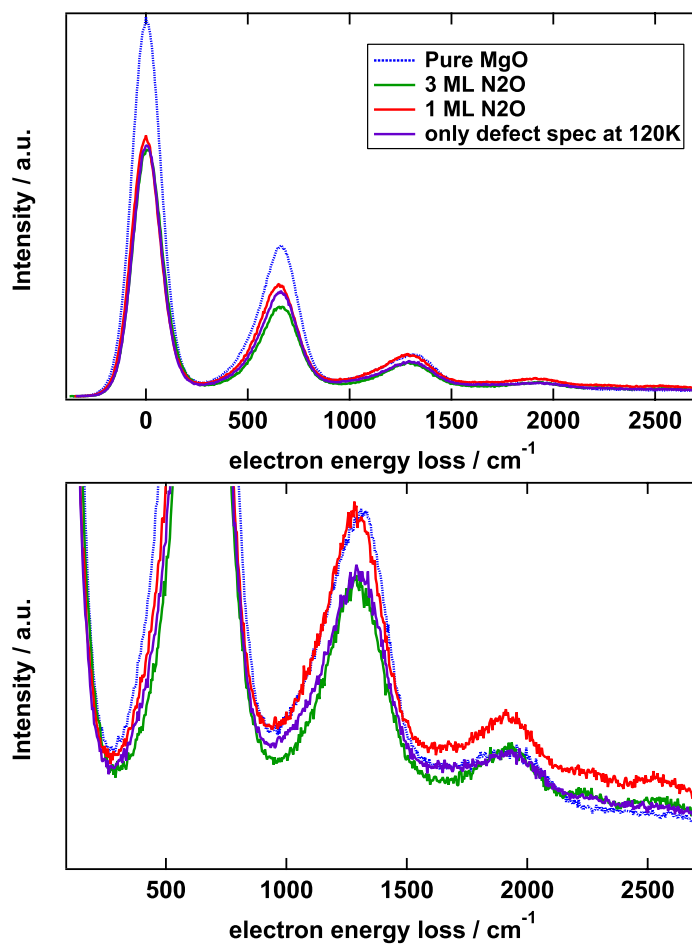


Figure 4.2: Raw HREELS spectra of different amounts of N_2O adsorbed on MgO films. As shown, the adsorbate leads to a suppression of the primary electron beam and thus the complete spectrum. The lower panel confirms that the raw data does not show any trace of N_2O yet.

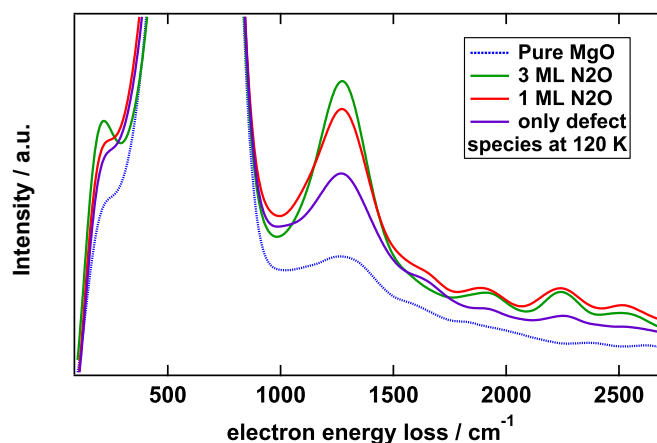


Figure 4.3: The deconvoluted HREELS spectra show at 1280 cm^{-1} and 2250 cm^{-1} signals when N₂O is adsorbed on MgO surfaces. Their spectral position and the thermal stability confirm the IRAS measurements by Lian et al [83]. Moreover, additional, IR inactive lines at 1900 cm^{-1} , 2510 cm^{-1} and for the multilayer at 220 cm^{-1} are visible. The large signal at $\approx 600\text{ cm}^{-1}$ is the fundamental of the surface modes.

The main goal of this measurement was achieved: the vibration peaks of N₂O obtained by HREELS-methods in this study agree with the IRAS spectra which were obtained by Lian et al. It could be shown that annealing the sample to 80 K (i.e. inducing multilayer desorption) does not affect the loss at 2250 cm^{-1} . Thus this loss is, in fact, identical with the $\nu_{3,b}$ vibration, i.e. the asymmetric stretch vibration of N₂O adsorbed on defect sites.

4.2 TPD spectra of N₂O/MgO

N₂O was dosed onto 4 - 30 ML MgO grown on Ag(001) at a base temperature of 20 K. A TPD spectrum (see Fig. 4.4) reveals a multilayer peak at $\approx 80\text{ K}$ and a monolayer peak at $\approx 97\text{ K}$. As the multilayer peak begins to grow before the monolayer peak is saturated, a clear layer by layer growth is excluded. A pure Redhead analysis leads to desorption energies of 21 kJ/mol and 26 kJ/mol for the multi- and the monolayer, respectively.

The monolayer shows unambiguously a first order desorption. The multilayer might either be interpreted as zeroth order or half order desorption, as a comparison with Fig. 1.11 reveals. A half-order desorption of the multilayer would indicate a mixed phase on the surface, which would support the hypothesis of two mono-

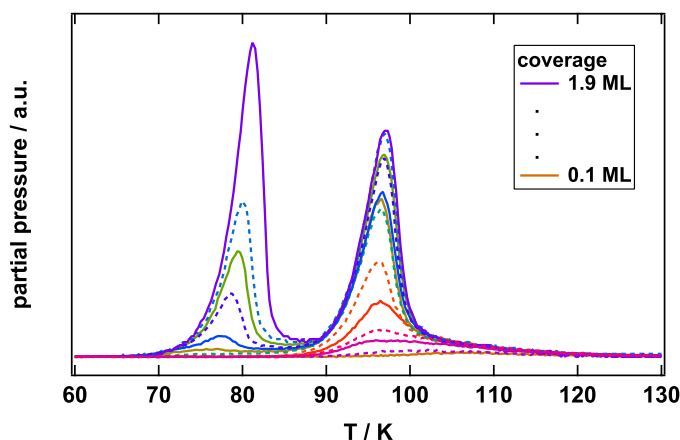


Figure 4.4: TPD spectra with different coverages of N_2O on MgO . A multilayer desorption is at about 80 K and a monolayer desorption peak at 97 K. The simultaneous growth of both peaks contradict a layer by layer growth.

layer phases, where the desorption of the loosely bound one coincides with the multilayer.

An analysis of an inverted Polanyi-Wigner plot, see Fig. 4.5, leads to a more exact and coverage-dependent desorption energy of the monolayer: For coverages larger than 0.3 ML an almost constant desorption energy for the monolayer of 26 kJ/mol is measured. For lower coverages, a dramatic increase of the desorption energy is correlated to the adsorption of N_2O on various defects [103].

As shown in chapter 2.3.2, it is possible to extract the pre exponential factor for different N_2O dosages and thus reveal a coverage dependent pre exponential factor $\nu(\theta)$. The result of this analysis concerning the monolayer is depicted in Fig. 4.6. As shown, the pre exponential factor is for higher coverages $10^{13\pm 1} \text{ s}^{-1}$. However, for coverages lower than 0.6 ML the frequency factor rises abruptly to $10^{16\pm 1} \text{ s}^{-1}$. This again can be correlated to defects as the entropy for low coverages will be higher; the number of different adsorption configurations will be increased by the number of different surface sites.

Summarizing, the recorded TPD spectra reveal the following information:

- There is no pure layer by layer growth.
- The desorption order of the multilayer might be half order which would indicate the presence of mixed phases.
- The monolayer desorbs at 97 K and the multilayer at 80 K. That corresponds

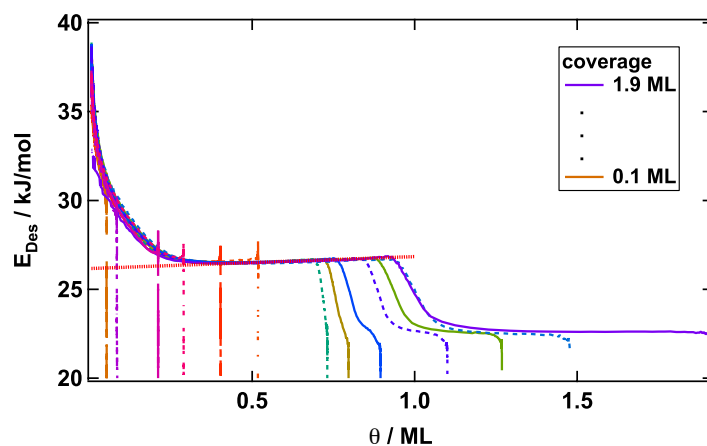


Figure 4.5: Inverted Polanyi-Wigner plot reveals desorption energy of $E_{des} = 26$ kJ/mol with a frequency factor of $\nu = 3 \cdot 10^{13} \text{ s}^{-1}$ for the monolayer. The desorption energy increases for low coverages due to the adsorption on defects.

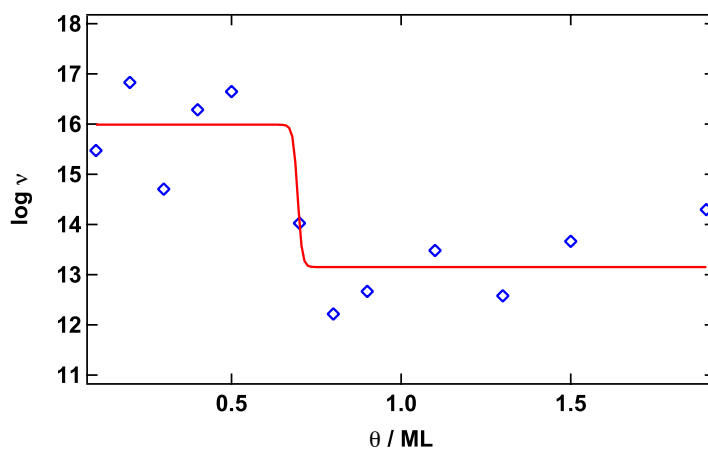


Figure 4.6: N₂O coverage dependence of $\nu(\theta)$ for the monolayer. The monolayer itself has a frequency factor of about $3 \cdot 10^{13} \text{ s}^{-1}$ but rises abruptly for lower coverages ($\nu \approx 10^{16} \text{ s}^{-1}$). This abrupt rise of ν is related to a higher entropy of the system and can be related to an adsorption at defect sites.

Table 4.1: Calculated and measured desorption energies for the monolayer

Adsorption site	E_{des} / kJ/mol	T_{des} / K	Source
terraces	21	80	Ref. [127]
edges	24	91	Ref. [127]
Multilayer	21	80	this thesis, Redhead equation
Monolayer	26	97	this thesis, Fig. 4.5

to a desorption energy of 26 kJ/mol and 21 kJ/mol, respectively.

- The desorption energy increases for lower coverages, indicating desorption from defects
- the frequency factor of the monolayer also increases for lower coverages, corroborating the desorption from defects.

4.3 Conclusion

The number of N_2O molecules associated with the monolayer peak of N_2O in Fig. 4.4 is $\approx \cdot 10^{141}$. Since the number of possible adsorption sites on MgO is $\approx \cdot 10^{15}$, this abundance of N_2O correlated with the monolayer peak is too large to be associated only with adsorption on defects. In that way, the TPD spectra agree with the hypothesis of two adsorption phases. These two phases would also explain the absence of a layer by layer growth and the half-order desorption of the multilayer.

On the other hand, the calculated desorption energy by Xu et al [127] agrees perfectly with the one obtained in this thesis, as table 4.1 shows. The agreement between the adsorption energies would indicate that the monolayer desorbing at 97 K only results from N_2O species adsorbed on edges of MgO . The IRAS-study by Lian et al [83] supports this hypothesis by showing that the IR signals associated with N_2O on terraces already vanish between 80 K and 90 K. HrEELS spectra were able to show that the experimental system investigated in this thesis is comparable to the one researched by Lian et al.

The conclusion is as follows: There exist two monolayer phases, as suggested by Britta Redlich. The low density phase desorbs at 97 K, while a reordering pro-

¹By referring to the ionization probability inside the QMS, the TPD signals can be calibrated to absolute particle numbers.

cess from the high-density phase to the lower one leads to a small desorption at 80 K. This desorption peak coincides with the multilayer which leads to the presence of a mixed phase and thus a half-order desorption. However, the desorption from edges coincides also with the desorption from the lower density phase. The frequency factor (see Fig. 4.6) is increased for coverages up to 0.5 ML. That shows that a decent amount of the monolayer consists of molecules which are not bound regularly, but on defects.

Summarizing, the presented conclusion is a unification of both hypotheses. One method for testing this suggestion concerning the nature of the monolayer is to induce a site-selective chemistry and study the saturation of it. A chemistry initiated at edges would have to saturate with the monolayer if the presented conclusion is valid. As shown in chapter 5.2.2 this is the case.

Chapter 5

Photoinduced N₂O dissociation on MgO films

In most of the measurements presented below, the influence of UV irradiation on one monolayer N₂O was investigated. Post-irradiation TPD spectra for N₂O, N₂ and O₂ are shown in Fig. 5.1. The referred pictures are scaled to magnify the signal of the reaction products; the abundance of generated nitrogen and atomic oxygen, compared to the abundance of N₂O, is only a fraction below ten per cent as Fig 3.7 confirms. UV-irradiation ($h\nu = 5.0 \text{ eV}$, $2 \cdot 10^{18} \text{ photons/cm}^2$) of N₂O adsorbed on MgO leads to a dissociation of N₂O resulting in a depletion of the parent mass, the generation of N₂ desorbing at above 50 K and tightly bound oxygen desorbing at high temperatures above 500 K. The desorption energy of regular molecular oxygen on MgO is about 9.6 kJ/mol [129], thus a low desorption temperature for molecular oxygen is expected. However, the calculated activation energy for recombinative desorption ([129, 130]) of atomic oxygen would fit to the tightly bound oxygen in this experiment. Additionally, the desorption peaks of N₂ and N₂O shift towards higher temperatures, as the TPD spectra show, which is often referred to the presence of atomic oxygen on the surface [131–133]. This shift and the high desorption temperature of oxygen lead to the conclusion that this oxygen desorption peak results from a recombinative desorption of atomic oxygen.

A direct photodissociation of N₂O by interaction with a photon has to be excluded: The absorption cross section of N₂O is $\approx 10^{-24} \text{ cm}^2$, thus after the mentioned photon exposure no dissociation should be present at all.

Even without irradiation, a second N₂ peak (as verified by looking for the a simultaneous QMS signal for $m = 14 \text{ a.m.u.}$) at about 66 K for the TPD spectra is

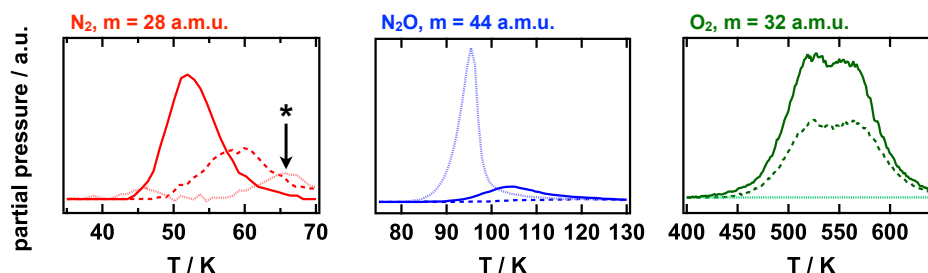


Figure 5.1: TPD spectra prior to irradiation (pale curves), after irradiation with $\approx 2 \cdot 10^{18}$ photons/cm², $h\nu = 5.0$ eV (solid curves) and after prolonged irradiation $\approx 10 \cdot 10^{18}$ photons/cm² (dashed curves). The parent mass N_2O is depicted in blue, the reaction products in red (N_2 , $m = 28$ a.m.u.) and dark green (O_2 resulting from recombinative desorption of atomic oxygen, $m = 32$ a.m.u.). As shown, UV irradiation of 1 ML N_2O leads to a depletion of N_2O and the generation of N_2 and O_2 . This is accompanied by a shift of the low temperature TPD spectra. Prolonged irradiation shows that the generation of N_2 and O_2 peaks and desorption processes occur. A second N_2 desorption peak (marked by an asterisk) only shifts towards higher temperatures but is neither increased nor decreased after UV irradiation.

visible, marked with an asterisk in Fig. 5.1. The height of this peak is not largely affected after irradiation, however, it also shifts towards higher temperatures as the other low temperature desorption features. Whether this second peak results from a photon-independent reaction or is simply N_2 contamination is not clear. This peak does not grow significantly with time, thus a correlation of this nitrogen desorption peak with a contamination from the chamber background is problematic. As illustrated in chapter 5.3.2, an additional deposition of Mg on prepared MgO films results, after annealing, in an enhancement of this desorption peak.

After annealing to 650 K, the initial conditions of the MgO film are restored thus no irreversible (photo)chemically induced changes of the MgO film are detected. To deduce whether the reaction is poisoned by one reaction product, a second experiment was done: The sample was only annealed up to 160 K to record the generated N_2 and remaining N_2O after UV irradiation. The photon dose used was chosen to maximize the reaction yield; so, the N_2O adsorbate on MgO was irradiated with about $2 \cdot 10^{18}$ photons/cm² to obtain the maximal possible reaction yield. If this experimental cycle (N_2O adsorption, UV irradiation, annealing to 160 K and cooling the sample down again to 20 K) is done for several times, a successive decrease of the N_2 peak is recorded (see Fig. 5.2).

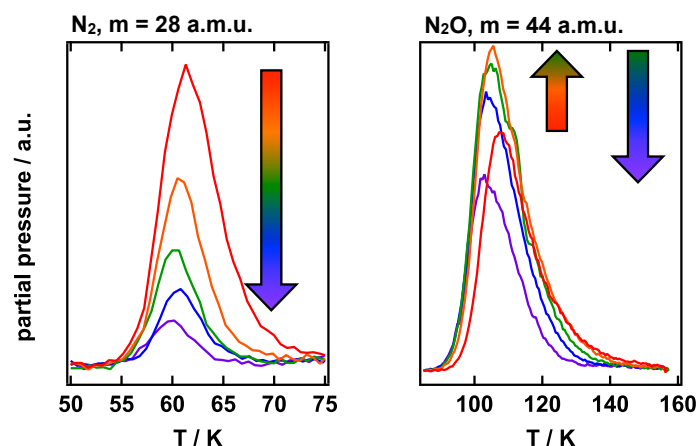


Figure 5.2: TPD spectra of N₂ (left) and N₂O (right) for several cycles of photoexcited reaction on MgO without annealing over 160 K. Without annealing to 650 K between each measurement, 1 ML N₂O was dosed on MgO films and irradiated with $2 \cdot 10^{18}$ photons/cm² before recording the TPD spectra. The arrows indicate the evolution of the peak maxima after each measurement cycle. While the reaction product N₂ drops steadily, the parent mass rises for the first few cycles and then drops also, revealing that two processes are responsible for the decrease of reaction yield.

The mentioned decrease of the reaction product N₂ is for the first couple of cycles accompanied by an increase of the remaining N₂O, but with after some experiment cycles, also the amount of remaining N₂O decreases. Thus it may be concluded that two processes result in a decreasing nitrogen generation. First, the reaction itself gets poisoned, but after 2-4 h measurement time (4 cycles of N₂O adsorption, irradiation, annealing to 160 K and letting the sample cool down) at temperatures below 160 K the adsorption properties of N₂O are altered - supposedly due to a contamination from the gas phase. It is well-known that H₂O desorbs from MgO at temperatures higher than 200 K [134–136], thus, water contamination would alter the adsorption properties of N₂O.

The oxidation of nitrogen to form nitrous oxide is barely possible as the respective reaction constant is $2 \cdot 10^{-37}$, the decreasing amount of generated N₂ with each measurement cycle is explained by a *substrate-mediated* reaction model. The basis of this reaction model is described earlier (chapter 1.2): N₂O dissociates at trapped electrons from a photon-induced electron hole pair excitation and forms nitrogen and atomic oxygen.

Assuming that a contamination with water would result in the altered N₂O

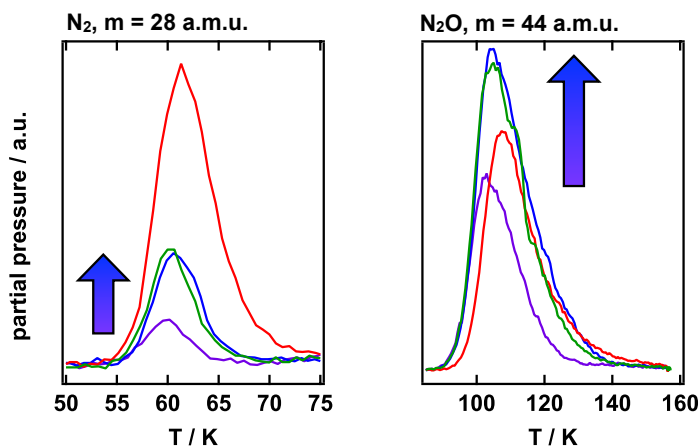


Figure 5.3: TPD spectra of (left) N_2 and N_2O after photoinduced N_2O dissociation on a to 650 K annealed MgO film (red), after two (green) and four (purple) cycles of photoexcitation without annealing over 160 K and after annealing to 300 K (blue). The reactivity is partially recovered, accompanied by a recovery of the N_2O adsorption characteristics.

adsorption properties, a recovery of this process should be detectable after annealing to 300 K, a temperature high enough to initiate water desorption. In fact, this hypothesis is proven true: As Fig. 5.3 shows, the amount of N_2O remaining after irradiation has recovered to its maximal amount. At this point, a feasible conclusion might be as follows:

- Photons initiate a substrate-mediated process which triggers the reaction.
- The number of possible reaction sites is finite (as the passivation of the reaction confirms).

The nature of the reaction mechanism will be examined thoroughly in the next sections. To conclude these preliminary discussions, a suggestion about the adsorption site of the photogenerated N_2 is presented. In Fig. 5.4 the TPD spectra of the photoproduct N_2 after N_2O dissociation and of regular N_2 adsorbed on pristine MgO films are plotted, the latter one with different coverages so that the monolayer generation can be studied. Since the amount of generated nitrogen is very small, a logarithmic scale was chosen to magnify the data. The photogenerated N_2 is differently adsorbed than regularly adsorbed nitrogen on defects and thus the question is, how and where this photoproduct is adsorbed. The shift of the low TPD spectra is, as already mentioned, associated with the abundance of atomic oxygen on

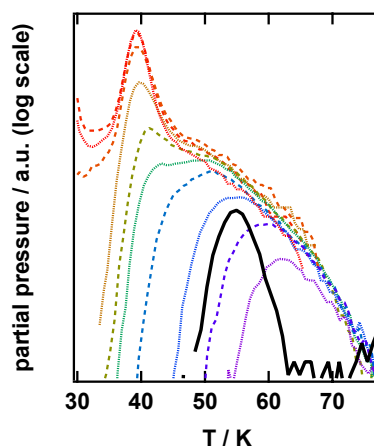


Figure 5.4: A comparison between adsorbed N_2 (color lines) on MgO and the photoproduct after UV-induced N_2O dissociation (thick black line) shows that the generated site is different from regular, defect bound N_2 on MgO surfaces.

the surface. One possible interpretation would then be that after dissociation, the generated nitrogen is primarily bound by atomic oxygen.

5.1 Photon dose dependence

A first look on the photon dependence of photoinduced N_2O dissociation on MgO surfaces reveals that N_2 and atomic oxygen are formed (the latter desorbs recombinatively as molecular oxygen), see Fig. 5.1. The reaction takes place at a limited number of surface sites, as the possibility to poison the reaction shows. A fingerprint of atomic oxygen is found in the shifting behavior of the low temperature TPD spectra and the tightly bound oxygen desorbing recombinatively above 500 K.

In this part, the aim is to examine the photon dependence thoroughly and in the end be able to deduce a feasible reaction model based on a substrate mediated reaction mechanism (see chapter 1.2). To verify that, raw TPD spectra of N_2 , N_2O and O_2 were recorded after irradiation of 1 ML N_2O adsorbed on 20 ML MgO for different photon exposures, see Fig 5.5. As shown in this picture, the generation of N_2 and O_2 saturates after irradiation with $\approx 2 \cdot 10^{18}$ photons/cm². At higher photon exposures, photon induced desorption processes dominate.

The TPD spectra were calibrated with respect to each ionization probability inside the quadrupole mass spectrometer so that the amount of respective particles could be estimated. A photoinduced electron excitation process in the MgO

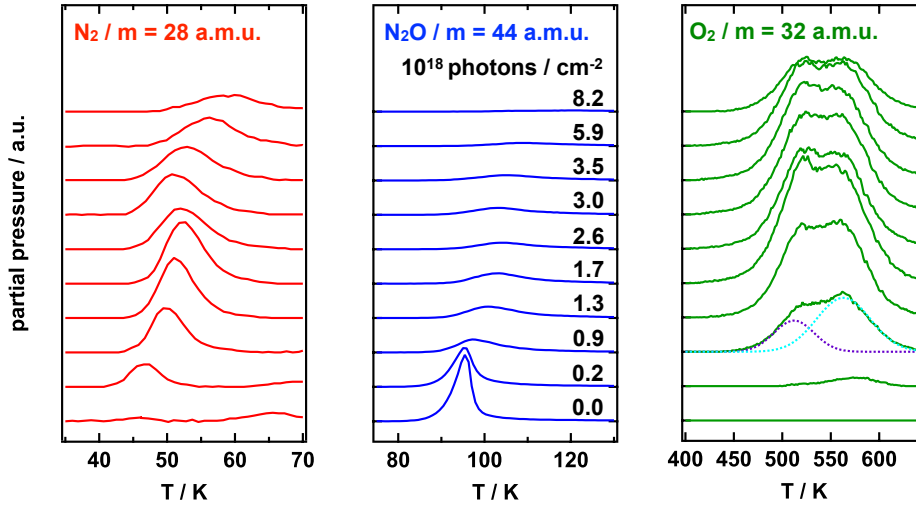
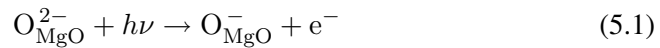


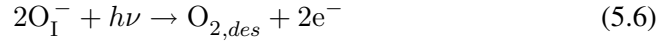
Figure 5.5: A more thorough view of the process presented in Fig. 5.1. The color code is the same as described there. As shown, the the nitrogen and oxygen generation saturates after $\approx 2 \cdot 10^{18}$ photons/cm² and photon induced desorption processes begin to dominate for both photoproducts and the educt. The purple and cyan lines show that the oxygen desorption consists of two desorption peaks at 520 K and 570 K suggesting two reaction mechanisms.

film is thought to be the underlying mechanism (see chapter 1.2). Whether a reaction model based on an electron-hole pair excitation would be able to describe the recorded data was examined by modeling the photon-dependent generation and desorption with the reaction pathways eq. 1.1 and eq 1.2 plus one electron-induced N₂O dissociation:



Here, $\text{O}_{\text{MgO}}^{2-}$ is a regular oxygen ion from the MgO film, O_I^- a generated, adsorbed oxygen atom with one negative charge¹ and *tr* denotes an electron trap like a (di)vacancy, a reverse corner or more extended defects (thus e^-_{tr} denotes a trapped electron). Corresponding reaction pathways for photon-induced desorption were also included:

¹It is important here to stress again that the single charge of the atomic oxygen is, in respect to the regular, two times charged oxygen of the MgO lattice, technically a *hole*.

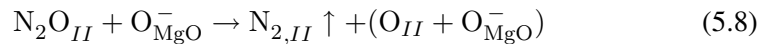


Since the direct photoproduct - the excited electron-hole-pair electron - is not detectable by TPD, a quasi steady state approximation was applied in order to model the reaction. In that sense, a fixed number of reaction sites was assumed which react in the presence of light or more specifically said, eqs. 5.1 - 5.3 were summarized to:



A set of differential equations corresponding to eqs. 5.4 - 5.7 was solved. The fitting parameters were the respective dissociation and desorption cross sections and the amount of reaction sites, educts and products. The implementation was realized with Wolfram Mathematica. The best fitting solution is shown as dotted curves in Fig. 5.6.

Even though this model is in almost perfect agreement with the detected nitrogen generation, the description of oxygen generation is incomplete: The maximal amount of generated oxygen is underestimated. As already mentioned, the oxygen desorption consists of two desorption peaks. Moreover, a second reaction pathway on MgO is assumed in literature where N_2O dissociates at O_{MgO}^- forming nitrogen and oxygen [50, 137–140]. A similar mechanism is assumed to take place on the MgO surface after irradiation:



The roman literals (*II*) indicate the educts and products of this second reaction mechanism. If this second reaction pathway, in the form of a quasi steady state approximation analogous to eq. 5.7, and a high nitrogen desorption cross section for the nitrogen generated by dissociation of N_2O on O_{MgO}^- sites is assumed (and respective desorption pathways for nitrous oxide and oxygen), the agreement between experimentally derived and assumed data by the reaction model is dramatically enhanced.

A confirmation of this model is that the two oxygen peaks forming the overall oxygen desorption agree not only qualitatively, but also *quantitatively* with the reaction model: As in Fig. 5.6 the agreement between purple and cyan squares

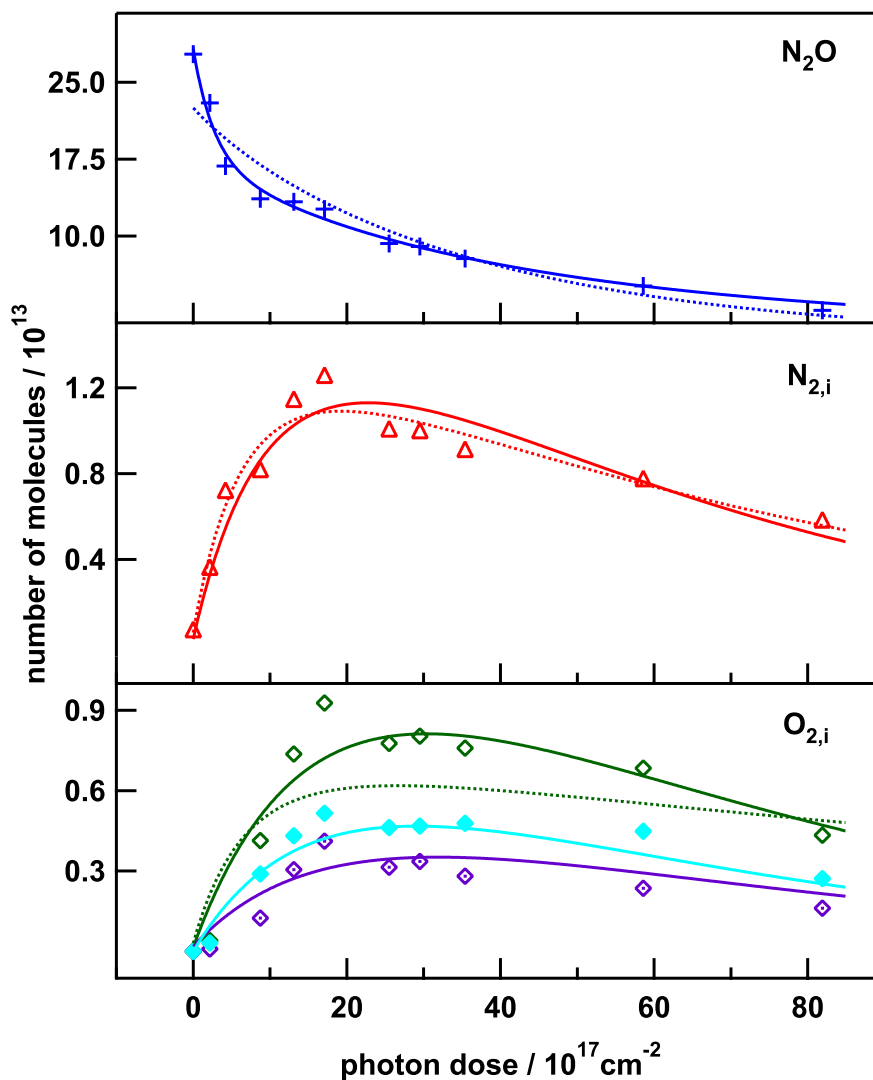


Figure 5.6: Photon dependencies of the educts' (N_2O) and the two reaction products' respective quantities as derived from the raw data shown in Fig. 5.5. The subscript i denote that these compounds are generated by irradiation. The markers show the experimental data and the lines the dependencies obtained by fitting the data to a reaction model. The dashed lines are based on the simple reaction mechanism with one one and the solid ones the more complicated reaction mechanism on two N_2O dissociation pathways. The cyan and purple symbols are the oxygen quantities associated to the two oxygen subpeaks while the respective lines are the expected behavior after the fitting process.

and the respective lines shows, the expected behavior of the two reaction products agrees almost perfectly to the experimental result. It has to be stressed here that these two oxygen subspecies served as a way to confirm the model *after* the fitting process, thus only the overall oxygen desorption was put into the model.

Moreover, the two oxygen desorption peaks can unambiguously be referred to the respective reaction pathways: The peak at 520 K results from atomic oxygen generated at electron traps (by reaction path 5.3) while the oxygen desorption peak at 570 K results from N₂O dissociation at localized holes (reaction path 5.8).

The maximal amount of generated atomic oxygen is, as shown in Fig. 5.6, about $2 \cdot 10^{13}$ (the desorbing molecular oxygen scaled by two). This high abundance exceeds the expected number of uncharged oxygen vacancies by at least two orders of magnitude [39, 40], see chapter 1.1.2. The electron trapping has to have another nature. As regular steps, edges and corners but also more extended, so-called shallow electron traps as divacancies or reverse corners possess the property to capture electrons these sites or some of them might play a role in this process. This topic will be examined by discussing EPR data (see chapter 5.4).

The respective cross sections for the first (eq. 5.3) and second (eq. 5.8) reaction pathway are $5 \cdot 10^{-19} \text{ cm}^2$ and $2 \cdot 10^{-19} \text{ cm}^2$, respectively.

As TPD is only a post mortem method an analysis of the *desorbing* species only based on the remaining compounds on the surface is, due to the presence of two reaction pathways, not possible. Only assumptions based on literature and comparison of the remaining compounds on the surface could be done. A local heating process (as detected for TiO₂ crystals [141]) cannot be assumed as the desorption cross sections are not correlated to the desorption energy of the respective compound. Furthermore, the respective absorption cross sections of the adsorbed molecules (or oxygen atoms, respectively) are far too low to explain the desorption process by direct photoexcitation. Thus one conclusion might be a coupled hot electron mechanism where excited, not trapped electrons lead to an energy transfer to the adsorbate. As the aim of this thesis was the investigation of the reaction, a further analysis of the desorption cross sections is not presented.

5.2 Photon energy dependence

Beside the excitation with 5.0 eV, N₂O dissociation was initiated with other photon energies as well. As described in chapter 1.1.1, the band gap of MgO varies with the local topology, thus a site - dependent electron hole pair excitation is possible

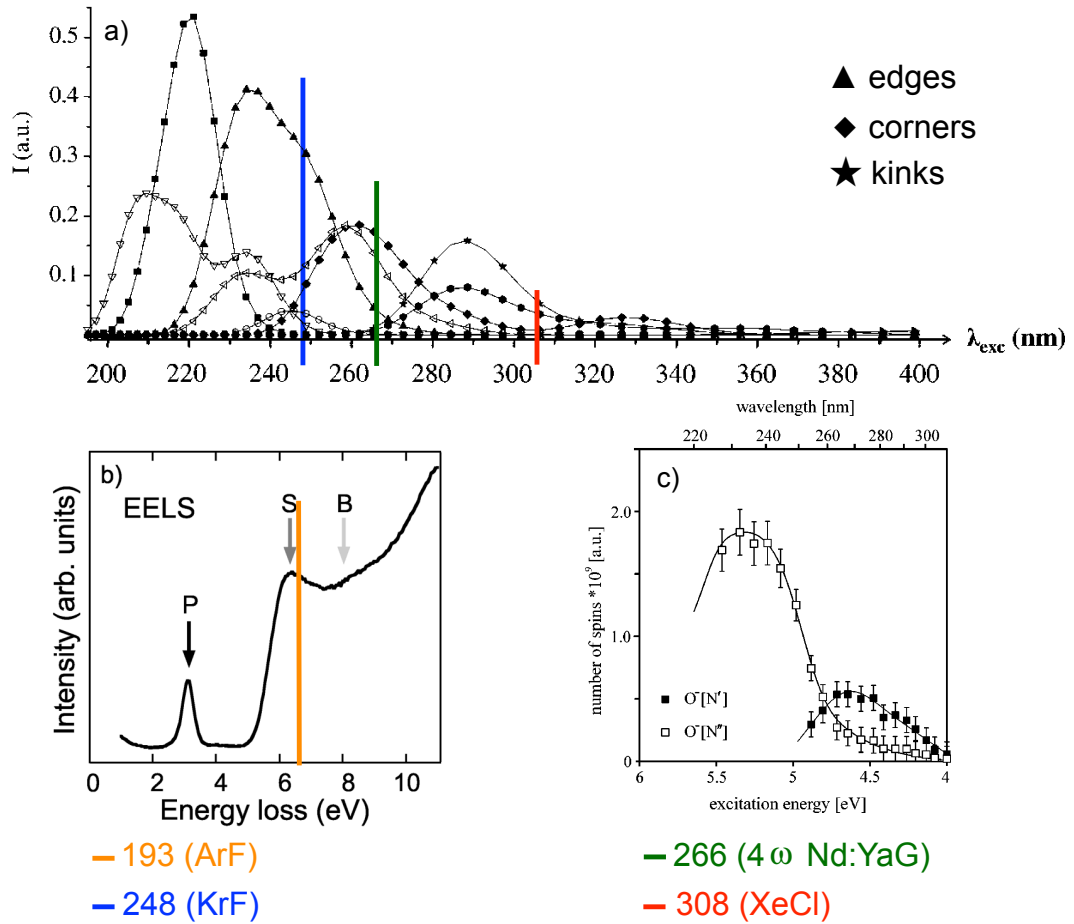


Figure 5.7: a.) excitation spectra of MgO derived from theoretical band structure calculations. The figure is taken from Ref. [142]. The colored lines are the excitation wavelengths used in the experiment. Triangles show the relative absorption cross section for edges, rhombusses for corners and stars for kinks b.) EELS spectrum of MgO. The surface band gap of ≈ 6 eV is clearly visible (depicted with an "S"). The picture is taken from Ref. [37] c.) as comparison to the calculated excitation spectrum in panel a.), the number of free spins derived from EPR spectra is in qualitative agreement with with the calculated spectrum a.). The picture is taken from Ref. [22].

by generating electron hole pairs with different photon energies. The measurements done before this thesis and described in chapter 1.2 were mainly done on MgO powders and at higher pressures. The transfer into UHV - conditions would make it possible to quantify the reaction cross sections (as already shown in the last chapter for 5.0 eV irradiation) and its saturation conditions with respect to the initial N₂O coverage. Especially the chemistry of electron-hole-pairs excited at terraces was not yet exclusively investigated. So one additional goal in this study was to elucidate whether the chemistry initiated at terraces is similar to the one at lower coordinated sites. This was realized by applying 6.4 eV photon irradiation which suffices to excite electrons from the valence to the conduction band at terraces, see Fig. 5.7 b.).

In this experiment, four different wavelengths were used (as described earlier, see table 2.1). While the 5.0 eV light is capable of overcoming the band gap at edge sites, it should be possible to initiate an electron-hole-pair excitation at lower coordinated sites with lower photon energies while higher coordinated sites would need higher ones.

The photoexcited excitons are capable to transfer to sites with equal or lower coordination until they recombine or the excited electron is trapped. As shown in Fig 5.7, it is possible to excite different surface sites with different wavelengths. The wavelength of the used light sources is included in this figure as straight lines with different color: The 6.4 eV photons generated by an ArF laser would be high enough to overcome the band gap at terrace sites (as shown in the EELS spectrum, panel b.)), while the 4.6 eV of the 4th harmonic of a Nd:YAG laser and the 4.0 eV emitted by a XeCl would excite electron hole pairs at corners and kinks, respectively, see panel a.) in Fig. 5.7. Since all of the processes are electron-driven and thus only indirectly dependent of the photon energy, the cross sections should be the same for all used wavelengths. However, the reaction yield should vary with the *number* of expected defect sites. Thus, the maximal reaction yield is expected to be dependent on the initial N₂O coverage and the used photon energy. Fig. 5.8 shows the maximal reaction yield after irradiating one monolayer of N₂O: the respective amounts of both reaction products grow with the used photon energy and thus with the coordination of the excited surface site. It should be noted that the number of photons used differs significantly for 6.4 eV: While the number of photons needed to saturate the reaction is almost identical for the three lower photon energies ($\approx 10^{18}$ photons/cm²), a significantly lower photon dose ($\approx 10^{16}$ photons/cm²) was needed to saturate the reaction here.

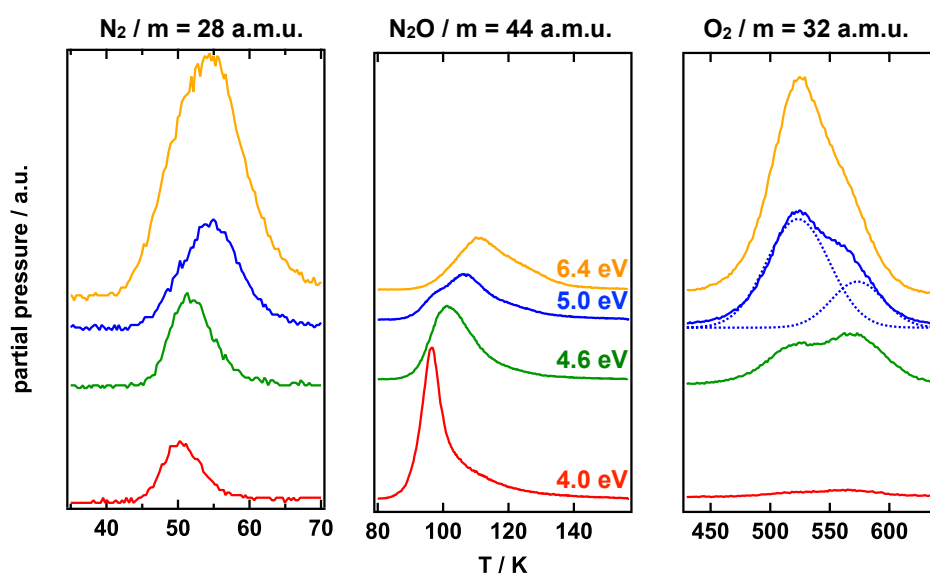


Figure 5.8: Raw TPD spectra after irradiation with photons whose photon energy is 6.4 eV (orange), 5.0 eV (blue), 4.6 eV (green) and 4.0 eV (red). The amount of generated N_2 and O_2 as well as the N_2O depletion is proportional to the photon energy (and thus to the coordination of the excited surface site), however, the photon doses needed to saturate the reaction yield differ significantly. Moreover, a shift of the N_2 and N_2O TPD spectra towards higher temperatures again indicates the presence of atomic oxygen on the surface.

Table 5.1: number of electron traps and reaction cross sections for N₂O dissociation

$\lambda (h\nu) / \text{nm (eV)}$	excited site	$tr / 10^{14}$	$\sigma_{e_{tr}^-} / 10^{-17} \text{ cm}^2$	$\sigma_{O^-} / 10^{-17} \text{ cm}^2$
193 (6.4)	terrace	0.38	3.00	1.62
248 (5.0)	edge	0.29	0.05	0.02
266 (4.6)	corner	0.05	0.07	0.09
308 (4.0)	kink	0.04	0.05	0.01

5.2.1 photon doses

Analogous to the measurement series shown in Fig 5.5, 1 ML N₂O adsorbed on MgO was irradiated with 6.4 eV, 4.6 eV and 4.0 eV for different photon exposures. The absolute amounts of N₂, N₂O and atomic oxygen were again derived from TPD spectra so that the reaction yields and cross sections could be quantified analogous to Fig. 5.6; the reaction mechanism described in chapter 5.1 was fitted to the respective amounts. The result of these fits for the different used photon energies is shown in Fig. 5.9.

The photon-dependent behavior fits well the expected one. Generally, a lower photon energy excites lower coordinated sites and thus results in a lower reaction yield. For the lower three wavelengths, the reaction cross sections are almost identical suggesting a similar reaction mechanism. The numbers of electron traps and the cross sections for both photon dissociation pathways derived from fitting the data to the reaction model are depicted in table 5.1.

According to the used reaction model, the number of electron traps which contribute to N₂O dissociation rises with the used photon energy. That is not surprising as higher photon energies excite electron-hole pairs at sites with a higher coordination; for example, photons with an energy of 6.4 eV will also excite electron hole pairs at terraces which can then also be trapped at sites with a higher coordination than edges.

Since the number of excited electron hole pairs is significantly higher when 6.4 eV photons are used, the probability of obtaining a trapped electron and thus the overall reaction cross section is dramatically enhanced which explains the large reaction cross sections for reactions initiated with 6.4 eV.

To conclude, a fluence-dependent investigation of the photochemistry initiated with different photon energies confirms the hypothesis of a site-selective reac-

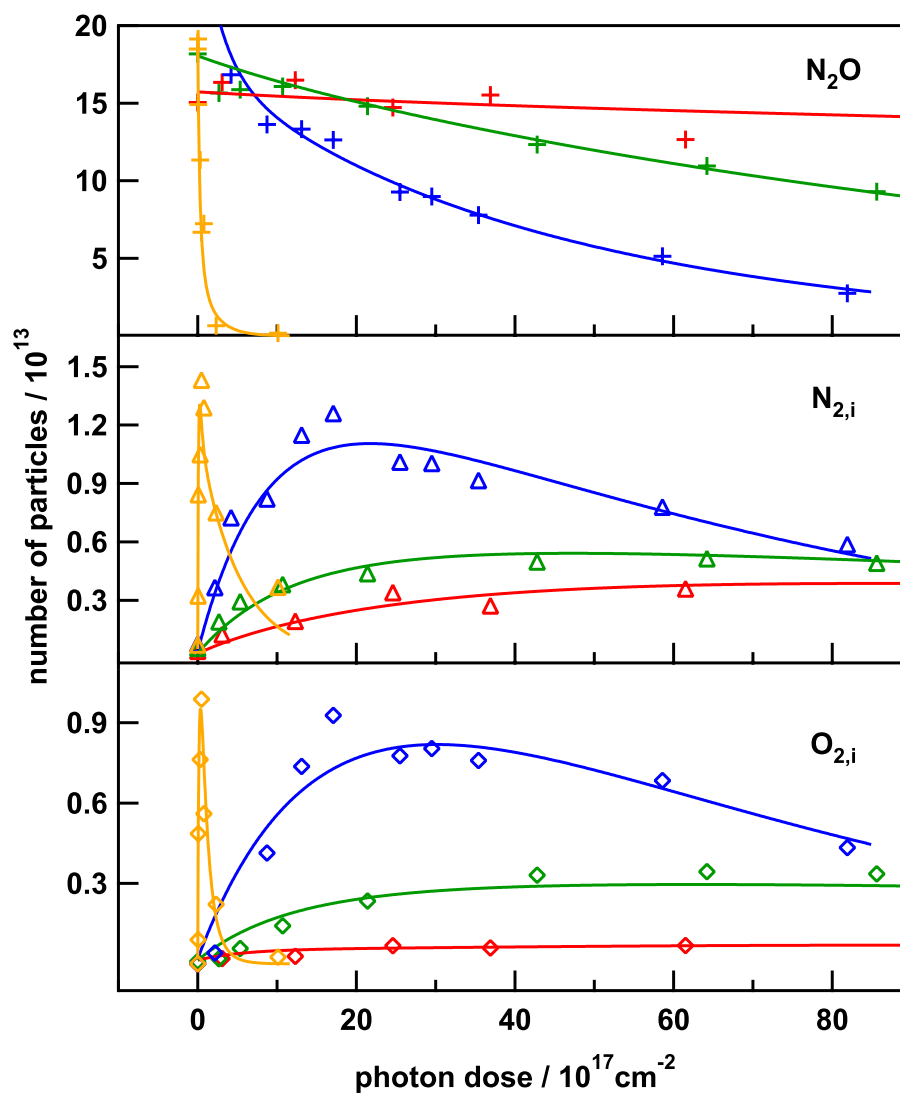


Figure 5.9: Photon dose dependencies of N_2O and the dissociation products with respect to the used photon energy: orange symbols and lines describe the photon dependence initiated with 6.4 eV photon energy, blue the one with 5.0 eV, green the one with 4.6 eV and red finally the photon dependence with 4.0 eV. Again, the markers show the experimental data and the lines the dependencies obtained by fitting the data to the reaction model eqs. 5.4-5.8.

tion. This reaction is controllable with different photon energies: The excitation of electron-hole pairs at surface sites with a higher coordination leads to a higher reaction yield and vice-versa. Moreover, the significantly larger abundance of electron-hole pairs excited at terraces (when using 6.4 eV photons) makes the electron trapping process (and thus the reaction) more probable and thus accelerates the reaction.

This site-selectivity will be confirmed in the next paragraph when the initial N_2O coverage dependence is discussed and a final conclusion about the nature of the N_2O monolayer is drawn.

5.2.2 N_2O coverage dependence

Since sites with a larger binding energy are assumed to be covered by adsorbate molecules earlier, reactions at corners would be expected to saturate at lower coverages than reactions at terrace sites. Thus, different amounts of N_2O were dosed on the MgO film and were irradiated long enough to saturate the reaction - about $2 \cdot 10^{18}$ photons/cm² for the lower three photon energies and 10^{16} photons/cm² for the reaction initiated with 6.4 eV. The absolute quantities of the reaction products were then examined in dependence of the initial N_2O coverage.

It was discussed in chapter 5.1 that due to the different desorption cross sections, nitrogen is no sufficient monitor to describe the whole reaction: the N_2O dissociation consists of two reaction pathways. As Fig. 5.10 shows, the reaction yields for N_2 and O_2 show different saturation behavior. This is consistent with the higher desorption cross section of N_2 for the second reaction pathway, as shown in the chapter 5.1. Since the generated oxygen is a more suitable reaction monitor than nitrogen, the focus is now on the investigation of the generated oxygen.

In Fig. 5.11 the N_2O coverage dependencies for oxygen generation with photon energies of 4.6 eV, 5.0 eV and 6.4 eV are shown. The excitation with 4.6 eV photons saturates the reaction already at an initial N_2O coverage of ≈ 0.6 ML, the one with 5.0 eV at 1.0 ML and the one initiated with 6.4 eV at coverages larger than 1.5 ML. Unfortunately, as the oxygen generation initiated by 4.0 eV irradiation is very low (see Figs. 5.8 and 5.9), measurements dependent on the initial N_2O coverage were not possible.

The adsorption energy scales with the coordination of the respective surface site, thus it can be assumed that during N_2O adsorption lower coordinated sites are earlier occupied than higher coordinated ones i.e. that the *saturation* of lower coordinated sites precedes the one of higher coordinated sites. Thus, a reaction

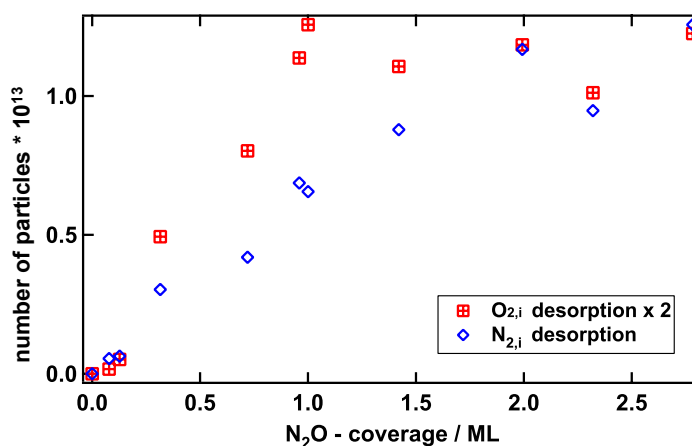


Figure 5.10: Coverage dependence of both reaction products at initiation with 5.0 eV. The red boxes indicate the amount of generated atomic oxygen (hence the number of oxygen molecules times 2), the blue squares the one for nitrogen. While the oxygen saturates rather abruptly at an initial coverage of one monolayer N_2O , the nitrogen yield continues to grow up until 2 ML.

initiated at corner sites should saturate at lower initial N_2O coverages than the reaction initiated at edge sites, followed by a reaction initiated at terrace sites. The saturation of the reaction with respect to the used photon energy and the initial N_2O coverage shows a confirming behavior: As Fig. 5.11 shows, irradiation of MgO 4.6 eV excites electron-hole pairs at corners, with 5.0 eV at edges and 6.4 eV at terraces. As predicted, the saturation of the reaction scales with the coordination of the excited surface site.

Here is a good point to remind the questions regarding the nature of the N_2O monolayer discussed in chapter 4: While IRAS measurements and DFT calculations suggest to correlate the monolayer species desorbing at 97 K to N_2O adsorbed on edges, the huge TPD signal, FTIR measurements and Monte-Carlo simulations propose a second monolayer phase which is not as tightly packed. In the mentioned chapter, the drawn conclusion was that the monolayer peak of N_2O results from a desorption of a low density adsorption phase on terraces as well as from a desorption from edges. In the presented studies irradiation of N_2O adsorbed on MgO with $h\nu = 5.0$ eV, i.e. excitation of electron hole pairs at the edges of MgO leads to a reaction whose saturation coincides with the saturation of the N_2O monolayer species, while the excitation of electron hole pairs at terraces (i.e. photoexcitation with 6.4 eV) saturates at higher coverages. This behavior clearly supports the conclusion about the nature of N_2O adsorption on MgO: As an additional, high density

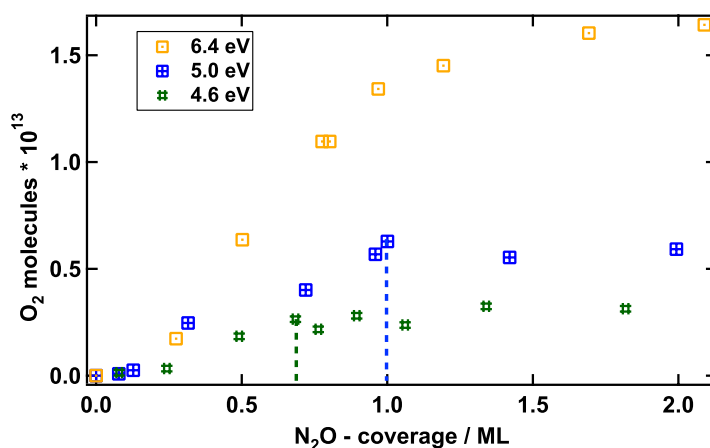


Figure 5.11: N₂O coverage dependence of oxygen generation with different photon energies (4.6 eV green, 5.0 eV blue and 6.4 eV orange). An earlier saturation of oxygen generation is seen for lower photon energies proving a site dependent excitation mechanism.

monolayer phase exists at terraces whose binding energy is almost identical to the one of the multilayer, it is expected that the reaction initiated at terraces saturates at higher initial N₂O coverages than the reaction initiated at edges. Moreover, as shown in Figs. 5.8 and 5.11, the reaction yield at only one monolayer N₂O is significantly larger for 6.4 eV than for 5.0 eV. That confirms that more reaction sites than edge sites should be correlated with that monolayer coverage of N₂O.

It is shown that the photoinduced reaction saturates with respect to the initial N₂O coverage as predicted: A reaction initiated at corners should saturate earlier than at edges while the reaction initiated at terraces should saturate at higher coverages. Moreover, as the irradiation of one monolayer N₂O with 6.4 eV photons leads to a higher reaction yield than the use of 5.0 eV and since the reaction initiated with 6.4 eV saturates at N₂O coverages larger than one monolayer, the characteristics of N₂O adsorption on MgO as suggested in chapter 4 were proven valid.

5.3 MgO preparation dependence

Since the photochemistry is expected to be defect-mediated, reaction probabilities should be altered by varying the MgO film preparation. In this thesis, this was tested for three model systems. The first model system makes use of the thickness-dependent surface quality of MgO. Very thin films are discussed briefly concerning

the possible influences from the metal substrate already mentioned in chapter 1.1.3.

The second model system are MgO films with small amounts of magnesium added onto the surface with the purpose to increase the number of electron traps artificially. These measurements are compared to a similar experiment investigated with EPR done by Gonchar et al [143].

The third model system was a MgO film obtained by post oxidation of pre-adsorbed magnesium. This preparation technique leads to domains rotated by $n \cdot 60^\circ$ to each other. Whether this forced breaking of a simple layer by layer growth is a useful way to increase the number of reaction sites and whether this is a suitable model system is discussed².

5.3.1 Influence of film thickness

The most simple and stable change in surface quality is to vary the film thickness. As already described in chapter 3.1.2, LEED-pictures of MgO films with different thicknesses grown on $Ag(001)$ suggest that the roughness of the surface increases with film thickness. Since a corresponding trend for divacancies, other electron traps and low coordinated sites can be assumed, a proportionality between film thickness and reaction yield seems reasonable.

A first look upon the photon dependent generation of N_2 by dissociation of 1 ML N_2O adsorbed on different MgO preparations ($h\nu = 5.0$ eV) seems to contradict this idea (see Fig. 5.12): No distinct film thickness dependence is seen for the N_2 generation yield. However, the broad distribution of generated N_2 molecules (between $0.75 \cdot 10^{13}$ and $1.3 \cdot 10^{13}$) shows that the amount of generated N_2 for a fixed photon dose is already dependent on MgO preparation: While on a prepared MgO film photon dependent processes are reversible after annealing to 650 K, Fig. 5.12 shows that the amount of generated nitrogen varies with each MgO preparation.

As already discussed, N_2 is not a good monitor for the reaction processes in general; the atomic oxygen generation could only be quantified by assuming a second reaction pathway (see chapter 5.1) as also the dependence of the reaction yield with respect to the initial N_2O coverage has shown (as described in chapter 5.2.2). Thus it seems reasonable to look upon the maximal reaction yield of oxygen generation in dependence of the initial MgO film thickness.

²A fourth possibility is to prepare the films at lower temperatures. For the *initial* reaction yield a gain of the reaction yield is visible but this gain is very small. Moreover, since the crystal has to be heated up to 650 K after each measurement, the film quality is enhanced with each annealing cycle leading to a relaxation of the reaction yield comparable to regularly prepared films.

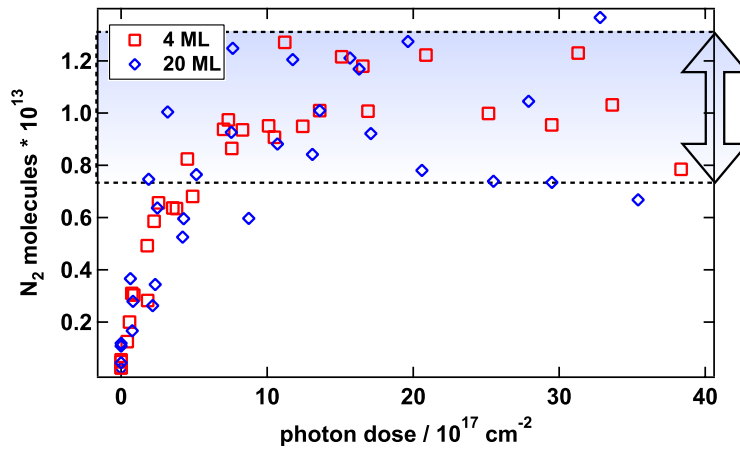


Figure 5.12: Photon dependence of N_2 generation for UV induced dissociation of 1 ML N_2O adsorbed on different MgO films with 4 ML and 20 ML thickness. No direct correlation between reaction yield and thickness is detected. The reaction yields for different preparations range between $0.75 \cdot 10^{13}$ and $1.3 \cdot 10^{13}$ N_2 molecules as indicated by the arrow on the right side. The reaction yield and cross section concerning the N_2 generation is the same for thin and thick films.

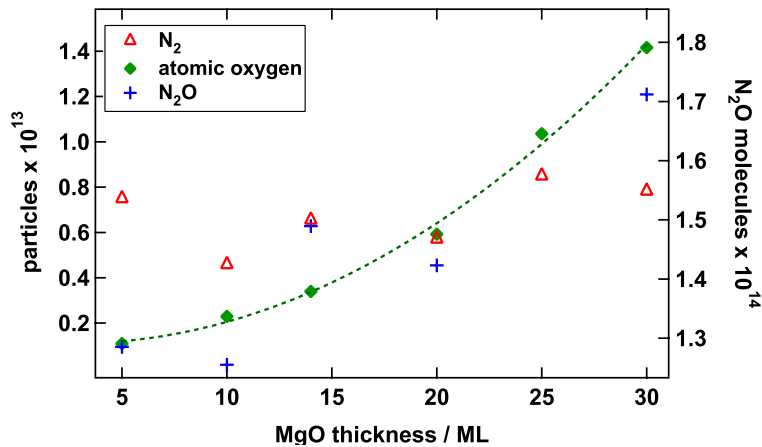


Figure 5.13: Maximal atomic oxygen generation yield after irradiation ($h\nu = 5.0$ eV) of 1 ML N_2O adsorbed on MgO films with different thicknesses ranging from 5 ML to 30 ML. The expected thickness dependence of the reaction is confirmed by investigating the atomic oxygen generation which grows quadratically with thickness. The nitrogen generation is constant. Note that the initial N_2O coverage grows similarly revealing a correlation between the adsorption and the reaction sites.

A following set of measurements was the irradiation of one monolayer N_2O with $2 \cdot 10^{18}$ photons/cm² adsorbed on MgO films with thicknesses ranging from five to thirty monolayers. TPD spectra of N_2 , N_2O and O_2 were converted to absolute particle numbers. The result is shown in Fig. 5.13.

The aforementioned prediction has proven valid: the atomic oxygen yield grows with film thickness while the nitrogen generation, as a not completely suitable reaction monitor, stays almost constant. It is interesting to note that the initial N_2O coverage (which is the number of N_2O molecules forming the monolayer structure at $T = 97$ K) grows in a similar manner as the oxygen yield. The interpretation is, referring to the combined nature of the N_2O monolayer peak, straightforward: As LEED pictures suggest (see Fig. 3.2), MgO surfaces become rougher and defective with increasing film thickness. This picture is confirmed by the increasing number of N_2O molecules forming the monolayer which consists partially of N_2O molecules adsorbed on edges. Since the reaction is initiated at edges - and a higher roughness of the MgO film will lead to more electron trapping sites - it is obvious that the reaction yield will grow. The high reaction yield is the reason why most of the presented measurements in this study are done on thick (20-30 ML) MgO films.

The increasing reaction yield with film thickness confirms that any contribution of the bulk for the regular high-temperature atomic oxygen feature has to be excluded: Even if silver diffuses into the MgO film as suggested earlier, the amount of (sub)surface MgO will decrease with film thickness (see Fig. 3.1). For thin films, however, this silver contribution might influence the reaction as discussed in the following section.

Low temperature oxygen desorption for thin MgO films

In chapter 1.1.3 the electrical and chemical properties of very thin MgO films on metal were briefly discussed. Fig. 5.14 shows that very thin films (4 - 5 ML MgO) exhibit after N_2O dissociation different oxygen desorption characteristics: Two additional desorption peaks arise at $T_1=300$ K and $T_2=330$ K. Since the desorption spectrum is much more complex consisting of four peaks, the focus of this thesis was on thicker films when determining the reaction cross sections. Here, the aim is on discussing different mechanisms which might be the underlying reason for reactions only occurring at thin films. These mechanisms are illustrated in the scheme of Fig. 5.15.

- Gonchar et al. [71] have investigated a similar system by studying the O_2^-

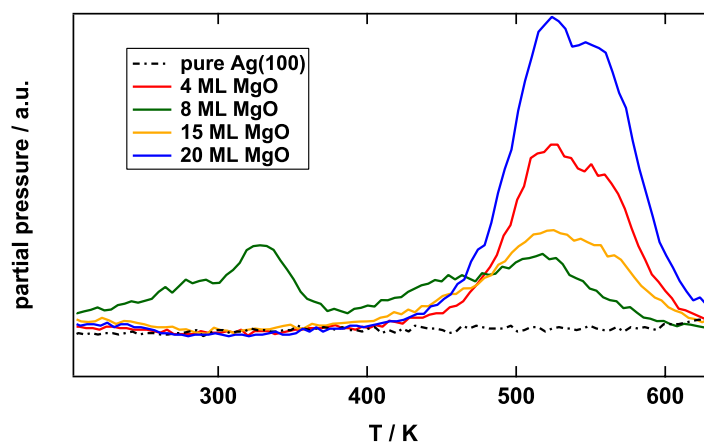


Figure 5.14: Raw TPD spectra of pre-generated atomic oxygen ($m = 32$ a.m.u.) desorbing from MgO for different MgO film thicknesses (4-20 ML). The thinnest MgO film shows a distinct second peak structure at low temperatures (250-350 K). A simple interpretation of a reaction on silver can be excluded; a bare silver crystal shows no oxygen generation at all.

radical formation on thin MgO films after exposure to an oxygen ambient. The underlying reason for this radical formation was thought to be a polaronic distortion. In their study, two EPR lines are detected ($g = 2.037$ and 2.013) which vanish at 350 K and 650 K, respectively, which would be quite consistent to the measurements presented here. However, the EPR signal studied in Ref. [71] decays exponentially with film thickness in contrast to the abrupt vanishing of these low temperature desorption peaks for MgO film thicknesses larger than 4 ML.

- A reaction on remaining spots of pure silver can be excluded. As the dot-dashed line indicates, no oxygen desorption in the temperature range is detected for irradiation of N_2O on Ag(001). This is reasonable since the N_2O monolayer desorbs from silver at ≈ 85 K (see Fig. 5.16).
- Another possible explanation might be a reaction initiated by a photoinduced charge transfer from the metal bulk to the oxide surface. The MgO film is at terrace sites transparent to 5.0 eV light thus an excitation of the silver's electron bath is possible. A charge transfer to the surface is restricted to thin films, since the mean free path of the excited electron is finite.
- A fourth way would be to assume more complicated interface structures

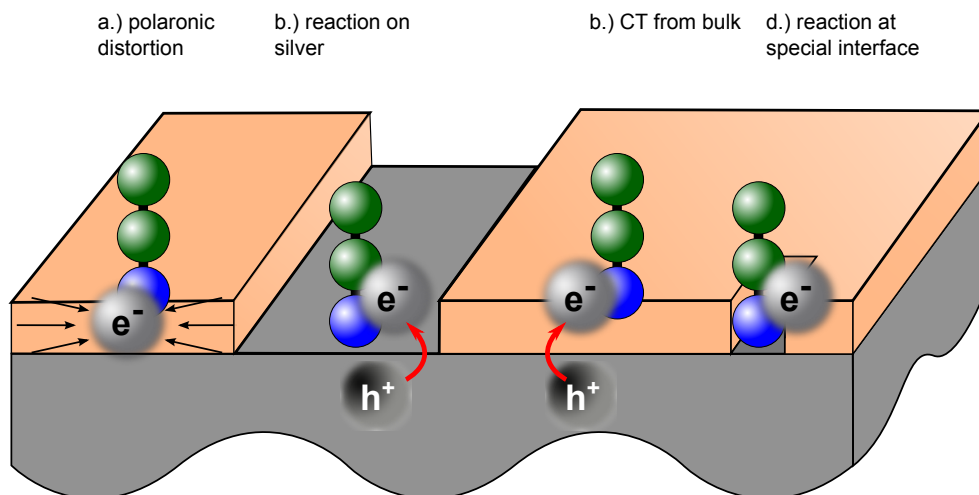


Figure 5.15: Possible reasons for the reaction at thin films are described. a.) Polaronic distortion, b.) N_2O dissociation at pure silver c.) a charge transfer from the silver bulk d.) electron trapping at distinct metal-oxide interfaces.

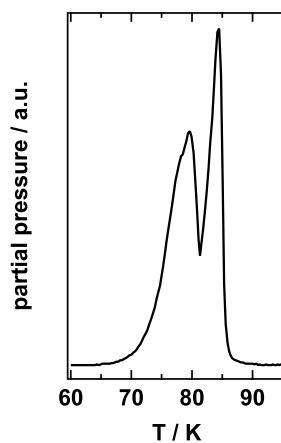


Figure 5.16: Raw TPD spectrum of N_2O adsorbed on pure $Ag(001)$. The monolayer species desorb at about 80 K revealing that after annealing to 85 K no N_2O is adsorbed on pure silver anymore.

which would appear on partially covered silver crystals: An interface site which is surrounded partially by MgO and partially by silver. These sites are expected to possess a significantly different electronic structure which may result in the detected behavior. Moreover, since a complete coverage of the surface will extinguish these sites, a rapid decrease would be reasonable. However, as no information about the electronic structure of these sites is available, this is only a possibility which needs to be discussed with other methods.

To conclude, two possibilities for this kind of reaction seem reasonable: on the one hand, charge transfers from the silver substrate to the MgO surface, which are possible for thin films, might be the underlying reason a distinct chemistry on thin MgO films. On the other hand, special interface sites surrounded partially by silver and partially by MgO may act as a distinct kind of electron traps. To verify one of these possibilities it would be mandatory to examine the thin film behavior more thoroughly. However, since the investigation of chemistry on MgO films as a model system for the photochemistry on regular oxide surfaces was the aim of this thesis, no further investigation of the photochemistry on thin MgO films (thickness ≈ 5 ML) was done.

5.3.2 Additional Mg deposition on MgO films

A second way of enhancing the reaction yield would be to create more reaction sites on an already prepared MgO film. The idea is to enhance the number of trapping sites by addition of pure magnesium to the surface. This technique is known in literature [59, 143, 144]: The addition of small amounts of Mg at low temperatures (100 K) would result in the formation of new color centers onto the surface (see Fig. 5.17) - hence the term "magnesium coloring" for this procedure. An in-depth investigation of this color center generation was done by Gonchar et al [143] where they could illustrate that the maximal generation of paramagnetic color centers (F^+ -centers) would peak at ≈ 0.03 ML Mg. At such low Mg doses the number of generated color centers was estimated to be $2 - 3 \cdot 10^{12} \text{ cm}^{-2}$. Since a similar mechanism - the photoninduced electron hole pair excitation followed by an electron trapping - initiates the N_2O dissociation process leading to atomic oxygen onto the surface, a similar reaction gain should be expected. Thus, a series of measurements was established to elucidate whether the addition of small amounts of magnesium would enhance the reaction. As magnesium might instantaneously

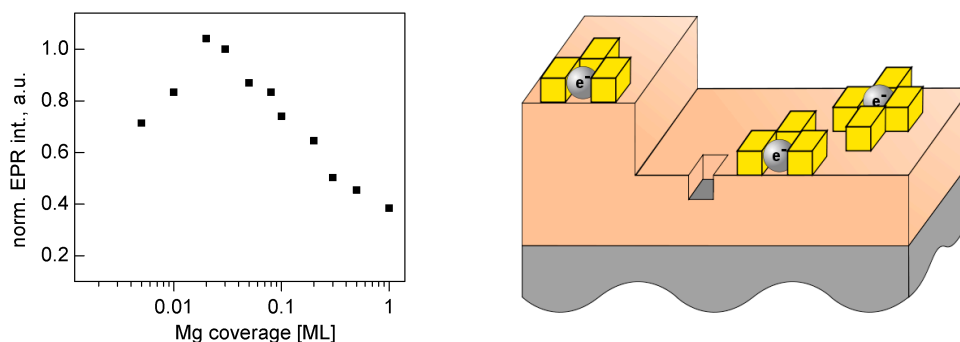


Figure 5.17: Left: integrated Intensity of EPR Signal ($g = 2.0017$) for F^+ centers generated by Mg deposition. As shown, the highest EPR Signal is detected after deposition of 0.03 ML Mg on the surface. This picture is taken from Ref. [143]. Right: Schematic drawing of surface after Mg coloring: at low coverages, Mg forms additional vacancies which can act as electron traps.

form MgO in the presence of atomic oxygen, this N_2O dissociation product is here, in contrast to the measurements presented before, a worse monitor than N_2 , thus the focus will be on the generated nitrogen amount.

On a prepared MgO film (thickness ≈ 20 ML) 0.03 ML magnesium were deposited at low temperatures. On this surface one monolayer N_2O was adsorbed and irradiated. As Fig. 5.18 shows, the reaction yield is increased by 70 % for the first experiment, which confirms the hypothesis of creating more reaction sites. With each measurement cycle (adsorption and irradiation of N_2O , followed by TPD and annealing to 650 K), however, this reaction yield decreases exponentially. Furthermore, the second nitrogen peak at about 80 K is strongly enhanced and the amount of remaining N_2O increases.

The generated reaction centers are unstable at high temperatures, thus it is to be expected that the reactivity reduces after each annealing. The question arises what happens to the pre-adsorbed magnesium: Does it evaporate from the surface or does it form Mg clusters? The incrementation of the remaining amount of N_2O , which is higher than the respective yield loss, shows that the number of N_2O adsorption sites, i.e. the surface area is enhanced. Moreover, the second N_2 peak after the first annealing cycle indicates that a second reaction takes place. This would suggest that additional reaction species not as abundant on pristine MgO are gen-

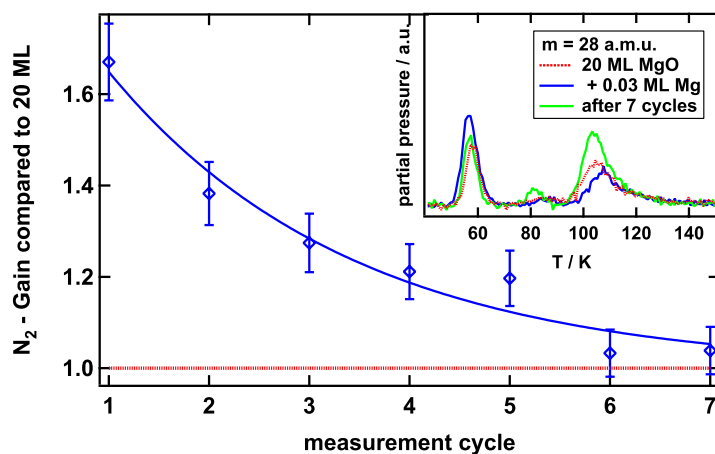


Figure 5.18: Generation of nitrogen (blue) compared to the reaction yield on 20 ML pristine MgO (red). The initial reaction gain is almost 70 %. This gain decreases with each measurement cycle (adsorption and irradiation of N_2O , followed by recording the TPD spectrum and annealing to 650 K) and after seven measurements, the reaction yield is as large as the one on pristine MgO. *Inset:* Raw TPD spectrum of $m = 28$ a.m.u. depicting nitrogen desorption at ≈ 55 K and 80 K and N_2O desorption at ≈ 100 K. The blue line shows the spectrum immediately after Mg deposition, the green one after seven measurement cycles and the red one of pristine MgO. The second nitrogen species at about 80 K is strongly enhanced after several measurement cycles.

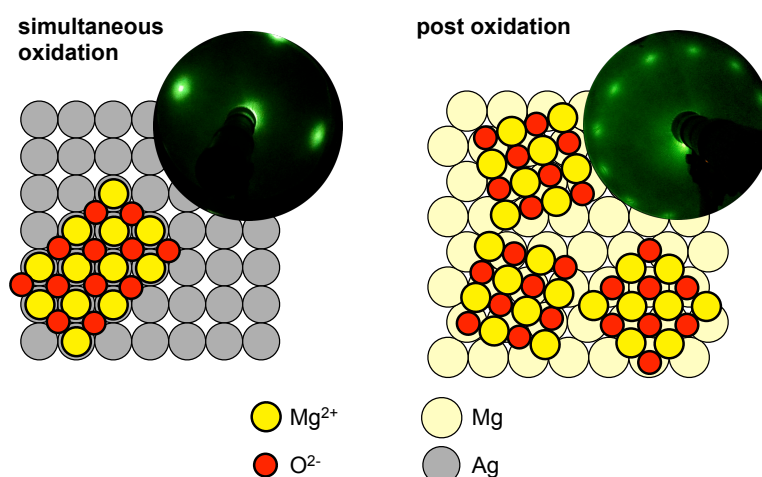


Figure 5.19: Scheme of simultaneous and post-oxidized generation of MgO films and LEED pictures taken at 50 eV for both cases (Film thickness 20 ML). While in the first case, the MgO film grows directly on the Ag(001) surface, post oxidation leads to a rearrangement of the deposited Mg film which is grown in hcp structure. (structure of this picture inspired by Ref. [58], the LEED pictures are recorded in the course of this thesis.)

erated in this process. Thus the hypothesis of a generation of Mg clusters with new properties seems reasonable. In fact, this hypothesis is corroborated by Gonchar et al. [143]: If higher amounts of magnesium are deposited on MgO, IR measurements of CO adsorbed on MgO confirm the generation of a mode associated with CO adsorbed on metal clusters. If, however, this film is annealed to over 100 K, this mode disappears. Thus, they conclude the presence of Mg clusters after the annealing process.

As F^+ sites, i.e. trapped electrons, are generated in this course, a reaction yield *without* irradiation might be expected. This "dark" reaction could not be detected due to the carbon monoxide contaminations at low temperatures which lead to the tempering at 85 K mentioned earlier. However, not only F^+ - sites but also other diamagnetic anion vacancies are generated in this process. Thus, the photogenerated reaction gain serves here as an indirect proof for this hypothesis.

5.3.3 Post-oxidation of magnesium

Another possible method to increase the number of defects (or more specifically to decrease the flatness of the MgO film) is presented in two articles by Wollschäger

et al [58, 145]: By oxidizing a Mg film previously deposited on an Ag(001) surface, the magnesiums' hcp structure would form a MgO film consisting of several domains. These domains are rotated by 60 degree in respect to each other. This results in a twelfefold LEED-pattern as shown in Fig. 5.19.

Three mechanisms are possible:

- The enforcement of different domains might lead to additional electron traps and thus to a higher reactivity.
- A special case would be that this preparation procedure might generate new forms of traps or alter the band structure so that the reaction probability is increased. Kurth et al detected a significantly lower band gap for oxidized magnesium than for bulk MgO [146, 147] (2.5 eV compared to the regular 7.8 eV). Obviously that would be a bad model system for regular MgO.
- The respective domains might be more stable so that this preparation method would result in a smaller reaction yield.

To confirm one of these possibilities, a post-oxidized MgO film was prepared: 20 ML Pure magnesium were deposited on a prepared Ag(001) crystal. The film was then annealed for one hour in an oxygen ambient ($T = 600$ K). Prior to and after this tempering the Auger spectrum for magnesium was recorded to elucidate how oxidized the magnesium is afterwards. A presence of the Mg^0 LVV peak at ≈ 45 eV (see Fig. 5.20) would reveal the presence of metallic magnesium. After tempering the film in an oxygen ambient the Mg^0 LVV peak disappears due to the complete oxidation of magnesium.

If the recorded Auger spectra for both methods are compared, a higher remaining Ag MNN-signal accompanied by a smaller O KLL signal is detected. As no layer by layer growth is expected, the real, local film thickness will differ from the nominal one.

The N_2O adsorbate on MgO films generated by post oxidation is significantly different from N_2O adsorbates on regular MgO as shown in Fig. 5.21. Beside the early multilayer desorption, the most interesting difference is a second desorption peak at ≈ 80 K. This feature must not be confused with the N_2O desorption from Ag(001) which has its maximum at 83 K. It should be noted that this desorption peak coincides perfectly with the expected desorption of the high density phase of N_2O adsorbed on terraces, thus it may be concluded that the abundance of terrace sites is dramatically increased, a result from the growth of different domains.

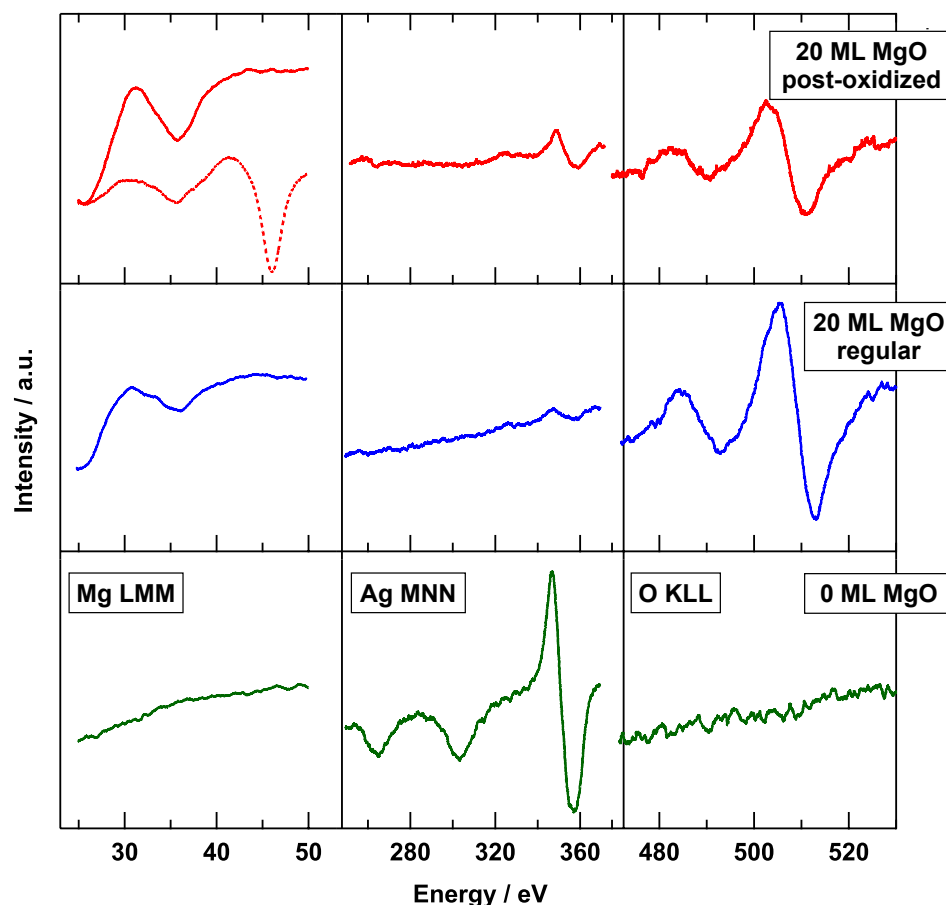


Figure 5.20: Auger electron spectra of bare silver and 20 ML MgO, grown either with simultaneous or post-oxidation. The Mg LMM, Ag MNN and O KLL lines are depicted. A comparison between the Ag and O lines of both film preparation types show that the post-oxidized films appear "thinner" than the regular ones (the remaining Ag MNN signal is larger), an effect which has to be associated with its unusual, multiple domain growth. On the left side, the red dashed line indicates the Auger spectrum of pure magnesium deposited on Ag(001) prior to tempering the Mg film in an oxygen ambient. Beside the Mg LMM peak at 36 eV a second peak at 46 eV, the Mg^0 LVV signal, indicates the presence of non-oxidized magnesium on the surface. The disappearance of the Mg^0 LVV peak confirms that no pure magnesium was present after tempering.

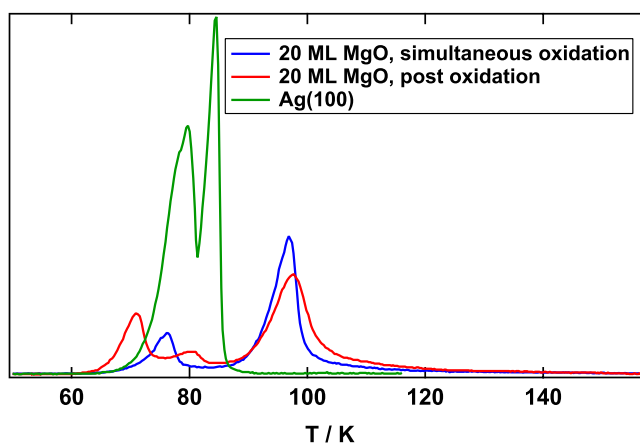


Figure 5.21: TPD spectra of N_2O ($m = 44$ a.m.u.). The blue plot shows the desorption from regular MgO generated by simultaneous oxidation and red one from MgO films prepared by post oxidation of magnesium. As a comparison, the TPD spectrum of N_2O desorbing from Ag(001) is shown in green. As shown, the main difference between the desorption characteristics of N_2O adsorbed on regular MgO and oxidized magnesium is a second desorption peak at 80 K and that the multilayer desorbs earlier.

The desorption of the low density phase and from edges, however, is again at about 97 K. To compare this experiment with the photochemistry of 1 ML N_2O on regular MgO, the adsorbate was again annealed to 85 K prior to irradiation.

From the photochemistry done on regular MgO films, the maximal reaction yield is established at an irradiation of about $2 \cdot 10^{18}$ photons/cm² ($h\nu = 5.0$ eV). N_2O adsorbed on MgO obtained by oxidation of previously adsorbed magnesium was irradiated with the same photon dose to compare the respective reaction yields.

On Fig. 5.22, the resulting generation of N_2 and atomic oxygen and the depletion of the parent mass N_2O is shown. The reaction yield is significantly smaller on MgO prepared by oxidation of previously adsorbed magnesium than on regularly prepared MgO, especially the amount of generated atomic oxygen is negligible. Moreover, the remaining amount of N_2O is much smaller and the shift of the low temperature TPD spectra towards higher temperatures is larger on oxidized magnesium than on regularly prepared MgO.

At a first glance, the interpretation of the raw TPD spectra for N_2 and O_2 would suggest that the reactivity of the post oxidized magnesium would be much smaller compared to the reactivity of regularly prepared MgO. Even though the amount of

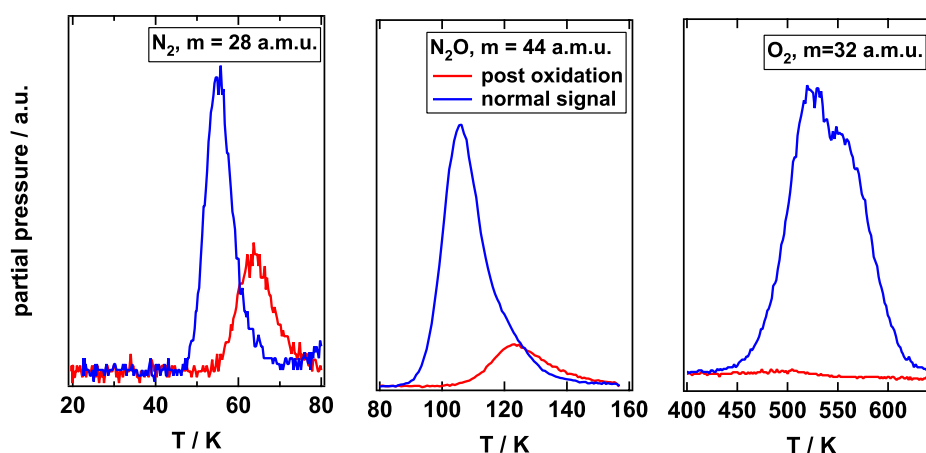


Figure 5.22: TPD spectra after irradiation with 5.0 eV light (photon density: $2 \cdot 10^{18}$ photons/cm²). The photochemistry on regular MgO grown by simultaneous oxidation is blue and the one on post oxidized Mg deposited on Ag(001) is red. As shown, the reaction yield obtained on post oxidized Mg is lower than the one on regular MgO. It should be noted though that the N_2 desorption energy is higher on post oxidized Mg and the remaining amount of N_2O dramatically lower.

oxygen on the surface is almost negligible, the amount of N_2 exceeds this generation significantly ($4 \cdot 10^{12}$ N_2 molecules compared to $2 \cdot 10^{11}$ oxygen atoms). Furthermore, the N_2 desorption peak on post oxidized MgO is shifted towards higher temperatures compared to the one on regular MgO. As mentioned earlier, this shift of the N_2 peak is correlated with the abundance of atomic oxygen on the surface. Finally, the abundance of N_2O after irradiation is significantly smaller on post oxidized magnesium than on N_2O adsorbed and irradiated on regular MgO films.

A promising suggestion is that in fact a lowered band gap accelerates the reaction here: As in the case of electron hole pair excitation at terraces discussed in chapter 5.2.1, the reduced band gap would make it possible to generate a multitude of electron hole pairs. That would increase the probability to trap one electron and thus accelerate the reaction. Thus MgO films generated by post oxidation of Mg deposited on Ag(001) would have a higher reaction probability than regular MgO films.

However, that would lead to the conclusion that this system is a bad model system to investigate the chemistry of regular MgO-surfaces and its low coordinated sites as the dramatically reduced band gap shows. This is also the reason why no further effort was put into investigating the chemical properties of this significantly

different system.

5.4 Observation of free spin by EPR

So far, thermal desorption spectroscopy was solely used to determine and quantify the dynamics on the surface. Though this method has its benefits, its main drawback is that it only detects what desorbs from the surface. In that sense, thermal desorption spectroscopy is a *post-mortem method* and all processes on the surface prior to desorption have to be deduced indirectly.

Many studies of the (photo)chemistry on polycrystalline MgO were done by EPR spectroscopy. The proposed, electron-hole-pair mediated reaction mechanism (see eqs. 5.1 - 5.8) assumes a singly charged oxygen generated by N₂O dissociation which should be detectable by this method. In fact, numerous experimental and theoretical studies [15, 19, 23, 24, 43, 74, 148–151] deal with that subject thus a clear distinction and comparison with theory should be possible.

Investigating this photon-induced process by means of EPR is of particular importance: As already mentioned, the amount of generated atomic oxygen exceeds dramatically the natural abundance of uncharged point defects suggesting that different, *shallow* electron traps act here as localized reaction sites. As the local topology of the single electron charge has a significant influence on the detected g-factor, see chapter 2.5, a comparison with other measurements and theory would possibly shine light on the nature of the electron trapping site.

The EPR measurements were not possible with the used apparatus. In the former FHI working group of Professor Risse (now in the chemistry department of the Free university of Berlin), the needed experimental equipment (and with Dr. Anastasia Gonchar a person gifted enough to work with this machine) was just inside our own institute - a great possibility for a collaboration. However, every adaptation of an experiment in a different apparatus is problematic which is why some experimental details were different: The substrate on which the MgO films were grown was Molybdenum, not Ag(001)³, the crystal was cooled down with liquid nitrogen resulting in a lowest possible temperature of 90 K. Moreover, the irradiation took place in a N₂O atmosphere (10⁻⁶ mbar).

Since the prepared MgO film has a thickness of 20 ML, the different substrates' influence should be negligible. As Fig. 5.23 shows, it is possible to generate atomic

³For the EPR experiments, crystals with two polished surfaces were needed. According to the respective working group it is not possible to prepare Ag(001) crystals in that manner.

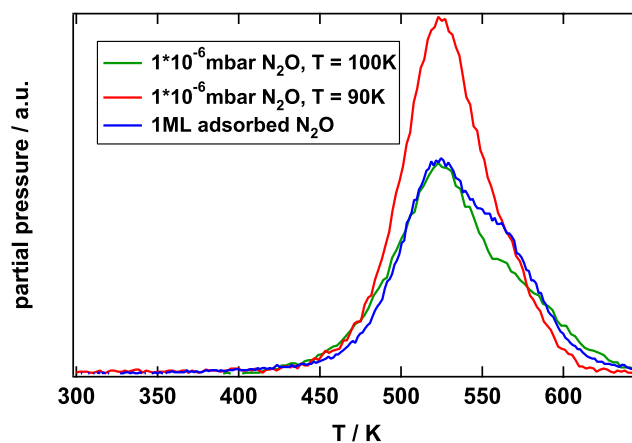


Figure 5.23: TPD spectra of O_2 resulting from recombinative desorption of atomic oxygen of 1 ML N_2O adsorbed on MgO (blue) and in $1 \cdot 10^{-6}$ mbar dynamic N_2O vacuum at a sample temperature 90 K (red) and 100 K (green) after irradiation with 5.0 eV light (photon density: $2 \cdot 10^{18}$ photons/cm²). As the desorption temperature of N_2O is 100 K, the atomic oxygen generation in an N_2O atmosphere is in acceptable agreement with the one of pre-adsorbed N_2O . The similar binding energy suggests for all systems a similar oxygen generation mechanism.

oxygen on MgO surfaces by irradiating the sample within a N_2O atmosphere. Thus, the higher surface temperature and the reaction in dynamic vacuum does not alter the generation of atomic oxygen - as the desorbing N_2O at reactive sites is replenished by N_2O from the gas phase, the amount of atomic oxygen is, in fact, even higher than the respective amount after irradiation of 1 ML N_2O adsorbed on MgO.

A prepared MgO film (20 ML) grown on Mo was irradiated in a N_2O atmosphere ($p = 1 \cdot 10^{-6}$ mbar, $h\nu = 5.0$ eV, photon dose $\approx 2 \cdot 10^{18}$ photons/cm²). The EPR spectra themselves show two distinct features after irradiation (see Fig. 5.24): The parallel component of the g-value (g_{\parallel}) at 2.004 and the perpendicular component of the g-value (g_{\perp}) at 2.023. A look in literature reveals that these values are known on polycrystalline material from experimental studies in the working group of Knözinger [15, 24, 152]: UV-irradiation of MgO powder in H_2 atmosphere creates trapped electrons (and thus an EPR-Signal) at distinct sites. A reaction with N_2O results in different new EPR-signals. One of the detected EPR signals coincides with the g_{\perp} -value measured in this thesis. The nature of these different signals was discussed theoretically [74, 149].

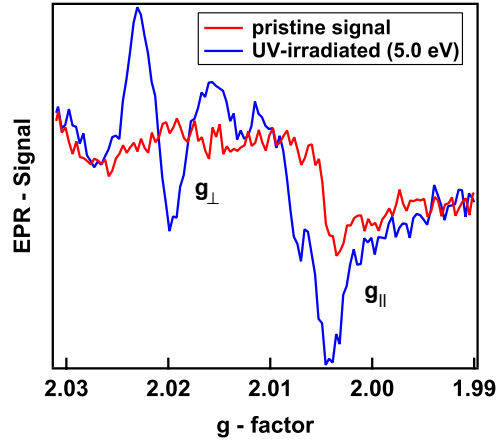


Figure 5.24: EPR-spectra of MgO/Mo prior to (red) and after (blue) UV irradiation in a N_2O atmosphere ($p = 1 \cdot 10^{-6}$ mbar). Two signals are appearing, $g_{\perp} \approx 2.023$ and $g_{\parallel} \approx 2.004$.

The g-values themselves are approximated as

$$g_{\parallel} \approx g_e \quad (5.9)$$

$$g_{\perp} = g_e + (c/\Delta E) \quad (5.10)$$

The parallel component of the g-value is about 2.002 and thus not much affected by the local topology. However, the perpendicular component of the g-value is dependent on the energy difference ΔE between the p_z level which contains the electron hole and the two degenerate p_x and p_y levels. ΔE represents the local crystal field splitting of the energy levels and thus is highly sensitive on the local topology of the respective surface site. Moreover, it is dependent on the spin-orbit constant of oxygen which is proportional to the constant c .

This crystal field splitting was calculated in the already cited publications [74, 149]. Both theoretical studies are from the working group of Giamello. They modeled singly charged atomic oxygen in different environments to calculate the local crystal field splitting. For the present case, the two structures which fit best are the reverse corner and the divacancy at edges ⁴.

⁴All calculated values are smaller than the crystal field splitting value corresponding to $g_{\perp} = 2.023$, thus it is assumed that the largest calculated crystal field splitting factors correspond to the largest derived from experiment.

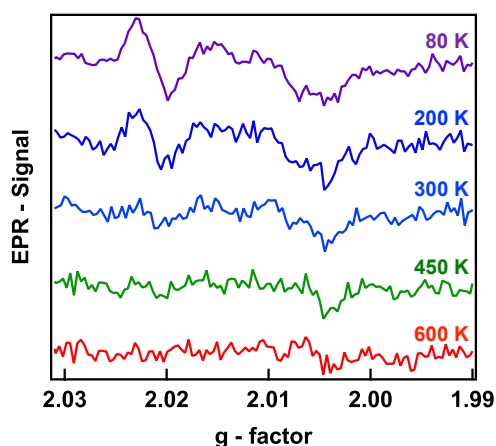


Figure 5.25: A temperature - dependent investigation of the EPR signatures generated by UV induced N_2O dissociation on MgO/Mo reveals that the g_{\perp} component is almost vanished at about 300 K while the g_{\parallel} component vanishes at 600 K. From all signals the EPR signature of MgO without irradiation is subtracted.

This should not be too surprising: Point defects are, as already explained, scarce on thin films. The abundance of generated atomic oxygen exceeds the expected number of point defects significantly. As no hydrogen was introduced into the system and no protonated sites to stabilize the electron should be expected, only reverse corners and divacancies are suitable candidates as electron traps and thus as localization points for the generated atomic oxygen.

A look at the temperature-dependence of both components of the g-factor (see Fig. 5.25) induced by UV irradiation in a N_2O atmosphere clearly shows that the g_{\perp} component of the g-factor is almost vanished after annealing up to 300 K. As this component of the g-factor is (unlike g_{\parallel}) a distinct feature resulting solely from the generation of atomic oxygen, it seems reasonable to assume the free spin associated with it is generated oxygen vanishes at temperatures at about 300 K. In fact, as will be seen in chapter 6.1, this generated atomic oxygen also reacts with carbon monoxide only at temperatures below 300 K. Despite this agreement concerning the reactivity, it is yet an open question to answer the discrepancy between the temperature where the free spin radical vanishes in EPR data and the temperature where oxygen desorbs recombinatively.

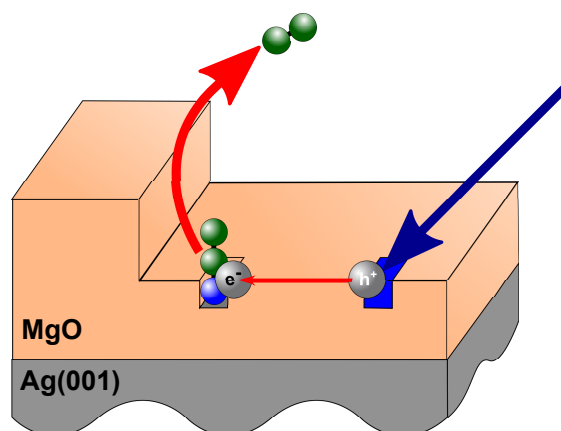


Figure 5.26: Schematic representation of one reaction path (eqs. 5.1 - 5.3). An incoming photon (dark blue) generates an electron - hole - pair where the electron gets trapped. If a N_2O molecule is adsorbed in the vicinity of the trapped electron the electron leads to a dissociation of N_2O forming atomic oxygen and N_2 .

5.5 Conclusion

In this chapter, the photon induced N_2O dissociation on thin MgO films grown on Ag(001) was investigated. When irradiating N_2O adsorbed on MgO with UV-light ($h\nu = 4.0 \text{ eV}$, 4.6 eV , 5.0 eV and 6.4 eV) four processes are detected by post-irradiation TPD spectra:

- Depletion of N_2O
- formation of nitrogen desorbing at $\approx 55 \text{ K}$
- generation of tightly bound atomic oxygen desorbing at 520 K and 570 K
- a shift of the low temperature TPD spectra towards higher temperatures.

The latter observation was, in agreement with literature, interpreted as an influence due to atomic oxygen on the surface. On the basis of an electron-hole-pair induced N_2O dissociation mechanism a reaction model containing two reaction pathways was proposed. This hypothesis was confirmed by the photon-dependent behavior of the two oxygen desorption peaks.

The implementation of the reaction mechanism and comparison with the experiment was implemented with Mathematica. A schematic representation of the first

reaction path (eqs. 5.1 - 5.3) is shown in Fig. 5.26. The overall mechanism is described as follows: a photon generates an electron-hole-pair by lifting an electron from the valence bond into the conduction bond of MgO . This electron-hole-pair is transferred along sites with the same coordination until the electron is trapped. If N_2O is adsorbed in its vicinity, the nearby electron causes a dissociation of the molecule forming nitrogen and atomic oxygen. Furthermore, as the presented measurements suggest, the hole itself also can initiate a N_2O dissociation. The presented model has to assume that the desorption cross section of nitrogen generated by this second reaction pathway is very high as the discrepancy between generated oxygen and generated nitrogen indicates.

Photon-energy dependent measurements confirm that the reaction could be initiated site-selectively. A dramatic increase of the cross sections was measured when exciting electron-hole-pairs at terraces. This increase is correlated to the higher number of excited electron hole pairs which artificially increase the trapping and reaction probability.

Coverage-dependent measurements confirm a positive correlation between the saturation of the N_2O monolayer peak at 97 K and the maximal reaction yield at edges. The high number of N_2O molecules contained in this monolayer suggest that this desorption peak does result also from the N_2O desorption at terraces. The dramatic yield increase when a N_2O monolayer was irradiated with 6.4 eV instead of 5.0 eV confirms this.

Different preparation methods were examined with the goal to increase the number of defects and thus the reaction yield. The simplest and most stable way was to manipulate the MgO film thickness. It could be shown that in a range from zero to thirty monolayers MgO the amount of generated atomic oxygen after N_2O dissociation increases quadratically. The interpretation is based on the increasing surface roughness with MgO film thickness which leads to a higher number of defects causing N_2O dissociation.

To examine the free spin resulting from generating singly-charged atomic oxygen EPR spectroscopy was used to study this process. The signatures evolving correspond to a g -tensor with components $g_{\parallel} = 2.004$ and $g_{\perp} = 2.023$. As the g_{\perp} value is antiproportional to the crystal field splitting, a comparison with theoretically calculated field splitting values suggest that the electron trapping sites are of an extended nature like divacancies of reverse corners.

When investigating the temperature dependence of this EPR signal, it is striking to notice that the g_{\perp} component associated with singly-charged atomic oxygen

vanishes already at about 300 K. Thus, prior to desorption, atomic oxygen loses its charge.

To analyze the oxygen behavior between 300 K (the temperature when atomic oxygen loses its associated free spin) and 500 K (the temperature when oxygen desorbs) the chosen approach was to record the evolution of a signal correlated to atomic oxygen by means of HrEELS. However, the expected signal for atomic oxygen would be a small loss ($<1000\text{ cm}^{-1}$), a spectral region dominated by the fundamental of the surface phonon modes, see Fig. 3.5. As no hint of atomic oxygen was found in the data after photoinduced N_2O dissociation, it seems that the loss of atomic oxygen is negligible compared to the phonon mode. Unfortunately, to the authors best knowledge no stable method to extract also this large feature from the data is known.

Chapter 6

Oxidation by pregenerated atomic oxygen

Chapter 5 discussed how atomic oxygen was generated on MgO films by photoinduced N_2O dissociation. As one motivation for this thesis was to investigate the charge-induced chemistry on oxide surfaces, the chemistry of these generated localized atomic oxygen sites was investigated.

In a first series of experiments, the possibility to dissociate CH_4 at singly-charged atomic oxygen sites was examined. The motivation for that is the claim stated by Lunsford et al that singly charged atomic oxygen (generated by Lithium doping of MgO) would enhance the reaction yield and selectivity towards methane dissociation [5]. It has to be pointed out, however, that methane dissociation could not be initiated under laboratory conditions. The results of that study and its discussion are shown in Appendix A.

Another experiment is the investigation of CO oxidation with pregenerated atomic oxygen on MgO surfaces. The oxidation of carbon monoxide was investigated thoroughly on metal surfaces and on oxide surfaces. For an overview see Ref. [153]. In the study presented here, the oxidation properties with atomic oxygen generated by photoinduced dissociation of N_2O were investigated.

6.1 CO and CO/O coadsorbates adsorbed on MgO

A closer look at the adsorption characteristics of CO on bare MgO surfaces and CO adsorbed on MgO surfaces with pregenerated atomic oxygen is presented here. The former one will be mainly based on the experimental measurements [103] and

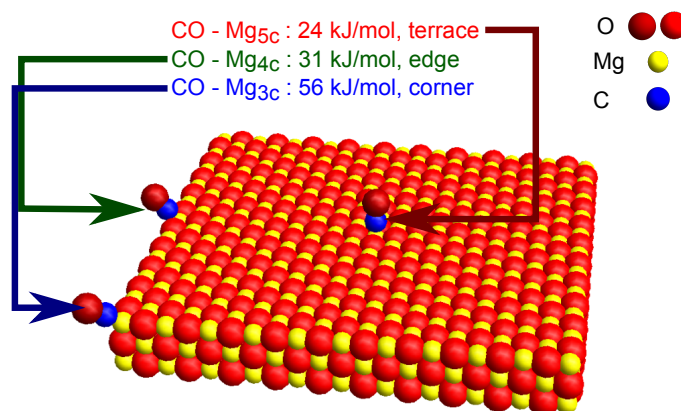


Figure 6.1: Carbon monoxide adsorbed on MgO sites with different coordination. DFT calculations suggest that CO adsorbs with the carbon terminated end at Mg cation sites. The calculated adsorption energies taken from Ref. [154]

theoretical calculations [154] done by others while in the latter one the measurements and interpretations of Dohnalek et al is extended to MgO + O coadsorbates.

The adsorption of carbon monoxide on MgO is a topic discussed in great depth and with contradicting results [155]: The local coordination of the respective surface site has a huge influence on the adsorption properties of CO which results in a large distribution of experimentally and theoretically derived adsorption energies for CO molecules adsorbed on MgO surfaces.

Pacchioni et al calculated adsorption energies for CO molecules adsorbed on terraces, edges and corners as 24 kJ/mol, 31 kJ/mol and 56 kJ/mol, respectively [154], see Fig. 6.1. So, as in the case of N₂O on MgO, a lower coordination of the adsorption site leads to a higher adsorption energy.

This result is experimentally verified by TPD studies [103, 156](see Fig. 6.2): From the inverted Polanyi-Wigner plots the desorption energies of CO adsorbed on terraces, edges and corners could be estimated as 20 kJ/mol, 30 kJ/mol and 33 kJ/mol, respectively. While dramatic difference between the calculated and the measured desorption energy of CO desorbing from corners is evident, the other values derived from TPD spectra fit to theoretical expectations.

Adsorbate-adsorbate interactions are present for higher coverages and lead to a phase change of the adsorbate: at coverages above 0.8 ML, the regular 1×1 structure changes into a $c(4 \times 2)$ structure; the additional small peak at 45K results from carbon monoxide desorption during the phase transition.

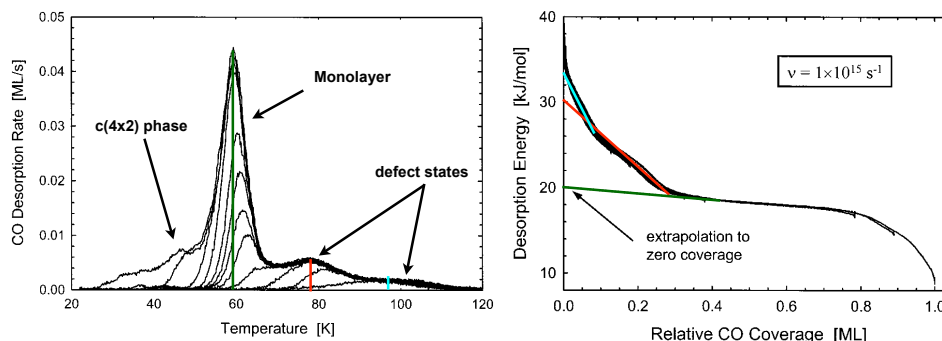


Figure 6.2: TPD spectra (left) and corresponding inverted Polanyi-Wigner plots (right) of CO adsorbed on MgO. The pictures are taken from Ref. [103]. Two defect peaks are clearly visible at about 78 K and 95 K and can be correlated to CO desorbing from edges and corners, respectively. Small lateral interactions result in a decreasing adsorption energy with coverage.

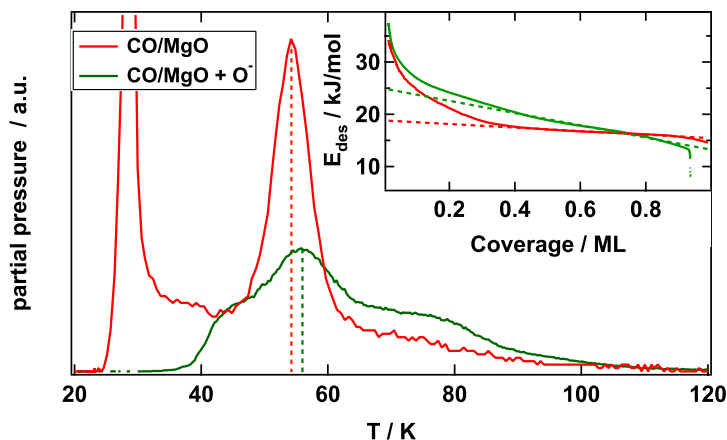


Figure 6.3: TPD spectra of CO ($m = 28$ a.m.u.) adsorbed on pristine MgO (red) and together with previously generated atomic oxygen (green). The desorption peak is shifted 2 K towards higher temperatures and the peak shape is broadened in the presence of atomic oxygen. An inverted Polanyi-Wigner plot (inset) shows a strong dependence of the desorption energy with respect to the coverage, thus the lateral interactions are dramatically increased for a CO + O⁻ coadsorbate.

As the oxidizing properties of atomic oxygen were object of this research, the adsorption properties of a *coadsorbate* consisting of carbon monoxide and pre-generated atomic oxygen generated by photoinduced N_2O dissociation are mandatory for further discussion. This coadsorbate will from now on be referred to as $\text{MgO} + \text{O}^-$. As Fig. 6.3 shows, the maximal desorption rate of CO adsorbed (i.e. the peak of the referring TPD spectra) on $\text{MgO} + \text{O}^-$ surfaces is shifted 2 K to higher temperatures compared to CO adsorbed on regular MgO and the whole desorption peak structure is broadened. Moreover, a higher amount of carbon monoxide molecules is adsorbed at defect sites. An inverted Polanyi-Wigner plot analysis reveals that the adsorbate-adsorbate interactions are increased dramatically resulting in a higher initial desorption energy (24 kJ/mol compared to 19 kJ/mol) with an increased coverage dependence.

Summarizing, it is obvious that the presence of atomic oxygen alters significantly the properties of the CO adsorbate. The shift of the desorption peak towards higher temperatures resembles the shift of low TPD spectra discussed in chapter 5.1, and thus can also be correlated to the presence of atomic oxygen. However, no carbon dioxide is generated in this manner which clearly shows that the reaction energy to form carbon dioxide out of atomic oxygen and CO is too high to be overcome at temperatures below 120 K.

6.2 UV-irradiation of $\text{CO}/\text{N}_2\text{O}$ and CO/O coadsorbates

The coadsorption of CO and previously generated atomic oxygen has shown that the activation energy to induce CO oxidation is too large to be overcome by thermal means alone. Thus, two approaches were investigated with the aim to initiate CO oxidation on MgO surfaces:

- N_2O and CO were dosed onto the surface and irradiated afterwards.
- Adsorption of CO on MgO surfaces where atomic oxygen was pregenerated by photoinduced N_2O dissociation. This CO-adsorbate was irradiated a second time after the sample was heated up to 160 K

In the first experiment, N_2O and CO were adsorbed on MgO and irradiated ($h\nu = 5.0 \text{ eV}$, $2 \cdot 10^{18} \text{ photons/cm}^2$). As shown in Fig. 6.4, CO_2 is evidently generated by shining light onto a coadsorbate consisting of N_2O and CO. One interpretation would be that CO interacts with N_2O directly during photoexcitation which would

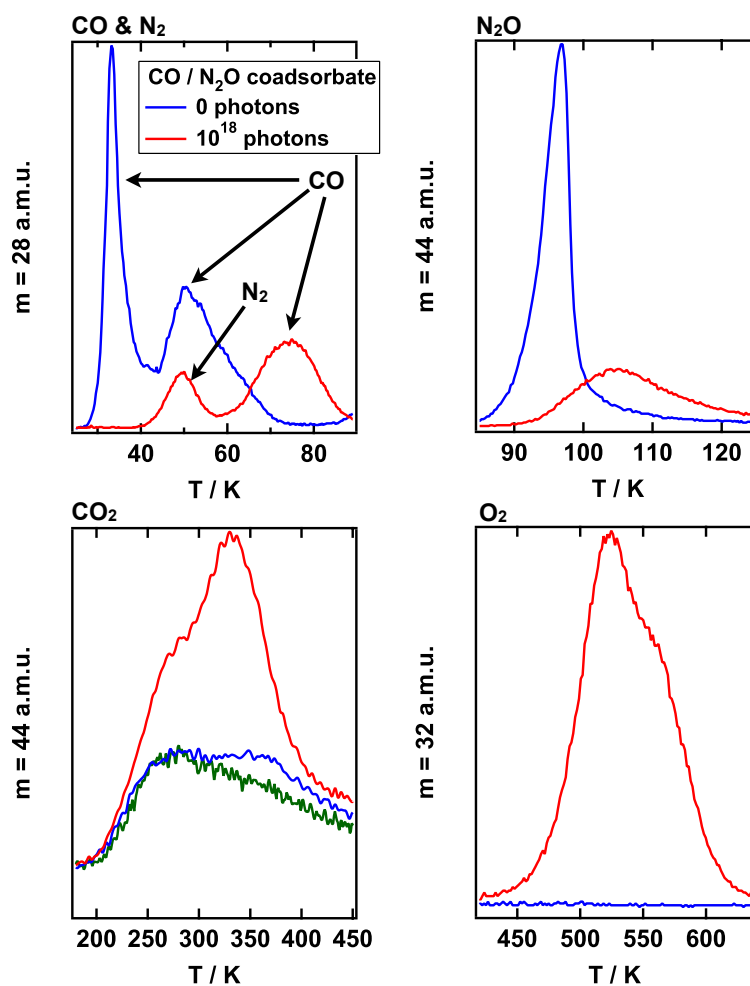


Figure 6.4: TPD spectra of CO and N₂ (top, left), N₂O (top, right), CO₂ (bottom, left) and O₂ (bottom, right) before (blue) and after (red) 5.0 eV irradiation. All pictures are normalized with respect to the highest peak in the picture - compared to the low temperature TPD spectra, the height of the CO₂ and O₂ desorption peaks is very small. N₂ appears in form of a desorption peak at about 55 K after irradiation due to the N₂O dissociation while the remaining CO shifts dramatically towards higher temperatures. The green plot in the third panel is an upscaled trace of a signal at m = 30 a.m.u. and thus indicates a small high-temperature desorption of N₂O.

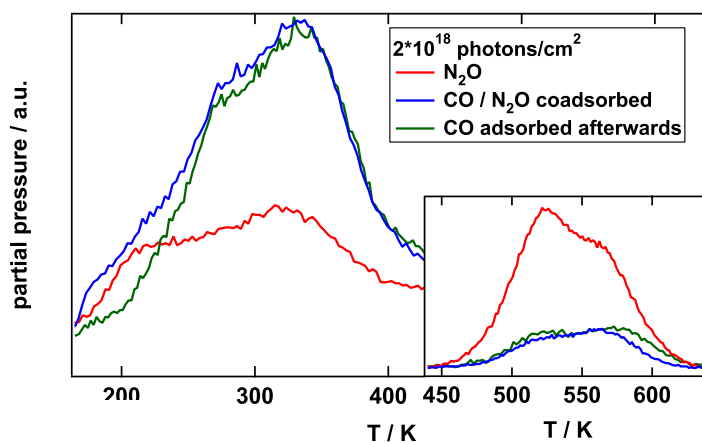


Figure 6.5: TPD spectra of CO₂ and O₂ (inset) generated by irradiation of a CO / N₂O coadsorbate (blue) and by second irradiation of CO adsorbed on MgO after generation of atomic oxygen (green). The red lines denote the amount of CO₂ and high temperature N₂O (see Fig 6.4) and O₂ without interaction with CO. The almost identical results and the smaller amount of atomic oxygen in case of CO₂ generation show that the reaction takes place between atomic oxygen and CO.

simply mean that the generated atomic oxygen does not react with CO. Another interpretation is that the reaction with atomic oxygen needs a hyperthermal excitation provided by UV irradiation. An easy way to deduce whether adsorbate - adsorbate reactions between N₂O and CO or reactions between atomic oxygen and CO are the underlying reason for the oxidation process is by irradiating coadsorbate consisting of CO and atomic oxygen generated by photoinduced N₂O dissociation a second time. The resulting generation of carbon dioxide (see Fig. 6.5), accompanied by a decreasing abundance of oxygen show that the reaction takes place between atomic oxygen and carbon monoxide and that N₂O serves only as a promoter for atomic oxygen.

It has to be mentioned that no carbon dioxide is generated by annealing the sample to over 300 K prior to coadsorption of CO. This is in agreement to the EPR-measurements discussed in chapter 5.4. It was discussed that the EPR signal correlated to the presence of atomic oxygen on the surface vanishes after annealing to ≈ 300 K (see Fig. 5.25) which is interpreted as an oxygen atom losing its single free charge and thus its high probability to react.

As the interaction between atomic oxygen and CO was focus of this experiment, only the photon dose dependence of CO+O systems was studied - the CO+N₂O

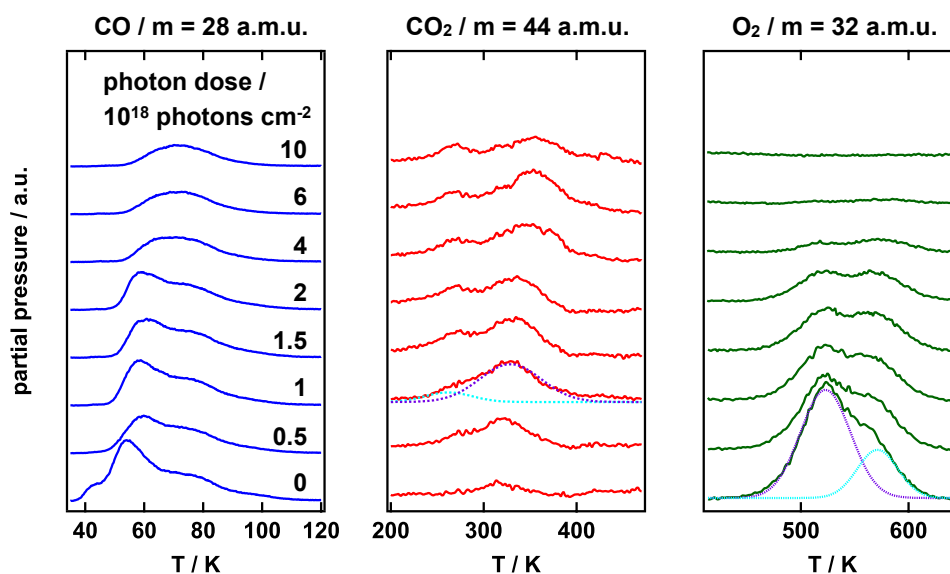
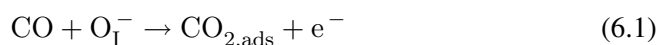


Figure 6.6: Raw TPD spectra of CO adsorbed on MgO + O⁻ systems in dependence of photon counts. On the left and right panel, the reaction educts CO and oxygen are plotted in blue and green, respectively, while the central panel shows the reaction product CO₂ in red. The amount of oxygen is completely and the one of CO partially depleted in course of irradiation while the number of generated CO₂ molecules rise up and then stay almost constant. The purple and cyan lines denote, as previously described, the presence of two different oxygen species and their corresponding CO oxidation products.

coadsorbates were after UV irradiation complicated systems consisting of five compounds (N₂, CO, N₂O, CO₂ and atomic oxygen). The raw data (Fig. 6.6) shows a complete depletion of the oxygen peak, a small depletion of the CO adsorbate and the generation of CO₂ at two peaks (270 K and 330 K). For better analysis, the signal corresponding to a high temperature desorption of N₂O, see Fig. 6.4, is subtracted from this data. This generation saturates, but, unlike the pre-generated O₂, does not decay at prolonged irradiation times. Similarly, the CO desorption cross section is small compared to the one of N₂O.

Both peaks in the oxygen desorption spectrum decay and also the CO₂ desorption peak show two distinct features. In that sense it seems reasonable to use an approach similar to the two reaction mechanisms discussed in chapter 5.1:



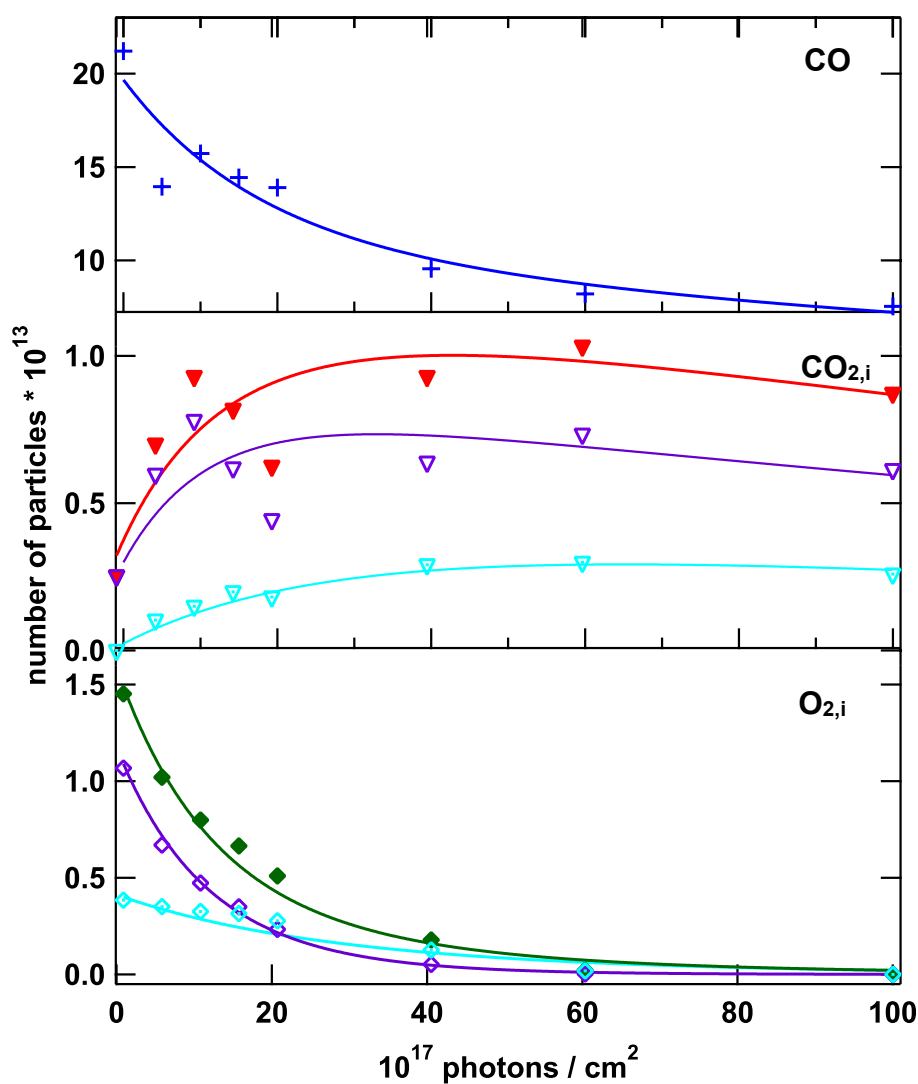


Figure 6.7: Number of CO molecules, CO₂ molecules and oxygen atoms in dependence of photon counts. The solid lines denote the solution of eqs. 6.1-6.2 and additional desorption pathways for the abundance of the respective compounds, while the blue crosses, the red triangles and the green squares correspond to the experimentally determined number of CO, CO₂ and oxygen particles, respectively. These particle numbers were obtained by conversing the raw TPD spectra in Fig. 6.6. The complete abundances of CO₂ and atomic oxygen result from two atomic oxygen species, as denoted in purple and cyan symbols and lines. The atomic oxygen is completely depleted in the course of this experiment while only about fifty per cent of the adsorbed CO is desorbed or oxidized. As the number of generated CO₂ molecules shows, approximately fifty per cent of the previously generated oxygen atoms serve as oxidants.



The above pathways, accompanied by desorption pathways for the respective compounds, were fit to the number of particles derived from TPD spectra. As shown in Fig. 6.7 this reaction model is able to describe the experimental result well. With this reaction model it can be concluded that about fifty per cent of the pre-generated atomic oxygen serves as an oxidant in the induced reaction. The evolution of the two CO₂ desorption peaks can unambiguously referred to the respective reaction pathways: The peak at 330 K results from CO - oxidation of atomic oxygen generated at electron traps (by reaction path 5.3) and corresponds to the oxidation pathway eq. 6.1. The CO₂ desorption peak at 270 K results from oxidation of oxygen generated by N₂O dissociation at localized holes (reaction path 5.8) and thus corresponds to the second oxydation pathway eq. 6.2. The cross sections for both reaction pathways are are 1·10⁻¹⁸ cm² and 5·10⁻¹⁹ cm², respectively, thus slightly larger than the previously mentioned N₂O dissociation cross sections for $h\nu = 5.0$ eV (see table 5.1).

A question that remains unanswered is the role of the second photoexcitation. As already discussed, local heating alone seems unreasonable - and 5.0 eV is a too high energy to induce a simple thermal process. So far, it seems that the CO + O complex is excited electronically and thus overcomes the reaction barrier separating this complex from CO₂.

If the reaction model proposed in eqs. 6.1-6.2 (plus desorption pathways for the respective compounds) is valid, the poisoning of the reaction sites concerning the dissociation of N₂O should be partially suppressed after CO oxidation. Atomic oxygen is for the photoinduced N₂O dissociation on MgO one reaction product on the one and the poisonous influence on the other hand, because atomic oxygen blocks one electron trap. An experimental evidence for this poisonous influence was shown in Fig. 5.2. CO is thought to react with the pregenerated atomic oxygen, thus a recovery of the reactive sites should be visible.

To confirm this hypothesis, the recovery of oxygen generation after four cycles of N₂O adsorption, photodissociation and annealing to 160 K was studied. It was discussed in chapter 5 that annealing to 300 K leads to a partial recovery of the nitrogen generation. As Fig. 6.8 shows, the photoinduced CO oxidation leads to a higher recovery concerning the photoinduced N₂O dissociation than the respective annealing, revealing that more electron traps are free again after CO oxidation. Though no complete recovery could be established the before mentioned hypothe-

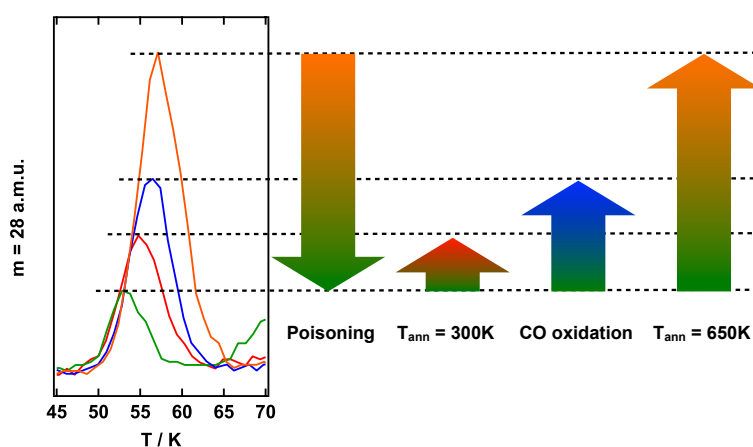


Figure 6.8: Raw TPD spectra of photogenerated N_2 initially and after annealing up to 650 K (orange) and after four cycles of photoinduced N_2O dissociation without annealing to over 160 K (green). Annealing up to 300 K (red) and photoinduced CO oxidation with pre-generated atomic oxygen (blue) prior to another UV induced N_2O dissociation lead to a partial recovery of the photoinduced N_2 generation. Moreover, the hyperthermal way of releasing previously blocked atomic oxygen sites by CO oxidation is more effective than heating the sample up to 300 K. The arrows on the right side illustrate the different amounts of recovery.

sis could be verified.

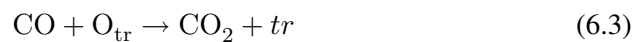
6.3 Conclusion

As a prototype system for reaction with atomic oxygen the CO oxidation on MgO surfaces was investigated. The atomic oxygen was generated by photoinduced N₂O dissociation. If CO was coadsorbed with atomic oxygen without further irradiation, no reaction could be detected. However, a second photoexcitation at temperatures lower than 300 K resulted in a generation of atomic oxygen.

If the sample is annealed to over 300 K prior to CO oxidation, no reaction occurs. This finding is interesting as it corroborates the EPR study which has shown that the free spin associated with atomic oxygen disappears at these temperatures. Thus the atomic oxygen is only reactive as long as its single negative charge is maintained.

The reaction is described by two CO oxidation pathways (eqs. 6.1 and 6.2): One at atomic oxygen generated at trapped electrons (eq. 5.3), the other one at atomic oxygen generated at localized holes (eq. 5.8). Their respective cross sections are $1 \cdot 10^{-18} \text{ cm}^2$ and $5 \cdot 10^{-19} \text{ cm}^2$.

The overall mechanism, i.e. the N₂O dissociation followed by CO oxidation (as depicted in Fig. 6.9), is a model system for a Mars-van Krevelen mechanism. In that catalytic reaction scheme, an adsorbed particle gets oxidized by oxygen atoms associated to the catalyst leaving a vacancy behind which becomes refilled by re-oxidation.



Here, the *tr* denotes a vacancy serving as an electron trap. For CO oxidation on oxides, such a Mars-van Krevelen mechanism was investigated by Lei et al [157] in the CO oxidation on FeO-films grown on Pt(111). Here, a reaction with an oxidant (O₂ or NO) transforms the bilayer FeO film into a trilayer FeO_{2-x} film. The oxidation of CO occurs then at the outermost oxygen layer. The formed CO₂ leaves behind a vacancy which gets oxidized again. As this experiment was done at high temperatures and pressures, the reaction path in two steps could only be deduced.

In the presented case, however, both reaction steps - the adsorbate oxidation and the (re-)oxidation of the vacancy - are completely separable. As it was shown,

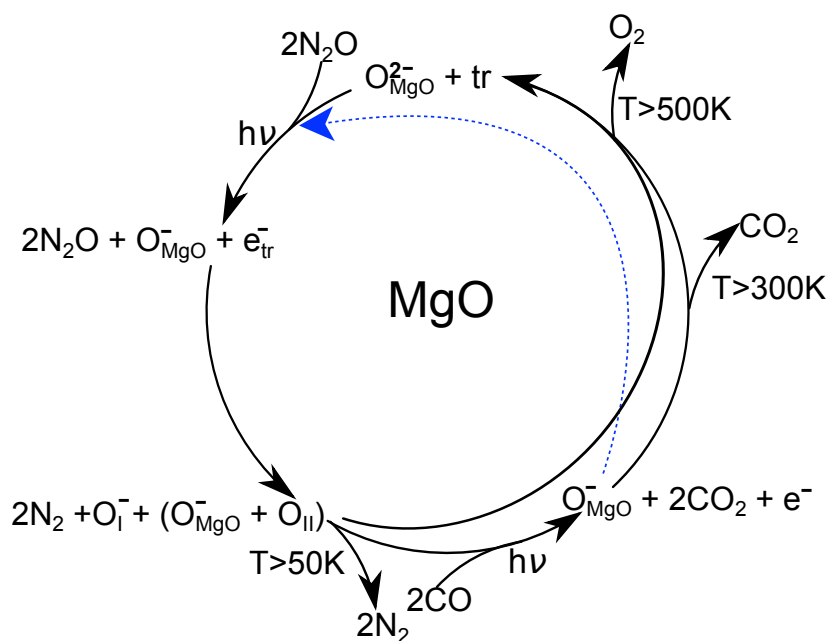


Figure 6.9: Scheme for the photoinduced reactions and thermally induced desorption processes studied in this thesis: The irradiation of N_2O adsorbed on certain trapping sites and in the vicinity of oxygen anions leads to formation of localized charges which force the adsorbed N_2O to dissociate (see reaction pathways eq. 5.3 and 5.8). If CO is adsorbed with the pregenerated atomic oxygen (O_I and O_{II}) and if this system is irradiated a second time, carbon dioxide is formed following the reaction pathways eq. 6.1 and 6.2 and some of the electron trapping sites formerly blocked by atomic oxygen are again available for dissociating N_2O . However, this CO oxidation can only take place before annealing to over 300 K.

a catalytic cycle could be partially modeled by inducing a CO oxidation after blocking of all reaction sites by atomic oxygen: The vacancies mandatory for N₂O dissociation were available again.

Chapter 7

Summary and Outlook

The aim of the presented study was to gain insight into the reaction mechanisms and the reaction cross sections of photochemical processes on oxide surfaces. The here researched model system was atomic oxygen generation by photoinduced N_2O dissociation on MgO films grown on Ag(001). Beside an analysis of this model system the reactivity of the generated atomic oxygen was investigated. Irradiation of N_2O adsorbed on MgO leads to a depletion of N_2O , the formation of nitrogen and oxygen. In contrast to N_2 which desorbed at about 55 K, the generated oxygen desorbed at high temperatures (520 K and 570 K) which was interpreted as a recombinative desorption of atomic oxygen.

The photon dose dependence of the respective amounts of N_2O , N_2 and atomic oxygen was quantified by applying a substrate-mediated mechanism involving two reaction pathways and photon-induced desorption pathways. The reaction mechanism is based on a photon-induced electron-hole-pair generation: An electron is excited from the valence band to the conduction band and thus an electron-hole-pair is formed. As the band gap of MgO varies with the coordination of the respective site, the excitation site is dependent on the used photon energy. The generated electron-hole-pair is mobile along sites with the same or lower coordination until the electron is trapped at sites with a distinct electron affinity. The transfer process leads to one localized electron and one localized hole in its vicinity. If N_2O is adsorbed nearby one of these localized charges, this molecule dissociates forming N_2 and singly charged atomic oxygen.

The application of different photon energies confirms this model: For example, photoexcitation with 6.4 eV photon energy generates electron-hole pairs at terraces, in contrast to the electron-hole pair generation at edges when using photons with an energy of 5.0 eV to initiate the reaction. As the abundance of terrace sites will

be significantly larger than the one of edge sites, a larger reaction yield is expected for initiating the reaction at terraces.

By controlling the MgO surface roughness, and thus the number of defects and electron trapping sites, the amount of generated atomic oxygen could be manipulated. As the thermal stability of MgO is significantly higher compared to Ag(001), the roughness of the MgO surface increases with film thickness.

EPR spectroscopy done in collaboration with the department of Hajo Freund confirmed the presence of singly charged atomic oxygen after photodissociation of N₂O. A comparison of the obtained *g*-values and DFT calculations suggest extended defects like divacancies or reverse corner sites to be the electron trapping sites. The signal corresponding to this atomic oxygen vanishes at about 300 K, in contrast to the oxygen desorption at higher temperatures.

Furthermore, the oxidation of CO coadsorbed with previously generated atomic oxygen on MgO films was studied. It could be shown that an irradiation of this coadsorbate ($h\nu = 5.0$ eV) led to the formation of CO₂ desorbing at 270 K and 330 K. However, if the MgO film with pregenerated atomic oxygen is annealed to over 300 K prior to coadsorption of CO, no reaction could be initiated. Correlating the aforementioned EPR measurements to this finding, the conclusion is that a reaction can only be established as long as the negative charge is maintained.

Summarizing, this study provided insight into the reaction mechanisms of photoinduced N₂O dissociation on thin MgO films, into the site selectivity with respect to the used photon energy, and into the influence on the reaction itself by film preparation. By varying the photon dose and photon energy or by preparing films of different surface quality, the amount of generated oxygen could be controlled and this study provided insight into this model reaction from a chemical point of view.

To extend this knowledge and obtain more physical understanding, a possible approach for further investigation would be to study the electronic structure of the occurring species. Photoelectron spectroscopy methods would provide insight into the bonding type of N₂O as well as the reaction products N₂ and atomic oxygen on MgO. The use of two-photon-photoemission (2PPE) is a feasible method to study the time dependence of the several elementary reaction steps by examining the time-dependent electronic structure: the electron-hole-pair excitation, the trapping of the electron and the reaction itself. The investigation of the electronic structure during irradiation would in particular extend the knowledge of the CO oxidation with atomic oxygen and lead to an understanding of this photoexcitation step.

Another direction would be to study the *desorbing* species during UV-irradiation. The gap between photodissociation and photodesorption could be closed by applying angle-resolved time of flight measurements (TOF). To gain microscopic insight into the energy transfer mechanisms due to photodesorption, resonance enhanced multi photon ionization (REMPI) could be applied as well. A REMPI study would serve as a connection point to the investigation of the electronic structure.

These possible further experiments would extend the insights reported in this thesis and thus lead to further understanding of all presented photoprocesses.

As the examined photoinduced N₂O dissociation serves as a model system for electron-hole pair driven chemistry, the results of this study are an important step to understand photochemical processes on oxide surfaces in general.

Appendix A

Influence of atomic oxygen on CH₄

One main motivation in researching oxide chemistry in general and of atomic oxygen on MgO surfaces in particular is the oxidative coupling of methane. Oxidative coupling of methane is a chemical reaction mechanism in which methane is transformed into different compounds. A thorough overview has been written recently by Arndt et al [158], here, only important points will be summarized and discussed with focus on the investigations done in the course of this thesis.

The goal of oxidative methane coupling is to generate more valuable C_x compounds from CH₄:



This reaction pathway is, when initiated without any catalyst, less favorable than a CO_x generation. It could be demonstrated that Lithium-doped MgO serves as a good catalyst with an increased selectivity towards ethene generation [54].

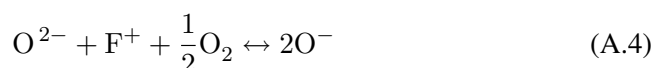
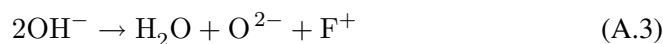
The mechanism behind the oxidative coupling of methane already mentioned briefly in chapter 1.1.2: The microscopic interpretation was based on the idea that Lithium atoms act as impurities in the MgO lattice by replacing magnesium atoms in it. In that manner, as Lithium has only one outer shell electron and a Li⁺O⁻ center, i.e. a localized hole, would be generated. On these centers, the assumed methane dissociation would take place [5]:



The methyl radicals would react in the gas phase to form ethane. By interacting with a second atomic oxygen site, ethane would form an C₂H₅^{*} radical which

would, in the presence of gaseous oxygen, lead to ethene formation.

This catalyst would soon be poisoned; all reactive sites would be transformed into OH⁻ species. As eq. A.1 suggests, oxygen has to be introduced into this system to obtain a stable catalytic cycle. Thus, the recovery of the catalyst was assumed to work as a Mars-van Krevelen mechanism:



For the present study it is noteworthy that also N₂O instead of O₂ is proposed as an oxidant due to its larger selectivity [5, 159] - despite the danger to produce HN. Nakamura et al showed that significantly more atomic, singly-charged oxygen was formed on MgO when N₂O was used as an oxidant instead of O₂. That is reasonable as N₂O has a lower binding energy than oxygen and thus dissociates more easily.

Summarizing, the presented mechanism made two suppositions:

- Lithium-doped magnesium oxide is the most versatile catalyst for the oxidative coupling of methane.
- The active center is in fact a localized hole located at an oxygen ion site of MgO.

While it is known that methane dissociates at high temperatures and high pressures, the conversion to the UHV region is questionable, as is a distinct correlation between prepared Li/MgO films under controlled UHV conditions and Li/MgO mixtures used in microreactors.

All of the above suppositions and questions were investigated by different working groups which collaborated in the Cluster of Excellence called "Unifying concepts in Catalysis". The approach chosen in this thesis was to investigate the possibilities for methane dissociation by pre-generated atomic oxygen.

As in the case of CO oxidation, the idea was to generate atomic oxygen by UV-induced N₂O dissociation on MgO films and then investigate the influence this oxygen has on a methane coadsorbate. The desorption energy of methane is about 12 kJ/mol [85] thus the lightly physisorbed molecule desorbs from the terrace already at 47 K (see Fig. A.1). The presence of atomic oxygen increases the desorption energy slightly and induces a lateral distortion in the adsorbate as the enhanced coverage dependence of the desorption energy proves.

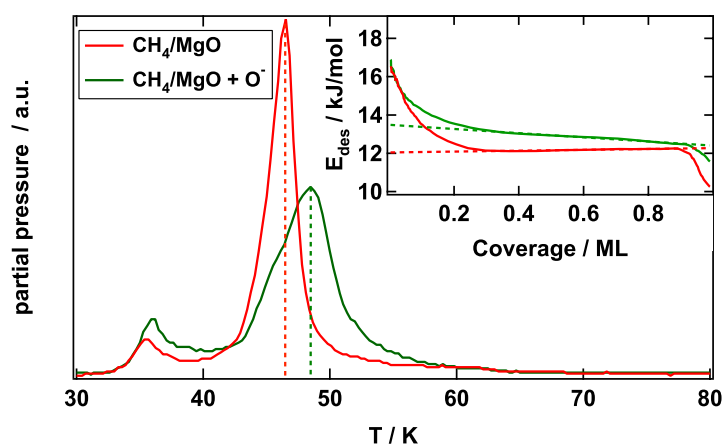


Figure A.1: Raw TPD spectra and inverse Polanyi-Wigner plots (inset) of CH_4 adsorbed on pristine MgO (red) and MgO with pregenerated atomic oxygen (green) show a shift of the desorption maximum of 2 K towards higher temperatures. The broadened peak structure and the increased coverage dependence of the desorption energy indicate increased lateral interactions due to the presence of atomic oxygen.

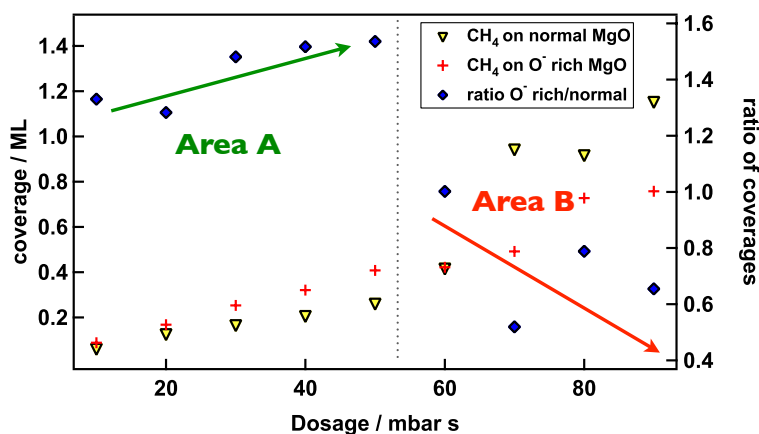


Figure A.2: Amount of adsorbed CH_4 in dependence of the respective dosage. The yellow triangles show the coverage of CH_4 on a regular MgO surface while the red crosses denote the amount of CH_4 coadsorbed with pregenerated atomic oxygen. The blue rhombuses finally show the ratio between both amounts, the corresponding y-axis is on the right side. Until a dosage of 50 mbar-s more CH_4 is adsorbed on MgO with pregenerated atomic oxygen than on pristine MgO, then the ratio changes so that more CH_4 is adsorbed on pristine MgO.

An examination of the relative sticking probabilities (by comparing the respective amount adsorbed by identical dosages on pristine MgO and MgO with coadsorbed atomic oxygen) show an interesting behavior (see Fig. A.2): until a dosage of 50 mbar·s the amount of CH₄ coadsorbed with pregenerated atomic oxygen exceeds the respective amount adsorbed on pristine MgO. At higher dosages this ratio is instantly inverted so that more CH₄ is adsorbed for the same dosage on pristine MgO than coadsorbed with atomic oxygen. Thus it can be concluded that the sticking coefficient of CH₄ adsorbed on MgO with pregenerated atomic oxygen abruptly decreases when more than 0.4 ML are adsorbed and that atomic oxygen increases the binding energy of CH₄ to the surface.

This dosage dependence can be interpreted as follows: Studies suggest that atomic oxygen enhances the adsorption energy of methane [160,161]. Since methane regularly binds to the MgO surface with two hydrogen atoms forming a bridge in such a way that the carbon atom rests over a magnesium ion [162] (see Fig A.3), a distortion of the adsorption characteristics is obvious: The bond to a regular oxygen site and a photogenerated atomic oxygen site will cause a non-balanced bond of CH₄ to the surface. This distortion will, at higher coverages, influence and hinder the adsorption of additional CH₄ molecules in its vicinity which results in a lower sticking coefficient.

Zobel et al have calculated a dissociation energy of CH₄ at singly charged atomic oxygen of about 72 kJ/mol [55]. In that sense, no thermally induced reaction should be expected. Unfortunately, when irradiating the coadsorbate consisting of CH₄ and pregenerated atomic oxygen again, no dissociation of methane was achieved either - in contrast to the induced CO oxidation described in chapter 6.2.

However, this negative result is in agreement to studies on different fields. More recent studies have revealed several aspects which clearly show that the suppositions mentioned earlier are wrong and too simplified:

- Though Li-doped MgO in fact has a high conversion rate and a high selectivity, however, it seems to lack a stability needed for industrialized purposes.
- Li⁺O⁻ centers are formed at temperatures above 700 °C, well above the desired temperatures for an OCM catalyst [3].
- Even if prepared, these centers are not only unstable but its role as an active center is put into question [163].
- Lithium is now thought to be a structural promoter, enhancing the generation of active sites of yet unknown nature [164].

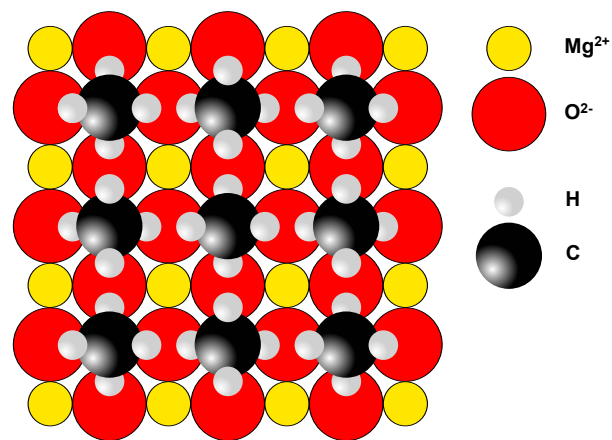


Figure A.3: Adsorption characteristics of methane on MgO. Methane binds with two hydrogen atoms to two oxygen ions so that the carbon atom rests above a magnesium ion. Neighboring CH₄ molecules are rotated by 90° with respect to each other. Based on Ref. [162]

- Finally, no CH₄ dissociation was detected by EPR studies of pregenerated atomic oxygen done in the former working group of Prof. Risse at the FHI Berlin.

Bibliography

- [1] Fujishima, A.; Zhang, X.; Tryk, D. *Surface Science Rep* **2008**, *63*, 515.
- [2] Diebold, U. *Surface Science Rep* **2003**, *48*, 53.
- [3] Zavyalova, U.; Weinberg, G.; Frandsen, W.; Girgsdies, F.; Risse, T.; Dinse, K.; Schlögl, R.; Horn, R. *ChemCatChem* **2011**, *3*, 1779.
- [4] Schlögl, R. *Angew Chem Int Edit* **1993**, *32*, 381.
- [5] Lunsford, J. *Angew Chem Int Edit* **1995**, *34*, 970.
- [6] Shido, T.; Asakura, K.; Iwasawa, Y. *Journal of catalysis* **1990**, *122*, 55–67.
- [7] Lisachenko, A.; Klimovskii, A.; Mikhailov, R.; Shelimov, B.; Che, M. *Catal Today* **2007**, *119*, 247.
- [8] Volodin, A. *Catal Today* **2000**, *58*, 103.
- [9] Lisachenko, A. *J Photoch Photobio A* **2008**, *196*, 127.
- [10] Ryabchuk, V. *International Journal of Photoenergy* **2004**, *6*, 95.
- [11] Volodin, A.; Bolshov, V.; Konovalova, T. *Molecular Engineering* **1994**, *4*, 221.
- [12] Ito, T.; Tashiro, T.; Watanabe, T.; Kawasaki, M.; Toi, K.; Kobayashi, H. *J Chem Soc Faraday T* **1990**, *86*, 4071.
- [13] Malykhin, S.; Volodin, A.; Bedilo, A.; Zhidomirov, G. *J Phys Chem C* **2009**, *113*, 10350.
- [14] Ito, T.; Kato, M.; Toi, K.; Shirakawa, T.; Ikemoto, I.; Tokuda, T. *J Chem Soc Farad T 1* **1985**, *81*, 2835.

- [15] Sterrer, M.; Berger, T.; Diwald, O.; Knözinger, E.; Allouche, A. *Top Catal* **2007**, *46*, 111.
- [16] Mueller, M.; Stankic, S.; Diwald, O.; Knözinger, E.; Sushko, P.; Trevisanutto, P.; Shluger, A. *J. Am. Chem. Soc.* **2007**, *129*, 12491.
- [17] Sterrer, M.; Berger, T.; Diwald, O.; Knözinger, E.; Sushko, P.; Shluger, A. *J Chem Phys* **2005**, *123*, 064714.
- [18] Berger, T.; Sterrer, M.; Diwald, O.; Knözinger, E. *J Phys Chem B* **2004**, *108*, 7280.
- [19] Sterrer, M.; Berger, T.; Stankic, S.; Diwald, O.; Knözinger, E. *ChemPhysChem* **2004**, *5*, 1695.
- [20] Sterrer, M.; Berger, T.; Diwald, O.; Knözinger, E. *J. Am. Chem. Soc.* **2003**, *125*, 195.
- [21] Sterrer, M.; Diwald, O.; Knözinger, E.; Sushko, P.; Shluger, A. *J. Phys. Chem. B* **2002**, *106*, 12478.
- [22] Diwald, O.; Sterrer, M.; Knözinger, E.; Sushko, P.; Shluger, A. *J Chem Phys* **2002**, *116*, 1707.
- [23] Diwald, O.; Sterrer, M.; Knözinger, E. *Phys Chem Chem Phys* **2002**, *4*, 2811.
- [24] Sterrer, M.; Diwald, O.; Knözinger, E. *J Phys Chem B* **2000**, *104*, 3601.
- [25] Knözinger, E.; Diwald, O.; Sterrer, M. *J Mol Catal A-Chem* **2000**, *162*, 83.
- [26] Kolasinski, K. *Surface science: Foundations of catalysis nanoscience*; 2009; p 1.
- [27] M. Henzler, W. G. *Oberflächenphysik des Festkörpers*; 1994; p 1.
- [28] Christmann, K. *Introduction to surface physical chemistry*; 1997; p 1.
- [29] Ibach, H. *Physics of surfaces and interfaces*; 2006; p 1.
- [30] Redlich, B. *Adsorption von CO₂, N₂O und D₂O an MgO(100)-Einkristallspaltflächen. Polarisations-Infrarotspektroskopie, Beugung langsamer Elektronen, Spektren- und Strukturberechnungen.*; 1998; p 1.

- [31] Schleife, A.; Roedl, C.; Fuchs, F.; Furthmueller, J.; Bechstedt, F. *Phys Rev B* **2009**, *80*, 035112.
- [32] Beck, K.; Joly, A.; Hess, W. *Appl Surface Science* **2009**, *255*, 9562.
- [33] Garrone, E.; Zecchina, A.; Stone, F. *Philos Mag B* **1980**, *42*, 683.
- [34] Kantorovich, L.; Holender, J.; Gillan, M. *arXiv* **2008**, 1.
- [35] Emeline, A.; Kuzmin, G.; Purevdorj, D.; Ryabchuk, V.; Serpone, N. *J Phys Chem B* **2000**, *104*, 2989.
- [36] Spoto, G.; Gribov, E.; Ricchiardi, G.; Damin, A.; Scarano, D.; Bordiga, S.; Lamberti, C.; Zecchina, A. *Prog Surface Science* **2004**, *76*, 71.
- [37] Schintke, S.; Messerli, S.; Pivetta, M.; Patthey, F.; Libioulle, L.; Stengel, M.; de Vita, A.; Schneider, W. *Phys. Rev. Lett.* **2001**, *87*, 276801.
- [38] Pacchioni, G. *ChemPhysChem* **2003**, *4*, 1041.
- [39] Sterrer, M.; Fischbach, E.; Risse, T.; Freund, H. *Phys. Rev. Lett.* **2005**, *94*, 186101.
- [40] Pacchioni, G.; Pescarmona, P. *Surface Science* **1998**, *412-13*, 657.
- [41] Xu, Y.; Zhang, Y.; Li, J. *Chem Phys* **2005**, *315*, 267.
- [42] Ricci, D.; Pacchioni, G.; Sushko, P.; Shluger, A. *J Chem Phys* **2002**, *117*, 2844.
- [43] Ricci, D.; di Valentin, C.; Pacchioni, G.; Sushko, P.; Shluger, A.; Giannelis, E. *J Am Chem Soc* **2003**, *125*, 738.
- [44] Benia, H.; Myrach, P.; Gonchar, A.; Risse, T.; Nilus, N.; Freund, H. *Phys Rev B* **2010**, *81*, 241415.
- [45] Zhukovskii, Y.; Kotomin, E.; Borstel, G. *Vacuum* **2004**, *74*, 235.
- [46] Inntam, C.; Moskaleva, L.; Neyman, K.; Nasluzov, V.; Rosch, N. *Appl Phys A-Mater* **2006**, *82*, 181.
- [47] Freund, H. *Chem-Eur J* **2010**, *16*, 9384.
- [48] Giordano, L.; del Vitto, A.; Pacchioni, G.; Ferrari, A. *Surface Science* **2003**, *540*, 63.

- [49] Smith, D.; Tench, A. *Chem Commun* **1968**, 1113.
- [50] Tench, A.; Lawson, T.; Kibblewhite, J. *J Chem Soc Farad T 1* **1972**, *68*, 1169.
- [51] Nakamura, M.; Yanagibashi, H.; Mitsunashi, H.; Takezawa, N. *B Chem Soc Jpn* **1993**, *66*, 2467.
- [52] Costa, D.; Chizallet, C.; Ealet, B.; Goniakowski, J.; Finocchi, F. *J Chem Phys* **2006**, *125*, 054702.
- [53] Ealet, B.; Goniakowski, J.; Finocchi, F. *Phys Rev B* **2004**, *69*, 195413.
- [54] Ito, T.; Wang, J.; Lin, C.; Lunsford, J. *J. Am. Chem. Soc.* **1985**, *107*, 5062.
- [55] Zobel, N.; Behrendt, F. *J Chem Phys* **2006**, *125*, 074715.
- [56] Mather, P.; Read, J.; Buhrman, R. *arXiv* **2006**, 1.
- [57] Wollschläger, J.; Erdös, D.; Goldbach, H.; Hopken, R.; Schröder, K. *Thin Solid Films* **2001**, *400*, 1.
- [58] Wollschläger, J.; Viernow, J.; Tegenkamp, C.; Erdös, D.; Schröder, K.; Pfnür, H. *Appl Surface Science* **1999**, *142*, 129.
- [59] Tegenkamp, C.; Pfnür, H.; Ernst, W.; Malaske, U.; Wollschläger, J.; Peterka, D.; Schröder, K.; Zielasek, V.; Henzler, M. *J Phys-Condens Mat* **1999**, *11*, 9943.
- [60] Kiguchi, M.; Goto, T.; Saiki, K.; Sasaki, T.; Iwasawa, Y.; Koma, A. *Surface Science* **2002**, *512*, 97.
- [61] Freund, H.; Pacchioni, G. *Chem Soc Rev* **2008**, *37*, 2224.
- [62] Vaida, M.; Bernhardt, T.; Barth, C.; Esch, F.; Heiz, U.; Landman, U. *Phys Status Solidi B* **2010**, *247*, 1001.
- [63] Altieri, S.; Tjeng, L.; Sawatzky, G. *Thin Solid Films* **2001**, *400*, 9.
- [64] Ouvrard, A.; Niebauer, J.; Ghalgaoui, A.; Barth, C.; Henry, C.; Bourguignon, B. *J Phys Chem C* **2011**, *115*, 8034.
- [65] Schintke, S.; Schneider, W. *J Phys-Condens Mat* **2004**, *16*, 49.

- [66] Sterrer, M.; Risse, T.; Heyde, M.; Rust, H.; Freund, H. *Phys. Rev. Lett.* **2007**, *98*, 206103.
- [67] Sterrer, M.; Risse, T.; Pozzoni, U.; Giordano, L.; Heyde, M.; Rust, H.; Pacchioni, G.; Freund, H. *Phys. Rev. Lett.* **2007**, *98*, 096107.
- [68] Nilius, N.; Risse, T.; Schauer mann, S.; Shaikhutdinov, S.; Sterrer, M.; Freund, H. *Top Catal* **2011**, *54*, 4.
- [69] Giordano, L.; Pacchioni, G. *Phys Chem Chem Phys* **2006**, *8*, 3335.
- [70] Shluger, A.; McKenna, K.; Sushko, P.; Ramo, D.; Kimmel, A. *Modelling Simul. Mater. Sci. Eng.* **2009**, *17*, 084004.
- [71] Gonchar, A.; Risse, T.; Freund, H.; Giordano, L.; Valentin, C. D.; Pacchioni, G. *Angew Chem Int Edit* **2011**, *50*, 2635.
- [72] Carrasco, E.; Brown, M.; Sterrer, M.; Freund, H.; Kwapien, K.; Sierka, M.; Sauer, J. *J Phys Chem C* **2010**, *114*, 18207.
- [73] Frischkorn, C.; Wolf, M. *Chem Rev* **2006**, *106*, 4207.
- [74] di Valentin, C.; Ricci, D.; Pacchioni, G.; Chiesa, M.; Paganini, M.; Giannello, E. *Surface Science* **2002**, *521*, 104.
- [75] Freund, H. *Faraday Discuss* **1999**, *114*, 1.
- [76] Redhead, P. *Vacuum* **1962**, *12*, 203.
- [77] de Jong, A.; Niemandtsverdriet, J. *Surface Science* **1990**, *233*, 355.
- [78] King, D. *Surface Science* **1975**, *47*, 384.
- [79] Koch, M. *Schwingungsspektroskopische Untersuchung von molekularen Schaltprozessen auf Au(111)*; 2009; p 1.
- [80] Jr., J. Y. *Experimental innovations in surface science*; 1997; p 1.
- [81] Bdzoch, J. *Ultrafast Energy and Charge Transfer in D₂O/Ru(0001)*; 2010; p 1.
- [82] Schlichting, H.; Menzel, D. *Rev Sci Instrum* **1993**, *64*, 2013.
- [83] Lian, J. C.; Kieseritzky, E.; Gonchar, A.; Sterrer, M.; Rocker, J.; Gao, H.; Risse, T. *J Phys Chem C* **2010**, *114*, 3148.

- [84] Dohnalek, Z.; Kimmel, G.; McCready, D.; Young, J.; Dohnalkova, A.; Smith, R.; Kay, B. *J Phys Chem B* **2002**, *106*, 3526.
- [85] Dohnalek, Z.; Smith, R.; Kay, B. *J Phys Chem B* **2002**, *106*, 8360.
- [86] Feulner, P.; Menzel, D. *Journal of Vacuum Science and Technology* **1980**, *17*, 662–663.
- [87] Schlichting, H.; Menzel, D. *Surface Science* **1993**, *285*, 209.
- [88] Garcia, V.; Bricenoalero, J.; Mora, A. *Surface Science* **1995**, *341*, 196.
- [89] Holland, L.; Steckelmacher, W.; Yarwood, J. *Vacuum manual*; 2003; p 1.
- [90] Wutz, M. *Theorie und Praxis der Vakuumtechnik*; 1965; p 1.
- [91] Tredelenburg, E. *Ultrahochvakuum, eine Einführung*; 1963; p 1.
- [92] Denzler, D. *Zur ultraschnellen Reaktionsdynamik von Wasserstoff und Grenzflächenstruktur von Wasser auf der Ru(001)-Oberfläche*; 2003; p 1.
- [93] de Jong, A.; Niemantsverdriet, J. *Vacuum* **1990**, *41*, 232.
- [94] Garcia, V.; Bricenoalero, J.; Martinez, L. *Surface Science* **1995**, *339*, 189.
- [95] Kowalczyk, P.; Kaneko, K.; Terzyk, A.; Tanaka, H.; Kanoh, H.; Gauden, P. *J Colloid Interf Sci* **2005**, *291*, 334.
- [96] Tomkova, E. *Surface Science* **1996**, *351*, 309.
- [97] Garcia, V.; Briceno-Valero, J.; Martinez, L. *Vacuum* **1997**, *48*, 941.
- [98] Tomkova, E.; Stara, I. *Vacuum* **1998**, *50*, 227.
- [99] Lombardo, S.; Bell, A. *Surface Science* **1989**, *224*, 451.
- [100] Reuter, K. *Modeling Heterogeneous Catalytic Reactions: From the Molecular Process to the Technical System* **2009**, *1*.
- [101] Rieger, M.; Rogal, J.; Reuter, K. *Phys Rev Lett* **2008**, *100*, 016105.
- [102] Lombardo, S.; Bell, A. *Surface Science* **1988**, *206*, 101.
- [103] Dohnalek, Z.; Kimmel, G.; Joyce, S.; Ayotte, P.; Smith, R.; Kay, B. *J Phys Chem B* **2001**, *105*, 3747.

- [104] Wu, M.; Estrada, C.; Corneille, J.; Goodman, D. *J Chem Phys* **1992**, *96*, 3892.
- [105] Gonchar, A. *Defect chemistry of single crystalline MgO(001) films*; 2011; p 1.
- [106] Che, M.; Bond, G. *Book* **1985**, 442.
- [107] Kramer, J.; Ernst, W.; Tegenkamp, C.; Pfnür, H. *Surface Science* **2002**, *517*, 87.
- [108] Benedetti, S.; Benia, H.; Nilius, N.; Valeri, S.; Freund, H. *Chem Phys Lett* **2006**, *430*, 330.
- [109] Chen, M.; Goodman, D. *Journal of Physics: Condensed Matter* **2008**, *20*, 264013.
- [110] Fuchs, R.; Kliewer, K. *Phys. Rev* **1965**, 2076.
- [111] Gazis, D.; Wallis, R. *J. Math. Phys.* **1962**, *3*, 190.
- [112] Wu, Y.; Garfunkel, E.; Madey, T. *Surface Science* **1996**, *365*, 337.
- [113] Savio, L.; Celasco, E.; Vattuone, L.; Rocca, M.; Senet, P. *Phys Rev B* **2003**, *67*, 075420.
- [114] Savio, L.; Celasco, E.; Vattuone, L.; Rocca, M. *J Chem Phys* **2003**, *119*, 12053.
- [115] Wang, Y.; Weinberg, W. *Physical Review Letters* **1992**, *69*, 3326.
- [116] Wang, Y.; Weinberg, W. *Surface Science* **1992**, *287/288*, 1102.
- [117] Charles, C.; Leclerc, G.; Pireaux, J.; Rasson, J. *Surf. Interface Anal.* **2004**, *36*, 49.
- [118] Cox, P.; Flavell, W.; Williams, A.; Egdell, R. *Surface Science* **1985**, *152*, 784.
- [119] Cox, P.; Williams, A. *Journal of electron spectroscopy and related Phenomena* **1986**, *39*, 45.
- [120] Hosoi, J.; Oikawa, T.; Kobuko, Y. *J Electron Microsc* **1985**, *34*, 73.
- [121] Wang, F.; Egerton, R.; Malac, M. *Ultramicroscopy* **2009**, *109*, 1245.

- [122] Wang, Y.; Meyer, B.; Kotsis, K.; Stodt, D.; Staemmler, V.; Qiu, H.; Traeger, F.; Langenberg, D.; Muhler, M.; Woell, C. *Angew Chem Int Edit* **2007**, *46*, 5624.
- [123] Wang, Y. *J Phys Chem* **2008**, *222*, 927.
- [124] Marsh, E.; Petitto, S.; Harbison, G.; Wulser, K.; Langell, M. *Journal of Vacuum Science & Technology A: Vacuum, Surfaces, and Films* **2005**, *23*, 1061.
- [125] Heidberg, J.; Redlich, B. *Surface Science* **1996**, *368*, 140.
- [126] Daub, C.; Patey, G.; Jack, D.; Sallabi, A. *J Chem Phys* **2006**, *124*, 114706.
- [127] Xu, Y.; Li, J.; Zhang, Y. *J Theor Comput Chem* **2003**, *2*, 57.
- [128] Tidwell, E.; Plyler, E.; Benedikt, W. *J Opt Soc Am* **1960**, *50*, 1243.
- [129] Kantorovich, L.; Gillan, M. *Surface Science* **1997**, *374*, 373.
- [130] Nakamura, M.; Mitsunashi, H.; Takezawa, N. *Journal of Catalysis* **1992**, *138*, 686.
- [131] Kiss, J.; Lennon, D.; Jo, S.; White, J. *J Phys Chem-Us* **1991**, *95*, 8054.
- [132] Kim, K.; Watanabe, K.; Menzel, D.; Freund, H. *J Phys-Condens Mat* **2010**, *22*, 084012.
- [133] Sawabe, K.; Matsumoto, Y. *Surface Science* **1993**, *283*, 126.
- [134] Wlodarczyk, R.; Sierka, M.; Kwapien, K.; Sauer, J.; Carrasco, E.; Aumer, A.; Gomes, J.; Sterrer, M.; Freund, H. *J Phys Chem C* **2011**, *115*, 6764.
- [135] Ahmed, S.; Perry, S.; El-Bjeirami, O. *J Phys Chem B* **2000**, *104*, 3343.
- [136] Kim, Y.; Stultz, J.; Goodman, D. *J Phys Chem B* **2002**, *106*, 1515.
- [137] Kapteijn, F.; Rodriguez-Mirasol, J.; Moulijn, J. *Appl Catal B-Environ* **1996**, *9*, 25.
- [138] Pietrzyk, P.; Zasada, F.; Piskorz, W.; Kotarba, A.; Sojka, Z. *Catal Today* **2007**, *119*, 219.

- [139] Guesmi, H.; Berthomieu, D.; Kiwi-Minsker, L. *J Phys Chem C* **2008**, *112*, 20319.
- [140] Swamy, C.; Christopher, J. *Catalysis Reviews* **1992**, *34*, 409.
- [141] Berger, T.; Diwald, O.; Knözinger, E.; Sterrer, M.; Yates, J. *Phys Chem Chem Phys* **2006**, *8*, 1822.
- [142] Chizallet, C.; Costentin, G.; Lauron-Pernott, H.; Krafft, J.; Che, M.; Delbecq, F.; Sautet, P. *J Phys Chem C* **2008**, *112*, 16629.
- [143] Gonchar, A.; Risse, T.; Giamello, E.; Freund, H. *Phys Chem Chem Phys* **2010**, *12*, 12520.
- [144] Peterka, D.; Tegenkamp, C.; Schröder, K.; Ernst, W.; Pfnür, H. *Surface Science* **1999**, *431*, 146.
- [145] Chambers, S. *Surface Science Rep* **2000**, *39*, 105.
- [146] Kurth, M.; Graat, P.; Mittemeijer, E. *Thin solid films* **2006**, *500*, 61.
- [147] Kurth, M.; Graat, P.; Carstanjen, H.; Mittemeijer, E. *Surface and interface analysis* **2006**, *38*, 931.
- [148] Chiesa, M.; Giamello, E.; Che, M. *Chem Rev* **2010**, *110*, 1320.
- [149] Pinarello, G.; Pisani, C.; D'Ercole, A.; Chiesa, M.; Paganini, M.; Giamello, E.; Diwald, O. *Surface Science* **2001**, *494*, 95.
- [150] di Valentin, C.; Ferullo, R.; Binda, R.; Pacchioni, G. *Surface Science* **2006**, *600*, 1147.
- [151] Chiesa, M.; Paganini, M.; Spoto, G.; Giamello, E.; di Valentin, C.; del Vitto, A.; Pacchioni, G. *J Phys Chem B* **2005**, *109*, 7314.
- [152] Berger, T.; Sterrer, M.; Stankic, S.; Bernardi, J.; Diwald, O.; Knözinger, E. *Mat Sci Eng C-Bio S* **2005**, *25*, 664.
- [153] Freund, H.; Meijer, G.; Scheffler, M.; Schlögl, R.; Wolf, M. *Angew Chem Int Edit* **2011**, *50*, 10064.
- [154] Pacchioni, G.; Minerva, T. *Surface Science* **1992**, *275*, 450.
- [155] Nygren, M.; Pettersson, L. *J Chem Phys* **1996**, *105*, 9339.

- [156] Sterrer, M.; Risse, T.; Freund, H. *Appl Catal A-Gen* **2006**, *307*, 58.
- [157] Lei, Y.; Lewandowski, M.; Sun, Y.; Fujimori, Y.; Martynova, Y.; Groot, I.; Meyer, R.; Giordano, L.; Pacchioni, G.; Goniakowski, J.; Noguera, C.; Shaikhutdinov, S.; Freund, H. *Chemcatchem* **2011**, *3*, 671.
- [158] Arndt, S.; Laugel, G.; Levchenko, S.; Horn, R.; Baerns, M.; Scheffler, M.; Schlögl, R.; Schomäcker, R. *Catalysis Reviews* **2011**, *53*, 424.
- [159] Yamamoto, H.; Chu, H.; Xu, M.; Shi, C.; Lunsford, J. *Journal of Catalysis* **1993**, *142*, 325.
- [160] Dash, L.; Gillan, M. *Surface Science* **2004**, *549*, 217.
- [161] Orlando, R.; Cora, F.; Millini, R.; Perego, G.; Dovesi, R. *J Chem Phys* **1996**, *105*, 8937.
- [162] Drummond, M.; Sumpter, B.; Shelton, W.; Larese, J. *Phys. Rev. B* **2006**, *73*, 195313.
- [163] S. Arndt and U. Simon and S. Heitz and A. Berthold and B. Beck and O. Görke and J.D. Epping and T. Otremba and Y. Aksu and E. Irran and G. Laugel and M. Driess and H. Schubert and R. Schomäcker, *Top Catal* **2011**, *1*.
- [164] Zavyalova, U.; Geske, G.; Horn, R.; Weinberg, G.; Frandsen, W.; Schuster, M.; Schlögl, R. *Chemcatchem* **2010**, *3*, 949.

Abbreviations

AES Auger Electron Spectroscopy

DFT Density Functional Theory

EPR Electron Paramagnetic Resonance

FKP Fuchs-Kliwer Phonon

FTIR Fourier Transform Infrared Spectroscopy

FWHM Full width half maximum

HrEELS High resolution Electron Energy Loss Spectroscopy

IR Infrared

IRAS Infrared Reflection Absorption Spectroscopy

ML Monolayer

QMS Quadrupole Mass Spectrometer

SEM Scanning Electron Microscopy

(SPA-)LEED Spot Profile Analysis Low Energy Electron Diffraction

STM Scanning Tunneling Microscopy

TDS Thermal Desorption Spectroscopy

TPD Temperature Programmed Desorption

tr Electron Trap

TST Transition State Theory

UHV Ultra High Vacuum

UV Ultraviolet

Publications

Related to this Thesis

1. P. Giese, H. Kirsch, M. Wolf and C. Frischkorn. *Reduction of N₂O on MgO/Ag(001) via UV-Photoinduced Trapped Electrons*, J. Phys. Chem. C 115, 10012-10016 (2011)
2. P. Giese, H. Kirsch, C. Frischkorn and M. Wolf. *Photon energy dependent generation of atomic oxygen by photoinduced N₂O dissociation on thin MgO films*, in preparation
3. P. Giese, C. Frischkorn and M. Wolf. *Chemistry with atomic oxygen under optimized preparation conditions on MgO/Ag(001)*, in preparation

Not related to the thesis

1. N. Owschimikow, F. Königsmann, J. Maurer, P. Giese, A. Ott, B. Schmidt and N. Schwentner. *Cross sections for rotational decoherence of perturbed nitrogen measured via decay of laser-induced alignment*, J. Chem. Phys. 133, 04431 (2010)

Curriculum vitae

For reasons of data protection, the curriculum vitae is not included in the online version

Danksagung

Herzlich danke ich Martin Wolf nicht nur für die Möglichkeit, eine Doktorarbeit in seiner Arbeitsgruppe durchführen zu können. Die Diskussionen um die Meßdaten mit ihm waren nicht nur essentiell, hilfreich, lebhaft und auch amüsant. Gerade die Zeiten zwischen den Jahren, wenn wenig Leute so verrückt waren und arbeiteten habe ich den Austausch mit ihm in sehr angenehmer Erinnerung.

Mit Jose Ignacio Pascual habe ich einen freundlichen Zweitgutachter gefunden, zu dem ich auch deshalb gute Kontakte hatte, weil der Raum meines Labores nominell "ihm" gehörte. Ich danke ihm dafür, mir bei Materialfragen weitergeholfen zu haben oder wenn ich für meinen Aufbau ganz schnell etwas ausleihen mußte.

Christian Frischkorn war für den größten Teil der Arbeit mein Betreuer. Martin Wolf und Christian Frischkorn ergänzten sich als meine beiden Vorgesetzten sehr gut. Wenn ich das Temperament von Martin Wolf falsch eingeschätzt hab, hat mir Christians ruhige und verständnisvolle Art weiter geholfen. Auch ihm danke ich auch ihm herzlich für alle Unterstützung und sein Vertrauen, daß er mir entgegenbrachte.

Kramer Campen was for the last year the leader of the working group I was involved in. I thank him for the fruitful discussions about my project. The questions which arose helped me a lot. Beside these technical discussions I thank him for being a very nice man who puts a lot of trust in someone and is eager to help.

Harald Kirsch war nicht nur für ein Jahr mein Diplomand (und dementsprechend essentieller Teil des experimentellen Aufbaus!) und guter Freund, sondern eine große Hilfe, das Experiment zum Laufen zu bekommen. Ich erinnere mich gerne an die gemeinsame Zeit im Labor, nicht nur an die Frustrationen, die ein EFM Evaporator so mit sich bringt, sondern an die großen Momente des Erfolges, die schönen Gespräche, an volle Pulle Manowar aus den Boxen und die dreckigen Witze.

Willi Krauss hat viel Zeit und Energie in den Aufbau, der zu Beginn nicht

umsonst auch "Kammer des Todes" genannt wurde, investiert. Mit seiner Hilfe schaffte ich es nicht nur, die Kammer lauffähig zu machen, sondern vor allem, die Kälteanbindung des Kristalls an den Kryostaten zu optimieren. Ich denke, daß Willi mit seiner derben Art eine wunderbare Ergänzung zu Harald und mir war. Nebenbei habe ich von ihm die beste Definition von Verlobungszeit gehört: "Verlobung ist, als hätte man ein Fahrrad bekommen, auf dem man noch nicht fahren darf. Aber man darf schonmal ein wenig klingeln".

Mit Juraj Bdzoch habe ich die ersten Monate in der AG Wolf an seinem Projekt gearbeitet, um die experimentellen Techniken der Oberflächenphysik dort zu lernen. Dort habe ich nicht nur die Wunderwelt der SFG-Spektroskopie, sondern vor allem einen guten Freund kennen gelernt. Auch nach der gemeinsamen Zeit im Labor hielt der freundschaftliche Kontakt immer an. Juraj ist eine gute Seele, die, wenn man Fragen hat, so viel hilft, daß der Anstand einen dazu zwingt, ihn darauf hinzuweisen, daß er noch andere Dinge zu tun hat, als einem zu helfen :)

Uwe Lipowski, Rainhard Franke und allen Technikern an der FU und dem Fritz Haber Institut danke ich für die Hilfe, meine Konstruktionsideen zu realisieren und allen anderen technischen Support. Herrn Streuber und dem Tieftemperaturlabor danke ich herzlich für alles Helium und alle Hilfe, die sie mir in den letzten Jahren geleistet haben.

Natürlich danke ich auch der restlichen AG Wolf bzw. der Abteilung für physikalische Chemie, speziell den Exilanten, die in der Fabbeckstraße arbeiten. Es war immer eine schöne Zeit mit Euch, man konnte immer mit Eurer Hilfe rechnen und wunderbar beim Kaffee schwatzen.

Ehemalig auch zur AG Wolf dazugehörig danke ich Petra Tegeder und ihrer Arbeitsgruppe für die gemeinsame Zeit, als ich das alte HrEELS-Spektrometer für meine Zwecke abzurichten versuchte. Petra ist eine Frau mit viel Humor, mit der man wunderbar und fundiert über die Messungen diskutieren kann. Innerhalb der Arbeitsgruppe danke ich ganz speziell Felix Leyssner und Stephan Meyer, den beiden Experten in Sachen EELS, die mir geholfen haben, diese Maschine überhaupt (wieder) zum Laufen zu bekommen. Die kurze Zeit bei Euch war wirklich sehr schön!

The EPR measurements were done with Anastasia Gonchar in the working group of Thomas Risse at the chemical physics department of the Fritz-Haber Institute. I especially thank Anastasia for the short time together, where she introduced me to the world of EPR spectroscopy.

I can proudly say to be a member of the "international Max Planck research

school - complex systems and material science". The discussion meetings and block courses were possibilities to look at surface science in a larger context and get in touch with other PhD-Students. Especially the small conference "From Complex to comprehensive - visions in surface science" was a great opportunity to learn how a conference is organized and to get in touch with people whose papers and reports I read since the beginning of my project.

Part of this work was funded by the Cluster of Excellence "Unifying concepts in catalysis" which is gratefully acknowledged.

Meiner Familie danke ich herzlich für alle Unterstützung auf meinem Weg und dafür, mich aufgemuntert zu haben, wenn es mal nicht weiterging. Meinem Vater kann ich nicht genügend danken für alle Unterstützung, allen Rat und alle Tat, für die Gespräche über Physik und Chemie, für alle Hilfe, alle Motivation, alle Beruhigung, wenn der Aufbau mir mitten in der Nacht einen Tobsuchtsanfall bescherte....

Zum Schluß danke ich meiner lieben Hedda, einfach sie selbst zu sein und das große Wunder, mich trotz all meiner Flausen zu lieben. Ich danke ihr als Laiin, sich alle Probevorträge angehört zu haben.

+ OAMDG +

Erklärung gemäß §7, Abs. 4 der Promotionsordnung

Hiermit versichere ich, daß diese Arbeit von niemandem anderen als mir angefertigt wurde. Alle verwendeten Hilfsmittel wurden angegeben. Zitate und Abbildungen aus fremden Arbeiten sind als solche kenntlich gemacht. Diese Arbeit wurde bisher in gleicher oder ähnlicher Form keiner anderen Prüfungskommission vorgelegt und auch nicht veröffentlicht.

Berlin, den

(Datum, Unterschrift)